BRNO UNIVERSITY OF TECHNOLOGY
VYSOKÉ UČENÍ TECHNICKÉ V BRNĚ

FACULTY OF MECHANICAL ENGINEERING
FAKULTA STROJNÍHO INŽENÝRSTVÍ

INSTITUTE OF PHYSICAL ENGINEERING
ÚSTAV FYZIKÁLNÍHO INŽENÝRSTVÍ

DESIGN OF OPTICALLY DETECTED MAGNETIC RESONANCE (ODMR) SPECTROMETER
NÁVRH SPEKTROMETRU S OPTICKY DETEKOVANOU MAGNETICKOU REZONANCÍ

MASTER'S THESIS
DIPLOMOVÁ PRÁCE

AUTHOR — **Bc. Martin Schneider**
AUTOR PRÁCE

SUPERVISOR — **Ing. Petr Neugebauer, Ph.D.**
VEDOUCÍ PRÁCE

BRNO 2017

VYSOKÉ UČENÍ TECHNICKÉ V BRNĚ
FAKULTA STROJNÍHO INŽENÝRSTVÍ

Zadání diplomové práce

Ústav:	Ústav fyzikálního inženýrství
Student:	**Bc. Martin Schneider**
Studijní program:	Aplikované vědy v inženýrství
Studijní obor:	Fyzikální inženýrství a nanotechnologie
Vedoucí práce:	**Ing. Petr Neugebauer, Ph.D.**
Akademický rok:	2016/17

Ředitel ústavu Vám v souladu se zákonem č.111/1998 o vysokých školách a se Studijním a zkušebním řádem VUT v Brně určuje následující téma diplomové práce:

Návrh spektrometru s opticky detekovanou magnetickou rezonancí

Stručná charakteristika problematiky úkolu:

Rychlá a zároveň citlivá charakterizace paramagnetických molekul, které můžou být využity v paměťových jednotkách o vysoké hustotě nebo jako kvantové bity v kvantových počítačích, v poslední době nabývá na významu. Hlavní cíl této diplomové práce je navrhnout a sestavit systém opticky detekované magnetické rezonance (ODMR) modifikací stávajícího spektrometru magnetického kruhového dichroismu (MCD) umožňující citlivou charakterizaci paramagnetických molekul, také nazývaných jednomolekulární magnety. Nový ODMR spektrometr bude využívat stávající osvětlení v rozsahu od ultrafialového po viditelné světlo (UV–VIS), ke kterému bude přivedeno ozařování vzorku pomocí mikrovlnného zdroje nezbytné pro paramagnetickou excitaci. Bude navrhnut a sestrojen nový držák vzorku, který umožní přístup mikrovlnného záření i spektra UV–VIS ke vzorku. Implementace mikrovlnného ozáření bude založena na teorii šíření Gaussovského svazku s aproximací ve volném prostoru a bude připojena do současné optické osy spektrometru. Možnosti a schopnosti nově zavedeného systému budou demonstrovány na sloučeninách s přechodnými kovy a na molekulárních komplexech lanthanoidů.

Cíle diplomové práce:

1. Vytvoření nové experimentální sestavy pro optickou detekci magnetické resonance (ODMR) modifikací stávajícího spektrometru magnetického kruhového dichroismu (MCD).
2. Navržení nového držáku vzorku vhodného pro oba typy ozařování.
3. Prokázání schopností nově zavedeného systému na sloučeninách s přechodnými kovy a na molekulárních komplexech lanthanoidů.

Seznam doporučené literatury:

GOLDSMITH, P. F. Quasioptical systems: Gaussian beam quasioptical propagation and applications. Piscataway, NJ: IEEE Press, 1998. ISBN 07-803-3439-6.

REYHER, H.-J. et al. Optically detected magnetic resonance via the magnetic circular dichroism of absorption of cerium impurities in bulk paramagnetic terbium gallium garnet. Journal of Physics: Condensed Matter. 1999, 9(42), 9065-9082. ISSN 09538984.

BAUER, T. et al. Indium-tin-oxide-coated glass as dichroic mirror for far-infrared electromagnetic radiation. Journal of Applied Physics. American Institute of Physics, 2002, 92(4), 2210-2212.

Termín odevzdání diplomové práce je stanoven časovým plánem akademického roku 2016/17

V Brně, dne

L. S.

prof. RNDr. Tomáš Šikola, CSc. ředitel ústavu	doc. Ing. Jaroslav Katolický, Ph.D. děkan fakulty

Abstract
The subject of this master's thesis is to develop a new spectrometer of Optically Detected Magnetic Resonance (ODMR) by modification of standard Magnetic Circular Dichroism (MCD) spectrometer. A new microwave irradiation is added and coupled to the optical path by ITO coated dichroic mirror. The microwave beam is guided through series of quasi-optical lenses. For irradiation with lower frequencies, antenna determined to be placed beneath the sample is designed. The performance of the new ODMR spectrometer is then demonstrated on various metal complexes.

Abstrakt
Diplomová práce se zabývá návrhem a sestavením nového spektrometru opticky detekované magnetické rezonance (ODMR) modifikací stávajícího spektrometru magnetického kruhového dichroismu (MCD) přivedením mikrovlnného ozařování. Je navrhnut nový držák vzorku umožnující osvětlení jak viditelným světlem, tak mikrovlnným zářením. Pro přivedení vlnění o nižších frekvencích je navržena anténa, určená k umístění pod vzorkem. Schopnosti celého systému jsou demonstrovány na sloučenínách kovových komplexů.

Keywords
Quasi-optics, Gaussian beam, spectroscopy, ODMR, EPR, MCD, single molecule magnet

Klíčová slova
Kvasioptika, Gaussovský svazek, spektroskopie, ODMR, EPR, MCD, jednomolekulární magnet

SCHNEIDER, Martin. *Design of Optically Detected Magnetic Resonance (ODMR) Spectrometer*. Brno, 2017. 66 p. Diplomová práce. Brno University of Technology. Faculty of Mechanical Engineering. Supervised by Petr NEUGEBAUER.

Declaration

I hereby declare that I have written my master's thesis entitled *Design of Optically Detected Magnetic Resonance (ODMR) Spectrometer* independently and it is a record of an original work done by me under the guidance of the supervisor, Ing. Petr Neugebauer, Ph.D., and using the technical literature and other sources of information which are all properly quoted in the thesis and detailed in the list of literature at the end of this thesis.

.....	.....
Place and date	Bc. Martin Schneider

Acknowledgment
I would like to thank my supervisor Ing. Petr Neugebauer, Ph.D.for his expertise, guidance and patience at all times. The good advice and support has been invaluable. I am very grateful to the whole group of Joris van Slageren at the University of Stuttgart for inspiring comments and given opportunities. My special thanks belong to Samuel Lenz, Michal Kern and Boris Tschertsche. I would like to extend my sincere gratitude to my friends and colleagues at the Institute of Physical Engineering together with co-workers at laboratories of CEITEC Nano Research Infrastructure. Above all, I am immensely thankful to my girlfriend Klára for the support, love and understanding. Last but not least, I am grateful for the encouragement my parents and my sister have given me. It would not have been possible to write this thesis without the help and support of the kind people around me.

Bc. Martin Schneider

Contents

1. Introduction and Motivation

"There's Plenty of Room at the Bottom"

Richard Feynman
Pasadena, 29 December 1959

Current computer technology stands on manipulation with electron and its charge. A fundamental element of computer architecture nowadays is a transistor. In order to improve the parameters of computing units it is necessary to reduce the dimensions of these elements. However, transistors miniaturizing is not limitless. It arrives to its limits from approximately 10 nm when the effects of quantum physics emerge. For example, imagine two conducting channels several nanometres wide and in comparable distance from each other. If we put one electron into one of the channel, according to quantum physics there is a probability the electron could be present in both channels at the same time or alternate its occurrence in channel in time. [1]

One of all possible solutions is not to use only charge of electron (electronics) but also its spin (spintronics) - intrinsic angular momentum, forming its magnetic properties.

This leads to realization of new coupled systems capable of investigation of potential advanced materials in various different ways. In this master's thesis we demonstrate experimental setup build around 10T Oxford instruments cryostat with optical windows (*Spectromag*). It is a Magnetic Circular Dichroism (MCD) spectrometer to which we add new electromagnetic irradiation in microwave frequency range resulting in creation of new ODMR spectrometer. Advantage of this coupled system is its significantly higher sensitivity of measurement (about 8 or 9 orders) than conventional Electron Spin Resonance (ESR) [2, 3]. The source of this sensitivity enhancement is the detection of radiation in visible region of electromagnetic spectrum which is much more sensitive than in the microwave region. In specific systems – pentacene molecule embedded in a *p*-terphenyl system – it is possible to even detect magnetic resonance in individual molecules [4, 5]. Also with possibility of detecting the signals from 10^{10} Hz to 10^{15} Hz there is enormous gain in signal-to-noise ratio which makes study of very small number of defects possible [6–8].

Optically detected magnetic resonance (ODMR) is a powerful technique for a study of spin-dependent processes [9, 10]. The principle of detection is based on the dependence of optical properties on the electron spin polarization of paramagnetic centres which are involved in the optical pumping cycle or a competing spin-dependent non-radiative process [10]. The irradiation of microwaves induce resonant transitions between spin levels of a paramagnetic centre in both ground or excited state. This results in change of electron spin polarization, which then affects optical properties (*absorption and emission spectra*) of studied sample [11].

Magnetism has been known to mankind since the ancient world, and "for millennia interpretations of the nature of this elusive force capable of moving inert bodies have been produced" [12]. Until the first investigation of the relationship between electricity and magnetism in the early nineteenth century by, among others, Oersted, Ampère and Faraday, this interesting attractive force was understood as a soul of inert matter, transforming it into some form of living organism with expressions and desires. [13]

During nineteenth and twentieth centuries, man partially revealed true nature of magnetism, however, magnetic materials were still structurally based on metals or oxides. The first examples of organic based magnetic materials emerged at the end of twentieth century forming a brand new scientific category – molecular magnetism. Molecules with slow relaxation of the magnetization (at low temperatures), behaving as small magnets are a exceptionally interesting area of molecular magnetism. A molecular nanomagnet is and organic molecule with one or more metal ions with unpaired electrons surrounded by bulky ligands, which act as a protective shield of the magnetic core (metal ions) against the surroundings. The best known example of so called single molecule magnet is shown in the figure 1.1. [12, 14]

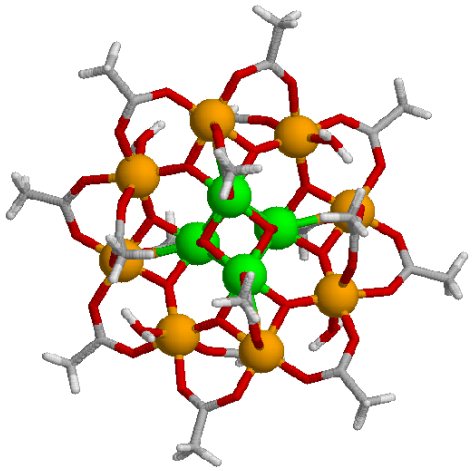

Figure 1.1: The crystal structure of the best known example of single molecule magnet $[Mn_{12}O_{12}(O_2CCH_3)_{16}(H_2O)_4]$ usually abbreviated as $Mn_{12}Ac$. *Picture adapted from [15].*

Magnetism is now understood as one of basic characteristics of matter obtained by intrinsic magnetic properties of elementary particles. Spintronic devices which exploits, spin as a another degree of freedom, can be used in more efficient data storage or data transfer systems [16].

One of principal aims of molecular magnetism is a creation of devices with high density data storage systems together with central processing unit based on quantum bits (qubits) technology.

1.1. Quantum Computing

Among the great challenges of building the quantum computer, which could be used to solve certain problems exponentially faster than classical computer, belongs overcoming the difficulties of their interaction with its environment. Thus, a quantum state of a system is eventually altered. The time needed for a change of the quantum state within the system is called the dephasing time T_2. The obvious path in the molecular magnetism

engineering is to increase the dephasing time to be longer than the time needed to perform several quantum information manipulations. However, we would like the qubits system to be entangled – linked – together. [14, 17, 18]

List of necessary conditions to construct a quantum computer has been described by DiVincenzo [19] as:

1. a scalable physical system with well characterized qubits;
2. the ability to initialize the state of the qubits to a simple fiducial state, such as $|000...i\rangle$;
3. long relevant decoherence times, much longer than the gate operation time;
4. a "universal" set of quantum gates;
5. a qubit-specific measurement capability;
6. the ability to interconvert stationary and flying qubits;
7. the ability faithfully to transmit flying qubits between specified locations.

If we would overcome these problems and create the system of sufficient number of qubits, which could operate without any distraction by quantum decoherence effects, we could use an algorithm that would outperform any classical computer in factoring numbers and in searching a database by exploiting the parallelism of quantum mechanics [20].

In order to use certain algorithms, there are some requirements. For example, Shor's algorithm require both superposition and entanglement of a many particle system [21]. On the other hand, Grover's algorithm needs only the superposition of single particle quantum state [22]. Many others algorithms can be found for example in [23].

Solid-state quantum systems such as nitrogen-vacancy centres in diamond (discussed in section 2.3), nuclear spins in silicon [24, 25], or transition metal complexes [26] belong to important candidates in qubit development. Transition metal complexes, which are further investigated in experimental part, are shown in the figure 1.2.

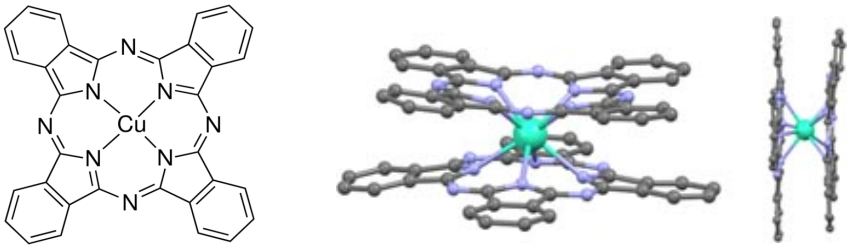

Figure 1.2: Structure of transition metal phthalocyanine complex CuPc and lanthanide based metal complex $ErPc_2$ on the left and right. If we substitute Mn instead of Cu in CuPc, we get MnPc complex. *Pictures adapted from [27] and [28].*

1.2. Data Storage

The magnetism has been known to data storage development since the end of 19th century when Poulsen in 1898 demonstrated at Paris Exposition of 1900 the first magnetic recorder [29]. Through the time of more than 100 years of development, mankind has reached the point where it is possible to store $1{,}3 \cdot 10^{12}$ bits/inch^2 [30]. However, the process of miniaturization has led to devices where the spin plays its key role [16].

Among the first generation of devices exploiting spin, which are in common use, belong the read/write heads of disk drives utilizing the effect of Giant Magnetoresistance (GMR) or Tunnelling Magnetoresistance (TMR). Switchable spin valve cells are the fundamental stones of Magnetic Random-Access Memory (MRAM).

In order to create high density magnetic storage systems, one of the possible ways is to reduce the dimension of one bit, possibly, to store data within a molecule. The future in developing data storage based on single molecule magnets relies on elevation of the blocking temperature. In the following figures, we show some examples of well known single molecule magnets.

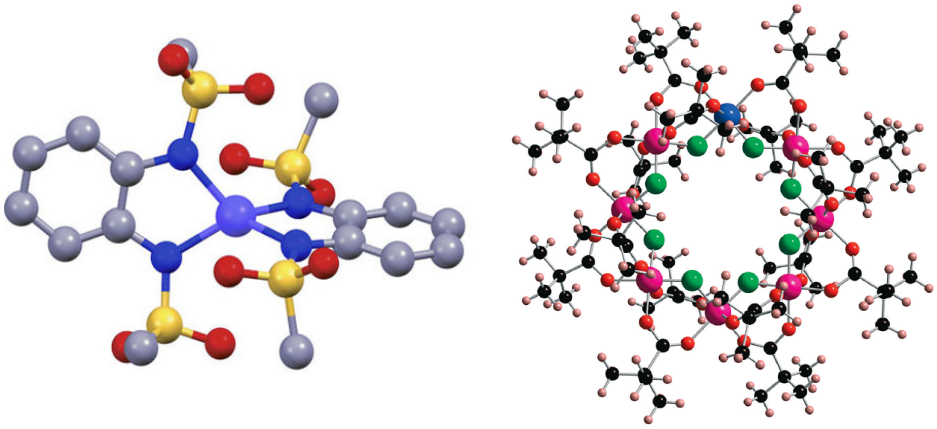

Figure 1.3: Mononuclear, tetrahedrally coordinated cobalt(II) on the left and transition metal complex Cr_7Ni on the right. *Pictures adapted from [31] and [14] respectively.*

2. Magnetic Anisotropy in Matter

"Twinkle twinkle little Spin
Are you single or are you twin?
Are you real or are you false?
How I crave your resonant pulse"

John A. Weil
In Prologue of [32]

Magnetic anisotropy is the directional dependence of magnetic moment of magnetic carriers in matter. The magnetic moment will tend to align in an energetically favourable direction of magnetization, called an "easy axis". Among other energies, magnetic anisotropy forms the hysteresis loops of matter. Magnetization curves define the possibility of application. To retain memory hard magnetic materials are desired.

The characterization of the material's magnetic properties can be done by defining the electron configuration and energy transitions between the spin states by, for example, magnetic resonance spectroscopy methods.

2.1. Magnetic Resonance

Magnetic resonance is mainly used for research or imaging purposes. There are two elementary particles – electron and atomic nucleus – which we exploit for their certain magnetic properties and use them to determine physical and chemical characteristics. However, in the following text, we will focus only on magnetic characteristics of electrons.

A negatively charged particle moving in a circular orbit around a fixed centre (shown in the figure 2.1) has both an angular momentum $\vec{L}$ and a magnetic dipole moment $\vec{\mu}$. Direction of vectors $\vec{L}$ and $\vec{\mu}$ are opposite, because of the negative charge.

The model described in the figure 2.1 is strictly classical and does not accurately represent electron in atom. The rigid orbit model has been replaced by the probability density model. However, in general, every quantum state of an electron in atom posses an orbital angular momentum $\vec{L}$ and a corresponding orbital magnetic dipole moment $\vec{\mu_L}$. Every electron, whether trapped in atom or free, has a spin angular momentum $\vec{S}$ and a corresponding spin magnetic dipole moment $\vec{\mu_S}$. [33]

2.1.1. Orbital Angular Momentum and Magnetic Dipole Moment

The magnitude L of $\vec{L}$ of electron in an atom is quantized as

$$L = \sqrt{l(l+1)}\hbar \tag{2.1}$$

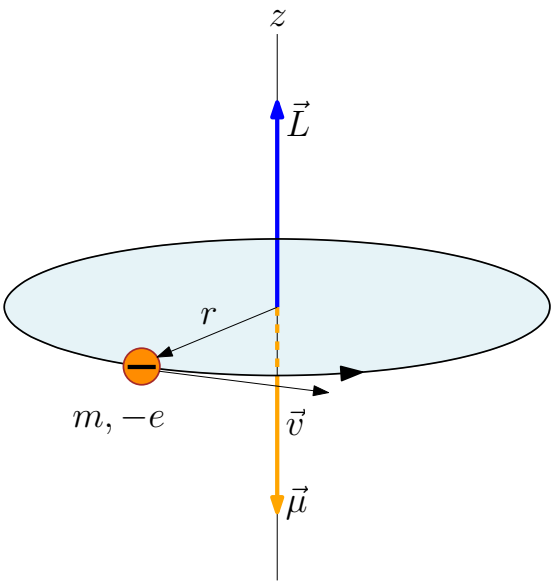

Figure 2.1: A clasical model of particle of mass m and charge $-e$ moving in a circle of radius r with speed v. Moving particle posses an angular momentum $\vec{L}$ given by $\vec{r} \times \vec{p}$, where $\vec{p}$ is its linear momentum $\vec{p} = m\vec{v}$. Particle's motion is equivalent to a current loop with an associated magnetic moment $\vec{\mu}$ that has opposite direction to $\vec{L}$.

where l is the orbital quantum number and $\hbar$ is reduced Planck constant h ($\hbar = h/2\pi$). The magnitude of orbital magnetic dipole moment $\vec{\mu_L}$ is related to the magnitude of quantized angular momentum L by

$$\mu_L = \frac{e}{2m}\sqrt{l(l+1)}\hbar. \tag{2.2}$$

Neither $\vec{\mu_L}$ nor $\vec{L}$ can be measured, however we can measure their components along a given axis, lets assume z axis, which will be later connected with the external magnetic field $\vec{B}$. [33] Components L_z of the angular momentum are quantized and determined by

$$L_z = m_l\hbar, \tag{2.3}$$

as do components $\mu_{L,z}$ by

$$\mu_{L,z} = -m_l\mu_B, \tag{2.4}$$

in which m_l is the orbital magnetic quantum number and μ_B is the Bohr magneton given by

$$\mu_B = \frac{e\hbar}{2m}. \tag{2.5}$$

2.1.2. Spin Angular Momentum and Magnetic Dipole Moment

The magnitude S of $\vec{S}$ of any electron is quantized and depends on a spin quantum number s by

$$S = \sqrt{s(s+1)}\hbar, \tag{2.6}$$

which is always $\frac{1}{2}$ for single electron. As we discussed in the previous section, spin angular momentum has also a corresponding spin magnetic dipole moment $\vec{\mu_S}$. The magnitude of μ_S is quantized and given by

$$\mu_S = g_e\frac{e}{2m}\sqrt{s(s+1)}\hbar, \tag{2.7}$$

where g_e is known as the g-factor (Landé factor) of electron.

We are not able to measure $\vec{S}$ or $\vec{\mu_S}$ but again, we can detect its component along any given axis. The component of $\vec{S}$ for single electron measured along axis z is quantized and depends on a spin magnetic quantum number m_s by

$$S_z = m_s\hbar. \tag{2.8}$$

This quantum number can have only two values: $m_s = +\frac{1}{2}$ (called spin up) and $m_s = -\frac{1}{2}$ (called spin down).

The components $\mu_{S,z}$ of the spin magnetic dipole moment are also quantized and set by

$$\mu_{S,z} = -g_e m_s \mu_B. \tag{2.9}$$

For systems of two or more electrons, s is 1, $\frac{3}{2}$, 2, ... The spin angular momentum vectors and their projected components for $s = \frac{1}{2}$, 1 and $\frac{3}{2}$ are represented in the figure 2.2.

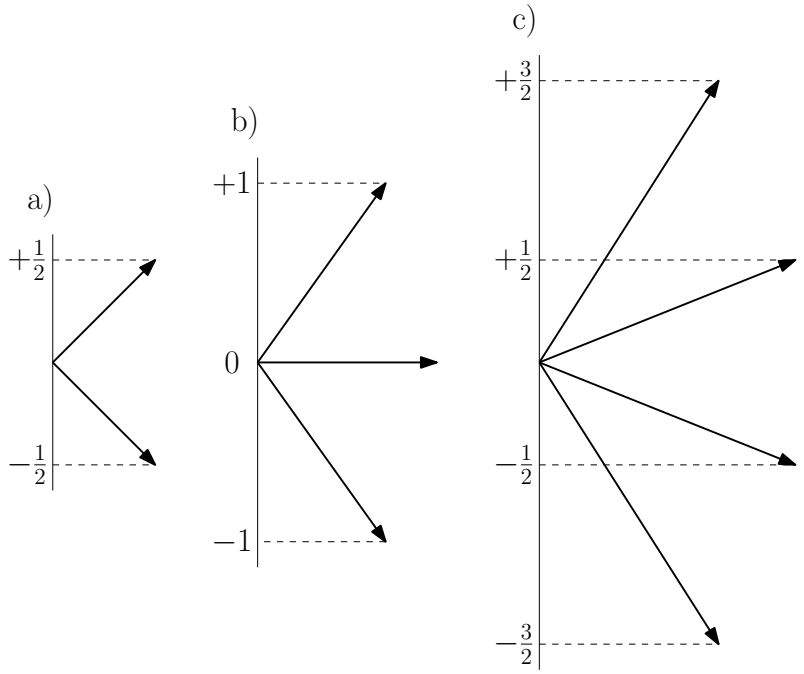

Figure 2.2: Allowed values (in units of $\hbar$) of the total spin angular momentum $S = = \sqrt{s(s+1)}\hbar$ and its vertical components S_z along a fixed direction for a) $s = \frac{1}{2}$, b) $s = 1$ and c) $s = \frac{3}{2}$.

The multiplicity rule of states is determined as $(2s+1)$. States with $S = \frac{1}{2}$ are referred to as doublet states (multiplicity is equal to 2). States with $S = 1$ are called triplet states.

The total magnetic moment $\vec{J}$ is composed of spin $\vec{S}$ and orbital moment $\vec{L}$ by equation

$$\vec{J} = \vec{L} + \vec{S}. \tag{2.10}$$

2.1.3. Electron Paramagnetic Resonance

In external magnetic field electron has two degenerate eigenstates depending on the orientation of spin magnetic dipole moment $\vec{\mu_S}$, which can be in the direction or opposite the direction of $\vec{B}$, described in the figure 2.3. Energy associated with the orientation

of spin magnetic dipole moment $\vec{\mu_S}$ in external magnetic field is $\vec{B}$ is $E = -\vec{\mu} \cdot \vec{B}$. If the magnetic field $\vec{B}$ is directed along the positive direction of axis z then the energy for each alignment (up and down states) is given by $E = m_s g_e \mu_B B$. Therefore the separation energy between those two states is

$$\Delta E = g_e \mu_B B \tag{2.11}$$

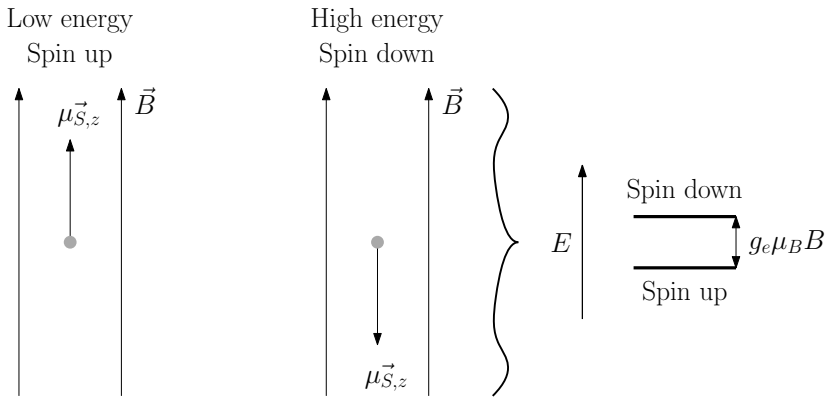

Figure 2.3: Scheme of the z component of $\vec{\mu}$ in spin up – lower energy state and in spin up – higher energy state together with energy diagram showing the energy $g_e \mu_{S,z} B$ necessary for spin flip mechanism.

Energy difference described by equation 2.11 can be used for spectroscopy measurement by photon with energy $E = hf$. If we satisfy condition

$$\Delta E = g_e \mu_B B_0 = hf, \tag{2.12}$$

where f is the frequency of excitation photon and B_0 is the specific strength of magnetic field. Such absorption is called magnetic resonance. From now on, we will consider only electrons and the corresponding magnetic resonance – electron paramagnetic resonance (EPR). The distance between states is increasing accordingly with the external magnetic field (Zeeman effect) as can be seen in the figure 2.4.

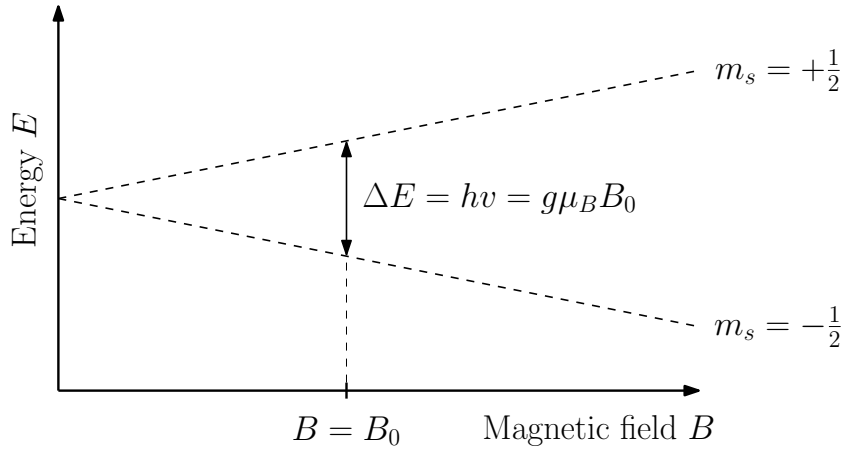

Figure 2.4: Zeeman splitting for an electron spin state $m_s = \pm\frac{1}{2}$ in an increasing strength of external magnetic field B. The energy difference between two spin states (spin up and down) is given by equation 2.12 at the specific magnetic field B_0.

Experimentally, equation 2.12 permits a large combination of frequency and magnetic field values but the great majority of EPR measurements are made in GHz microwave frequency region with fields corresponding up to approximately 40 T. Furthermore, EPR spectra can be generated by either varying the photon frequency incident on a sample while holding the magnetic field constant or doing the reverse. In practice, it is usually the frequency that is kept fixed.

The whole chapter can basically be used also for nuclear magnetic resonance (NMR) spectroscopy. The main difference between EPR and NMR is in the magnitude of the magnetic interaction which corresponds to the gyromagnetic ratio γ, described in the following text.

When we put any charged particle with its characteristics into external magnetic field $\vec{B}$, the total magnetic moment $\vec{J}$ starts to precess around the direction of the applied field $\vec{B}$ with an angular frequency known as the Larmor frequency. The whole situation is illustrated in the figure 2.5.

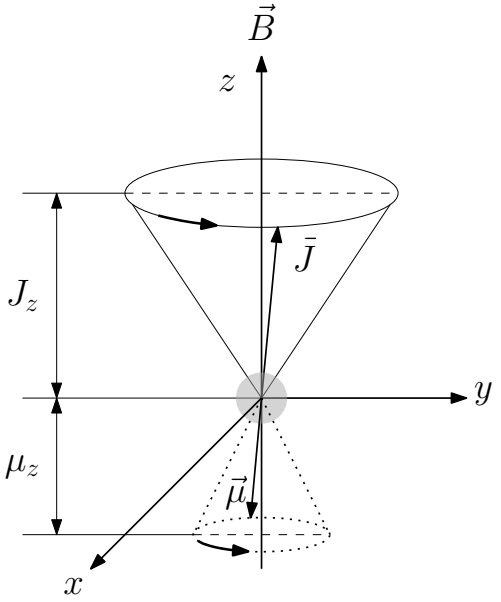

Figure 2.5: The precession model for the behavior of electron with the total angular momentum vector $\vec{J}$ and the total (effective) magnetic moment vector $\vec{\mu}$ together with their z-components in a static magnetic field $\vec{B}$.

$$\omega = -\gamma B, \tag{2.13}$$

where ω is the angular (Larmor) frequency, B is the magnitude of applied magnetic field and γ is the gyromagnetic ratio which is determined by

$$\gamma = \frac{qg}{2m}, \tag{2.14}$$

where q is the charge, g is g-factor and m is mass of either the electron or nucleus that is about three orders of magnitude higher than for electron. This difference has an influence on resonance frequency that is for NMR in region of MHz. [32, 34]

2.2. Molecular Magnetism

As it was discussed in the chapter 1, the first mention about molecular magnetic materials was at the end of twentieth century [12]. After the revelation of organic compounds that could conduct electricity or be even superconducting, a large effort has been put in investigation of organic conductors and to the possibility of tuning its properties into organic molecular magnets.

A big step towards so-called single molecule magnets (SMMs) was made in the beginning of 1990s when the first study of high-nuclearity spin clusters emerged. Under the expression "spin clusters" we hide system containing not only clusters of transition metal ions but also organic radicals (and also both coupled together) [35].

The first observation of magnetic hysteresis that has purely molecular origin [36] took place in 1993. It created a big buzz around SMMs and the vision of ultra high density magnetic data storage devices caught attention of many scientists.

In the figure 2.6 you can find a scheme, showing what kind of effect has size of "material" (S stands for the number of spins) on the magnetization dynamics and hysteresis loop.

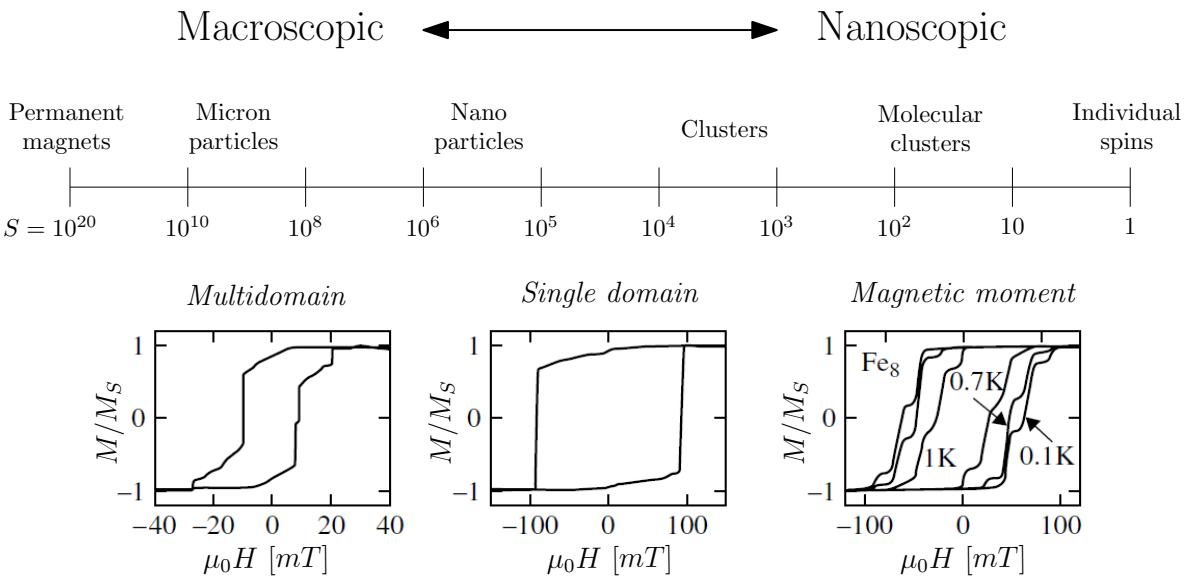

Figure 2.6: Scheme with the influence of size effect of "material" (S stands for the number of spins) on the magnetization dynamics. With macroscopic magnets the hysteresis loop goes smoothly as large number of domains (multidomain) are contributing to the magnetization of the whole system. When we reduce size to single domain magnet the hysteresis loop has sharp step of increasing magnetization. When we observe hysteresis of molecules at low temperatures the observed steps correspond to increase in the rate of the magnetisation change when there is an energy coincidence between levels on both sides of the potential barrier (described in figure 2.7). *(Edited figure, original from [12]).*

Large macroscopic magnets contain at least $S = 10^{20}$ of individual spins, coupled together so they will respond all together to external stimulation. By forming domains, regions of matter where all individual magnetic moments are parallel (or anti-parallel) to each other, the magnetic energy is kept at minimum. The sum of magnetic moments of domains is zero, when there is no external magnetic field. Eventually, there is a saturation point, where all the individual magnetic moments are parallel. With decreasing field the formation of domains is not strictly reversible. When the external magnetic field is turned

off, there is a remanent magnetization in the sample. This value is used to classify the type of bulk magnet and tells us whether it could be used for data storing. Hysteresis loop, typical for multidomain samples, is shown in the figure 2.6 on the left.

If we try to reduce the size of magnetic "material", limit is reached when it is no longer energetically better to form large domains – particle goes single domain [12] (middle part of the figure 2.6).

When we continue on with reducing dimensions, effect of magnetic anisotropy (referred to as A) begins to have its influence, meaning that energy of the system is a function of the orientation of the magnetic moment (easy and hard axis), shown in the figure 2.7. When we get to single molecules, together with low temperatures, the barrier of reorientation of the magnetization (ΔE in the figure 2.7) is comparable to the thermal energy, which is shown in the hysteresis loop in the right corner of the figure 2.6. At low temperatures only the ground spin state is thermally populated and the relaxation time for spin reorientation into the equilibrium state increases. The steps observed in the hysteresis loop correspond to increment of the rate of the magnetisation change when there is an energy coincidence between levels on both sides of the potential barrier.

If we prepare the sample with "down" magnetization state (left well of the figure 2.7 marked with big dark grey arrow in black circle) some of the electrons have enough energy to overcome the barrier. After adequate time half of electrons will be in the left ("down" state) and half in the right well ("up" state), resulting in lowest energy of the system. If no external field is applied, system will not be magnetized and will like a paramagnet. The relaxation of the system can go via three processes: thermal relaxation, thermally-(phonon-) assisted tunnelling or ground state tunnelling, all described in the figure 2.7 by red, blue or green arrows respectively [37].

When we apply external magnetic field, one of two wells will lower its energy while the other will increase it [12]. This causes a different population of spin states resulting in magnetization of the molecule. Since the response to the external field comes from all individual magnetic centres, it is very large. Therefore, these particles are called superparamagnets [12].

2.2.1. Single Molecule Magnets

A single molecule magnet (SMM) is a molecule that behaves, as one could deduce from its name, as an individual nanomagnet. Because of its small size and precise characterizability, molecular nanomagnets exhibit many fascinating quantum phenomena. SMMs with their capabilities and characteristics may find application in high-density magnetic storage or as qubits (fundamental unit of quantum information). [38]

Among the most important properties of SMM belongs a large spin ground state S together with a negative Zero-Field Splitting (ZFS), which is represented by D. This, together with an easy-axis magnetisation create a large energy barrier ΔE for magnetization reversal processes, which leads to slow relaxation. Below a certain blocking temperature (usually referred to as T_B) SMM behave as a superparamagnet. [12, 34]

As the result of negative ZFS term D inside the ground state multiplet, is inverted – in energy the highest spin state level is $M_S = 0$ and the lowest is $M_S = \pm S$ as can be seen in the figure 2.7. The energy difference is approximately equal to $\Delta E \approx DS^2$. For the possibility of storing information in SMMs high energy barrier ΔE is crucial.

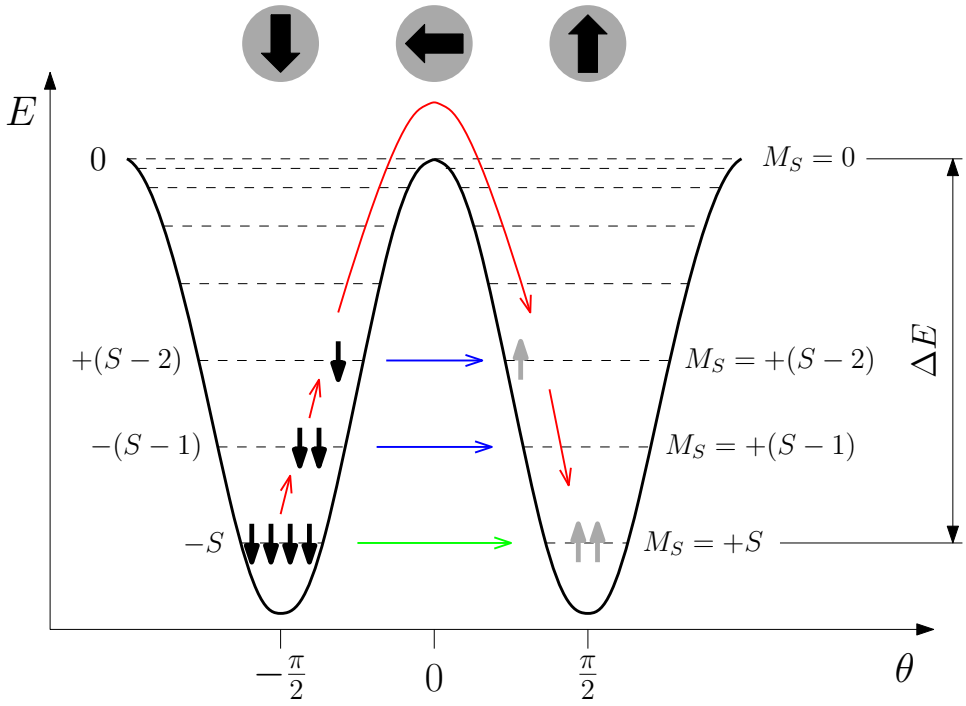

Figure 2.7: Energy of an Ising type single molecule magnet as a function of the angle of the magnetization from the easy axis (see the big arrows on the top). Scheme is also showing magnetisation and relaxation behaviour of SMM of a total spin S at a finite temperature and at zero magnetic field B. After the polarisation of SMM into $-S$ state the whole system starts to relax by both ground state or thermally assisted quantum tunnelling (blue arrows) and by thermal relaxation process (red arrows). The relaxation time (referred to as T_1) depends on height of the potential barrier ΔE.

2.3. Nitrogen-Vacancy Centre in Diamond

The nitrogen-vacancy (NV) colour centre in diamond belongs to one of the most important physical systems in terms of quantum technologies like information processing and communications, as well as a testing structure for the study of entanglement in quantum mechanics [39].

A nitrogen-vacancy centre in diamond is an atomic defect consisting of substitutional nitrogen (N) combined with a vacancy (V) in one of the nearest neighbouring sites of the diamond crystal lattice. Until this date, two different forms of this defect are identified – the neutral state NV^0 and the negatively charged state NV^- [40]. However, the neutral state of NV has not yet been successfully used in any kind of demonstration because so far no reported observation of optical readout [39]. On the other hand, the NV^- is used in a great deal of experiments that demonstrated its abilities even at room temperature [41, 42].

Beyond quantum information processing, there are many other important applications of NV^- centres, for example, in room-temperature nanoscale magnetometry [43–45], biomagnetometry [46], electrometry [47] and nanoscale high-sensitive thermometer [48].

The energy band diagram shown in the figure 2.8 describes the possibility of optical detection via the electron spin polarization using the optical pumping cycle. The NV^- centres are usually studied by photoluminiscence where the centre is excited by $532\,\mathrm{nm}$ laser (green arrow) and red fluorescence light $638 - 800\,\mathrm{nm}$ is detected (red arrow). The optical transitions are spin-conserving, however, non-radiative transitions (black arrows) do not conserve spin, and thus, allow the possibility to polarize the NV^- centres in the $m_s = 0$ spin state. When we then apply microwave irradiation with frequency $f = \\ = 2{,}87\,\mathrm{GHz}$ (blue double sided arrow) the decrease of the photoluminiscence gives rise to ODMR signal. [49, 50]

2.4. Magnetic Circular Dichroism

As it was first shown by Faraday, optical activity is induced in matter by magnetic field. He found that a polarization plane is rotated after passing through lead borate glass when external magnetic field is applied. The rotation is general property of matter and is quantitatively described as

$$\Phi = VBd, \tag{2.15}$$

where Φ is the rotation of the polarization plane, V represents the Verdet constant which is specific for material and is a function of frequency, B is the magnetic flux density in the direction of propagation and d is the length of the path where the light and magnetic field interact. The scheme of polarized light passing the distance d through optically active material is shown in figure 2.9. [51]

All matter causes optical rotation when there is a difference between refractive indices for left circularly polarized (lcp) and right circularly polarized (rcp) light. Very low symmetry of individual molecules, or in the unit cell of crystal, gives rise to a natural optical activity. In magnetic optical rotation (MOR) the difference is created by the applied longitudinal magnetic field (external or internal; set by equation 2.15) causing left and right handed circular motions being inequivalent [51, 52]. Also the absorption coefficients for lcp and rcp differ.

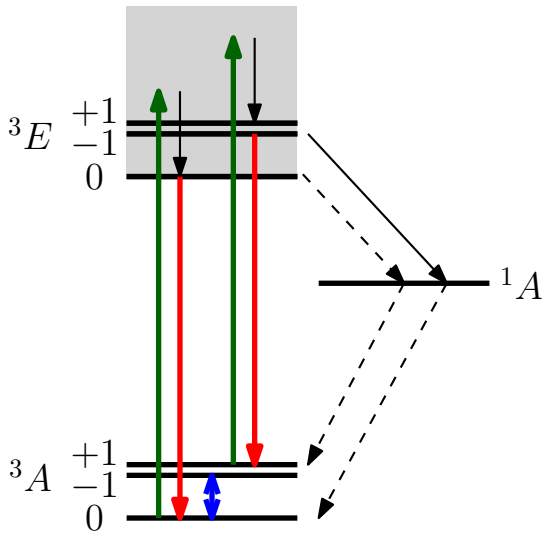

Figure 2.8: Energy band diagram of the NV^- centre describing the optical excitation and emission cycle. ^{3}A and ^{3}E are the triplet ground and excited states. ^{1}A is metastable singlet state. Spin-conserving optical readout is usually carried out by 532 nm excitation laser (green arrow) and red fluorescence light $638 - 800$ nm is detected (red arrow). Non-radiative transitions are represented by black lines - the spin levels $m_s = \pm 1$ are coupled to the metastable level strongly (solid arrow) than the $m_s = 0$ (dashed arrow). Spin manipulation in the ground state ^{3}A is influenced by microwave irradiation (blue double sided arrow) with frequency of $\approx$ 2,87 GHz at zero magnetic field. The microwave-induced resonant frequency transition leads to decrease of photoluminiscence and gives rise to ODMR signal.

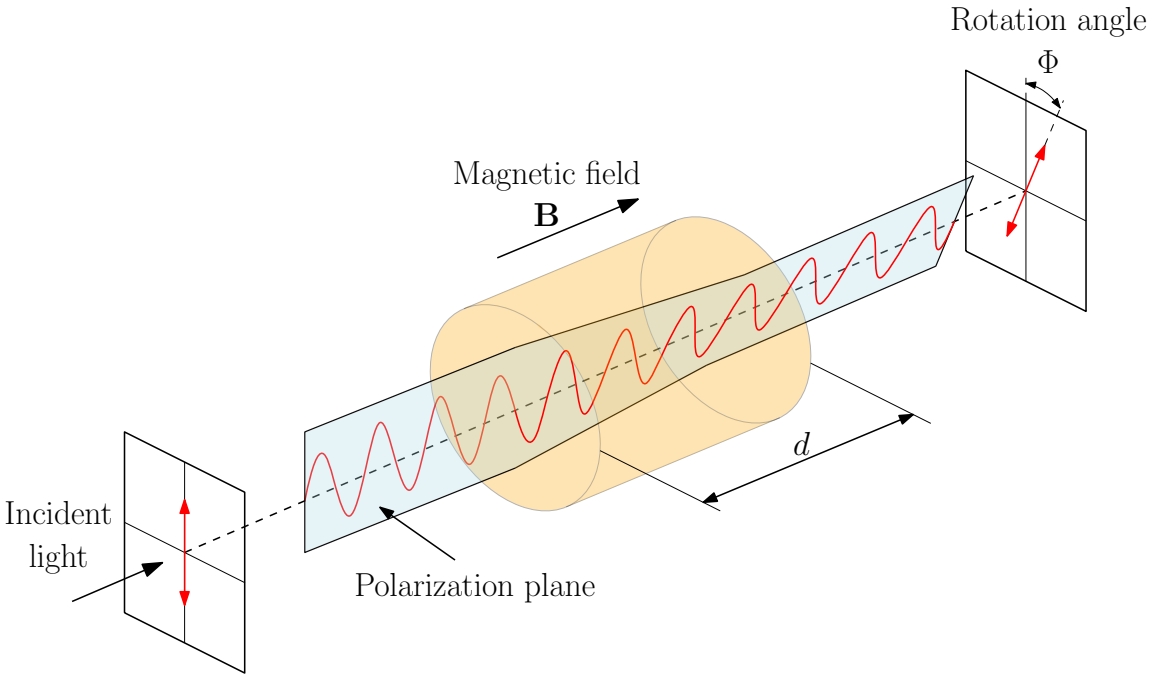

Figure 2.9: Scheme of Faraday rotation. Linearly polarized light is passing though the distance d in optically active material in magnetic field B that is parallel to the optical axis. This causes a rotation of polarization by an angle Φ described by equation 2.15.

Magnetic circular dichroism (MCD) spectroscopy is than based on the measurement of the difference in absorption between lcp and rcp light, which is induced in a sample by strong magnetic field oriented parallel to the direction of light propagation (birefringence) [52, 53].

2.4.1. General Theory

The difference of absorption, or dichroism, is defined by convention as

$$\Delta A = A_- - A_+, \tag{2.16}$$

where A_- is lcp absorption and A_+ is rcp absorption. It should be drawn to attention that ΔA differs from conventional absorption spectrum. The measured quantity has a sign which is dependent on whether A_- or A_+ is larger. This main characteristic of MCD adds another dimension to measurement and provides a much better resolution compared to conventional absorption spectroscopy methods. [53]

The differences in absorption of lcp and rcp light give rise to elliptically polarized light which is being radiated from the sample. The ellipticity θ is proportional to the differential absorption by factor [54]

$$\theta = \Delta A \cdot 32{,}98. \tag{2.17}$$

At low temperatures, MCD spectroscopy allows the determination of excited term crystal field splittings, however, different shapes of the signal can be measured depending on the nature of the states origin. The general expression of the MCD signal is set by

$$\frac{\Delta A}{E} = \gamma \mu_B B \left[A_1 \left(-\frac{\partial f(E)}{\partial E} \right) + \left(B_0 + \frac{C_0}{k_B T} \right) f(E) \right], \tag{2.18}$$

where γ is a general spectroscopic constant, $f(E)$ is a line-shape function and A_1, B_0 and C_0 represent the MCD terms. The C term is essentially a characteristic of paramagnetic molecules, A_1 and B_0 exist for all molecules and make MCD universal phenomenon which occurs in all matter. [53, 55, 56]

The A term can be observed in measurement when degenerate states are involved in the transition. The magnetic field lifts the degeneracy resulting in absorption of lcp and rcp with different energies. Whole transition processes are described in the figure 2.10 part a) where a simple example of transition between non-degenerate ground state ^1S to threefold degenerate excited state ^1P are shown. The signal has usually derivative shape.

Field induced mixing of states gives rise to the B term while the energy between the ground and excited states should be high enough resulting in highly uneven distribution of population. It has usually weak absorption-like signal shape. Both A and B terms are independent of temperature.

The greatest source of information in respect of SMMs MCD spectroscopy is the C term occurring when the Zeeman splitting of the degenerate ground state is present. Due to the Maxwell-Boltzmann population distribution among Zeeman sub-levels, the temperature dependence can be observed. The C term has usually asymmetric absorption-like shape.

The measurements of paramagnetic centres take place at low temperatures (liquid helium temperature $\approx 4\,\mathrm{K}$) where the C term dominate the MCD spectrum and important information about the electronic ground state can be acquired.

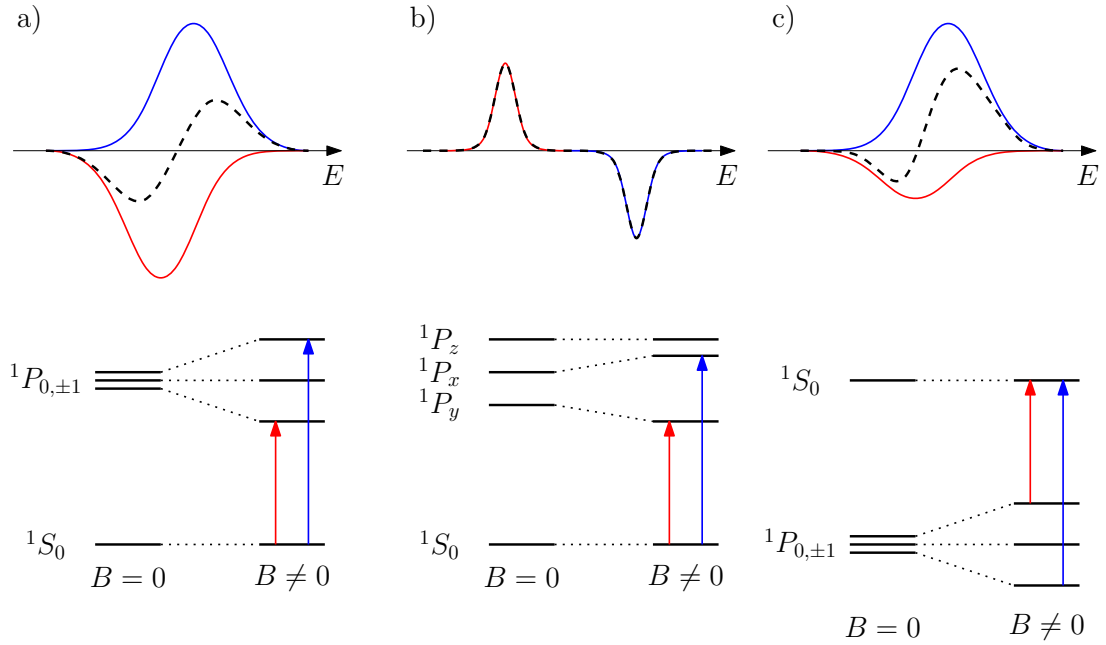

Figure 2.10: Scheme of different MCD terms. Blue and red lines represent the absorption of lcp and rcp light respectively. In the figure a) the A term (also called Faraday) is shown. The differential absorption is due to lifted degeneracy of the excited state resulting in different energy absorption. The B term, illustrated in b), can be observed when the field induced mixing of states is involved. The most important C term, in respect of SMMs, is present due to the degeneracy of ground state.

2.4.2. MCD Spectrometer Setup

The typical visible light MCD spectrometer consists of a conventional CD spectrometer and magnet. The setup in question is located at the Institute of Physical Chemistry, University of Stuttgart, Germany. Scheme of the experimental assembly is described in the figure 2.11.

The CD spectrometer *Aviv Model 42 Spectrometer* consists of the light source, monochromator, polarizer for generation of linearly polarized light, photoelastic modulator (PEM) for generation of circularly polarized light and the detector. It allows measurements in wavelength range from 200 to 2 000 nm with resolution of up to 0,1 nm.

Sample is inserted into split-pair superconducting magnet *Spectromag, Oxford Instruments* capable of generating magnetic field up to 11 T. It is a cryogenic magnet which can provide sample temperatures from 1,5 K to 300 K.

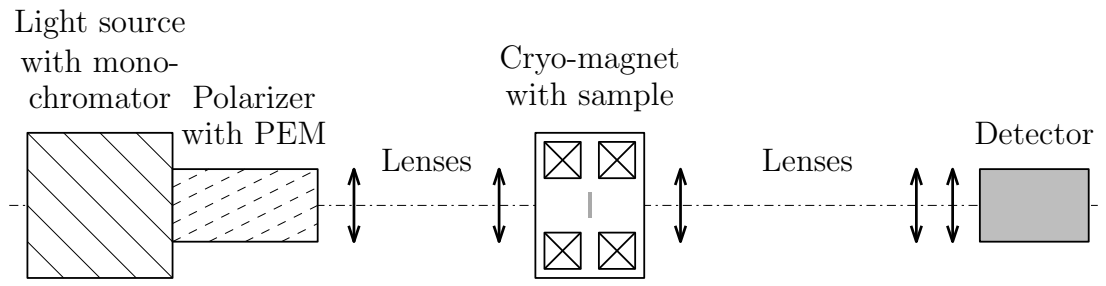

Figure 2.11: Scheme representing the MCD spectrometer assembly.

2.5. Optically Detected Magnetic Resonance

Optical detection of EPR is very different from conventional methods by being double resonance experiment – microwave induced changes of population of Zeeman levels is indirectly connected to a change in some property of light. With the gain in sensitivity by several orders of magnitude [57] it is possible to study a very small number of defects and their influence on bulk properties of solids [3, 7, 58–60]. Optical properties can be thus connected with energy levels of defects influencing the "gap properties", such as electrical properties (specific interest in semiconductor physics). Or another particularly interesting spin-dependent physical system is the NV colour centre in diamond (discussed in section 2.3).

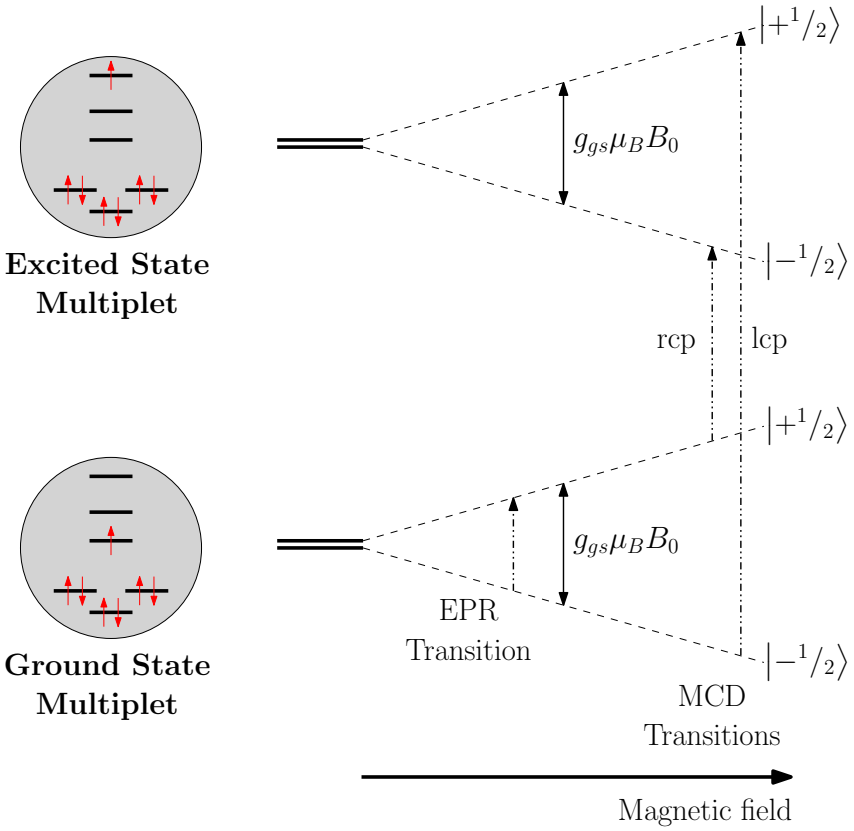

Figure 2.12: Resonant transitions between spin levels in both ground or excited state of spin 1/2 system. If the EPR conditions are fulfilled they cause a change in MCD signal.

It is one of the most powerful and informative techniques for a study of spin-dependent processes [9, 10, 61–63]. The detection is based on a change of optical properties due to electron spin polarization of paramagnetic centres involved in optical pumping cycle or spin-dependent non-radiative process. [10, 57]

Direction of spin polarization can be changed by microwave-induced resonant transition between Zeeman levels either in ground or excited state, but also by cross relaxation – higher energy state of one molecule is distributed to intermediate excited state of both molecules [11]. Optically detected cross relaxation has been observed in many systems both via MCD of absorption [57, 58, 64] and via photoluminescence [65–67].

Thus, MCD-ODMR links the benefits of electronic absorption and EPR-spectroscopy, since it allows the simultaneous investigation of electronic ground and excited states.

3. Quasi-Optical Propagation

The theory of quasi-optical propagation covers wide range of wavelengths between ray and diffraction optics. Ray optics deals with radiation where we assume that wavelength $\lambda \to 0$ and all components like lenses, mirrors and apertures are large enough so we do not have to consider the effects of finite wavelengths. On the other hand, using diffraction optics which operate with wavelength limit $\lambda \approx$ system dimensions, is relatively difficult and time consuming [68].

Quasi-optics stand between these two cases, therefore, it includes the important and realistic situation where the diameter of beam of radiation is comparable or slightly bigger than wavelength. The diffraction is also a part of this formalism but its role is not that restrictive.

The objective of this chapter is to describe the formalism of propagation of Gaussian beam for wavelengths of several millimetres. Most of the information are gained from the work of P. F. Goldsmith [68] and my supervisor's thesis [34]. This will help us to find optimal solution for system which will guide microwave beam to the dichroic mirror, where it will be coupled into path of visible light beam, resulting in irradiation of the sample by both electromagnetic radiations.

3.1. Gaussian Beam

3.1.1. Paraxial Wave Equation

To form the basis for Gaussian beam propagation we develop a paraxial wave equation for a beam with well defined direction of propagation but also with some small transverse variation (unlike a plane wave where the distribution of field amplitude is independent of position). The beam source is defined as a region of finite extent.

Wave propagating in a uniform medium is described by a Helmholtz equation

$$(\nabla^2 + k^2)\psi = 0, \tag{3.1}$$

where ψ is any component of E or H. We assume a time variation $\exp \mathrm{i}\omega t$ at given angular frequency ω and wave number $k = 2\pi/\lambda$. Even if assume beam of radiation similar to a plane wave but we allow some variation perpendicular to the axis of propagation, we can still assume that electric and magnetic fields are perpendicular to the direction of propagation and also to each other. The distribution of electric field of any component can be written as

$$E(x,y,z) = u(x,y,z)\exp(-ikz)\exp(i\omega t), \tag{3.2}$$

where $u(x,y,z)$ is complex scalar function of perpendicular variation of the field and the direction of propagation is in the positive direction of z. The Helmholtz equation in rectangular coordinates is

$$\frac{\partial^2 E}{\partial x^2} + \frac{\partial^2 E}{\partial y^2} + \frac{\partial^2 E}{\partial z^2} + k^2 E = 0. \tag{3.3}$$

If we substitute our quasi-plane wave solution into equation 3.3 we obtain reduced wave equation

$$\frac{\partial^2 u}{\partial x^2} + \frac{\partial^2 u}{\partial y^2} + \frac{\partial^2 u}{\partial z^2} - 2ik\frac{\partial u}{\partial z} = 0. \tag{3.4}$$

Now we introduce the paraxial approximation where we assume that variation of the amplitude $u(x,y,z)$ along the direction of propagation will be small over a distance compared to a wavelength and also the axial variation will be small compared to perpendicular variation in this direction.

From the first statement we can conclude that in magnitude

$$\frac{\Delta(\partial u/\partial z)}{\Delta z}\lambda \ll \frac{\partial u}{\partial z}, \tag{3.5}$$

which means that in equation 3.4 the third term is small compared to the fourth term. From the second statement we can conclude that the third term is also smaller compared to the first two. This leads to paraxial wave equation in rectangular coordinates

$$\frac{\partial^2 u}{\partial x^2} + \frac{\partial^2 u}{\partial y^2} - 2ik\frac{\partial u}{\partial z} = 0. \tag{3.6}$$

Solutions for paraxial wave equation are Gaussian beam modes. The range of usage for this approximation is not rigorously stated. Generally, we can rely on it when the angular divergence of the beam is within 0.5 rad (about 30°) of the axis of propagation.

3.1.2. Fundamental Mode in Cylindrical Coordinates

Cylindrical coordinates are preferred choice for systems with axial symmetry (such as lenses, horn antennas, etc.). In this system of coordinates, r represents perpendicular distance from propagation axis z (radius) and φ is the angular position. Paraxial wave equation in cylindrical coordinates is

$$\frac{\partial^2 u}{\partial r^2} + \frac{1}{r}\frac{\partial u}{\partial r} + \frac{1}{r}\frac{\partial^2 u}{\partial \varphi^2} - 2ik\frac{\partial u}{\partial z} = 0, \tag{3.7}$$

where u is a function of r , φ and z ($u \equiv (r,\varphi,z)$). For our application we assume axial symmetry meaning that u is independent of φ. With this condition we get axially symmetric paraxial wave equation

$$\frac{\partial^2 u}{\partial r^2} + \frac{1}{r}\frac{\partial u}{\partial r} - 2ik\frac{\partial u}{\partial z} = 0. \tag{3.8}$$

Simplest solution for this equation can be

$$u(r,z) = A(z)\exp\left[\frac{-ikr^2}{2q(z)}\right], \tag{3.9}$$

where A and q are complex functions dependent on z only and will be determined in the following text. Also notice the similarity of solution for axially symmetrical paraxial wave equation with Gaussian distribution $f(r) = f(0)\exp[-(r/r_0)^2]$. In order to obtain A and q from equation 3.9 we substitute solution for u into equation 3.8 and we get

$$-2ik\left(\frac{A}{q}+\frac{\partial A}{\partial z}\right)+\frac{k^2r^2A}{q^2}\left(\frac{\partial q}{\partial z}-1\right)=0. \tag{3.10}$$

This equation must be satisfied for all r as well as all z. The first part depends only on z and the second one on r and z, the two part must individually be equal to zero. This gives us

$$\frac{\partial q}{\partial z}=1 \tag{3.11}$$

and

$$\frac{\partial A}{\partial z}=-\frac{A}{q}. \tag{3.12}$$

Solving the equation 3.11 we get

$$q(z)=q(z_0)+(z-z_0). \tag{3.13}$$

Now we put our reference position along the z axis to be $z_0 = 0$, which leads into

$$q(z)=q(0)+z. \tag{3.14}$$

The function q from equation 3.14 is called Gaussian beam parameter and since it often appears in equations like 3.9 it is usually written as

$$\frac{1}{q}=\left(\frac{1}{q}\right)_r-i\left(\frac{1}{q}\right)_i, \tag{3.15}$$

where the terms r and i are real and imaginary part of $1/q$. When we substitute this into equation 3.9 than the exponential term is

$$\exp\left(\frac{-ikr^2}{2q}\right)=\exp\left[\frac{-ikr^2}{2}\left(\frac{1}{q}\right)_r-\frac{kr^2}{2}\left(\frac{1}{q}\right)_i\right], \tag{3.16}$$

where the imaginary part has the form of phase variation. This can be proved by the following assumption described also by figure the 3.1. We have and equiphase surface with radius of curvature R and we define phase variation relative to a plane for a fixed value of z to be $\phi(r)$. Now, in the limit $r \ll R$, $\phi(r)$ is approximately equal to

$$\phi(r)\cong\frac{\pi r^2}{\lambda R}=\frac{kr^2}{2R}. \tag{3.17}$$

This means that we can identify the real part of Gaussian beam parameter with the radius of curvature of the beam

$$\left(\frac{1}{q}\right)_r=\frac{1}{R}. \tag{3.18}$$

Now we implement a Gaussian variation into the second part of the exponential term in equation 3.16. The Gaussian distribution is described as

$$f(r)=f(0)\exp\left[-\left(\frac{r}{r_0}\right)^2\right], \tag{3.19}$$

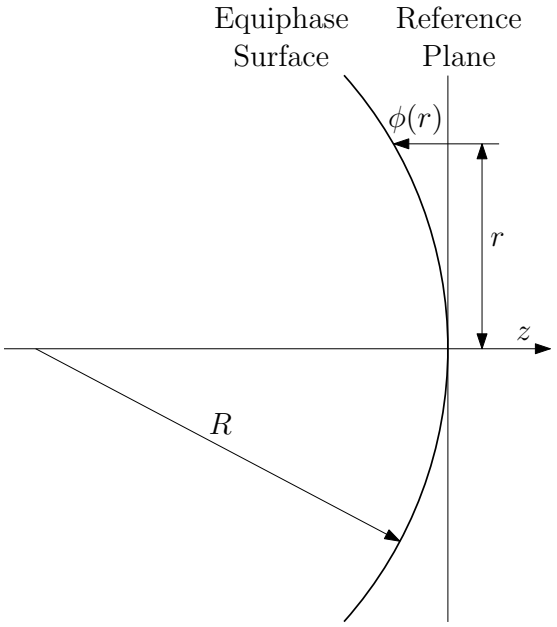

Figure 3.1: Scheme of phase shift of spherical wave relative to plane wave. Phase delay $\phi(r)$ is at distance r from the axis of propagation.

where r_0 is the distance to $1/e$ of relative intensity to the on-axis value. In order to make the mentioned second part of the exponential to have this form we take

$$\left(\frac{1}{q}\right)_i = \frac{2}{kw^2(z)} = \frac{\lambda}{\pi w^2}, \tag{3.20}$$

with this we can define the beam radius w in which the relative intensity drops to $1/e$ to its on-axis value.

Defining previous claims, we can rewrite the Gaussian beam parameter into

$$\frac{1}{q} = \frac{1}{R} - \frac{i\lambda}{\pi w^2}, \tag{3.21}$$

where both R and w are functions of z.

With this knowledge, if we substitute $z = 0$ and choose w_0 as $w_0 = \sqrt{\dfrac{\lambda q(0)}{i\pi}}$ into equation 3.9, we yield the relative field distribution to be

$$u(r,0) = u(0,0)\exp\left(\frac{-r^2}{w_0^2}\right), \tag{3.22}$$

where the term w_0 is called the beam waist radius. From previous definition we get also another important expression for q

$$q = \frac{i\pi w_0^2}{\lambda} + z.. \tag{3.23}$$

From expressions 3.20 and 3.23 we obtain radius of curvature R, beam radius w and so called confocal distance z_c to be

$$R = z + \frac{1}{z}\left(\frac{\pi w_0^2}{\lambda}\right)^2 \tag{3.24}$$

$$w = w_0\sqrt{1+\left(\frac{\lambda z}{\pi w_0^2}\right)} \tag{3.25}$$

$$z_c = \frac{\pi w_0^2}{\lambda}, \tag{3.26}$$

where we can see that the beam waist radius w is a point where the radius of curvature is infinite and the value of beam radius is minimal.

To analyse the Gaussian beam equation completely, we use the second obtained equation 3.12. With substituting also term gained from the first equation $\mathrm{d}z = \mathrm{d}q$ we can write

$$\frac{\mathrm{d}A}{A} = -\frac{\mathrm{d}q}{q}, \tag{3.27}$$

solving this equation we can get expression $A(z)/A(0) = q(0)/q(z)$ where if we substitute q from equation 3.23 we yield

$$\frac{A(z)}{A(0)} = \frac{1+\dfrac{i\lambda z}{\pi w_0^2}}{1+\dfrac{\lambda z}{\pi w_0^2}^2}, \tag{3.28}$$

which is convenient to express in a terms of a phasor using $\operatorname{tg}\phi_0 = \lambda z/\pi w_0^2$ as

$$\frac{A(z)}{A(0)} = \frac{w_0}{w}\exp\left(i\phi_0\right) \tag{3.29}$$

If we set on-axis amplitude at the beam waist to be unity, we get complete expression for the fundamental Gaussian beam mode

$$u(r,z) = \frac{w_0}{w}\exp\left(\frac{-r^2}{w^2} - \frac{i\pi r^2}{\lambda R} + i\phi_0\right). \tag{3.30}$$

To express the term for electric field distribution we use equation 3.2 and after a convenient normalization ($\int_0^\infty |E|^2 \cdot 2\pi r\mathrm{d}r = 1$) we gain

$$E(r,z) = \left(\frac{2}{\pi w^2}\right)\exp\left(\frac{-r^2}{w^2} - ikz - \frac{i\pi r^2}{\lambda R} + i\phi_0\right), \tag{3.31}$$

where the expressions for w, R and ϕ_0 derived in previous text.

Electric field distribution $E(r,z)$ along the axis z is shown in figures 3.2 and 3.3. In the figure 3.2 we can see the transverse spreading of a propagating Gaussian beam. Notice the drop of on-axis amplitude of the field and its behaviour as it travels through the distance. In figure the 3.3 we can see the expansion of the radius of curvature.

3.1.3. Confocal Distance

The confocal distance z_c (expressed by equation 3.26), sometimes also referred as Rayleigh range, divides the propagating beam into "near field", defined by $z \ll z_c$ and "far field", defined by $z \gg z_c$. If we rewrite main definitions of Gaussian beam – R described by equation 3.24, w by equation 3.25 and ϕ_0 by $\operatorname{tg}\phi_0 = \dfrac{\lambda z}{\pi w_0^2}$ – with the use of confocal parameter z_c, we obtain following expressions

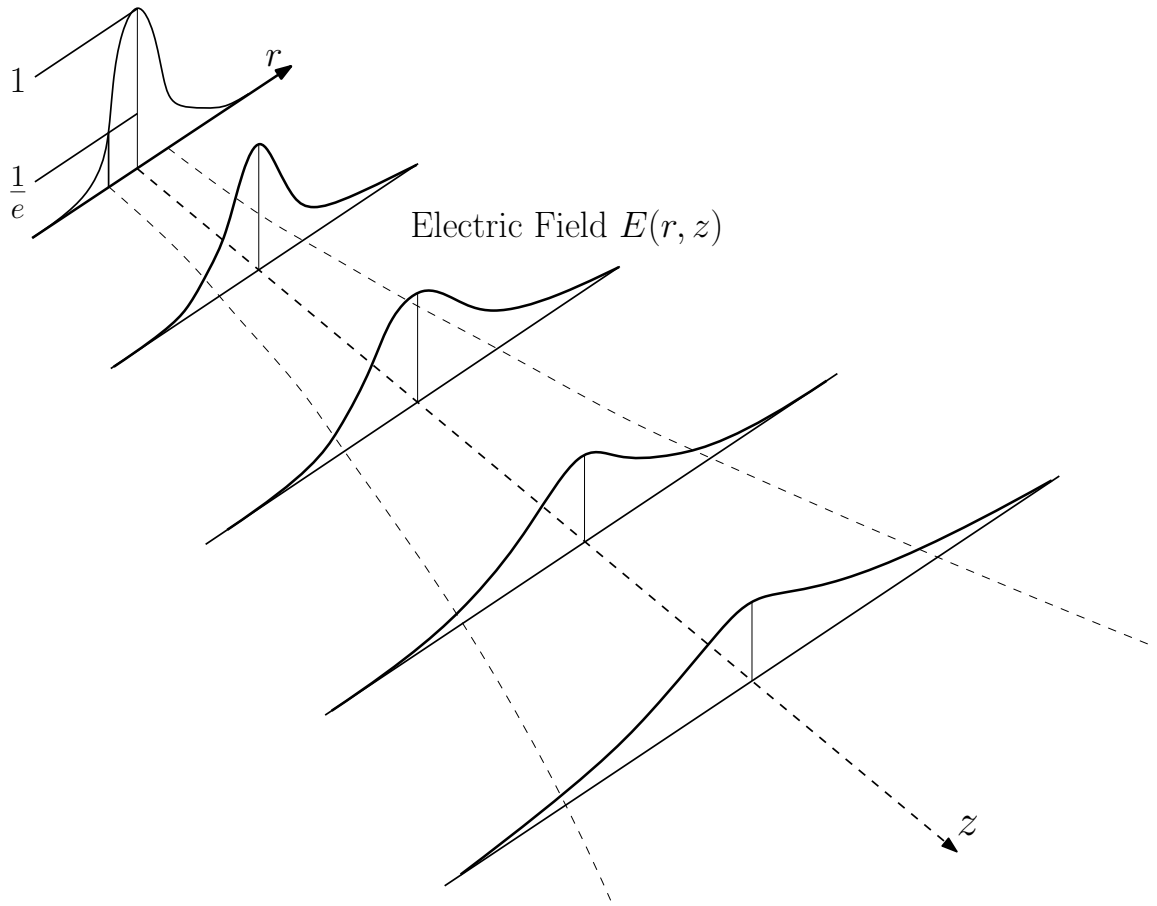

Figure 3.2: Gaussian beam propagation scheme along the axis z. As distance is larger the radius of curvature, defined by the value of $1/e$ of the on-axis intensity, is getting bigger. On the other hand the amplitude peak is being decreased.

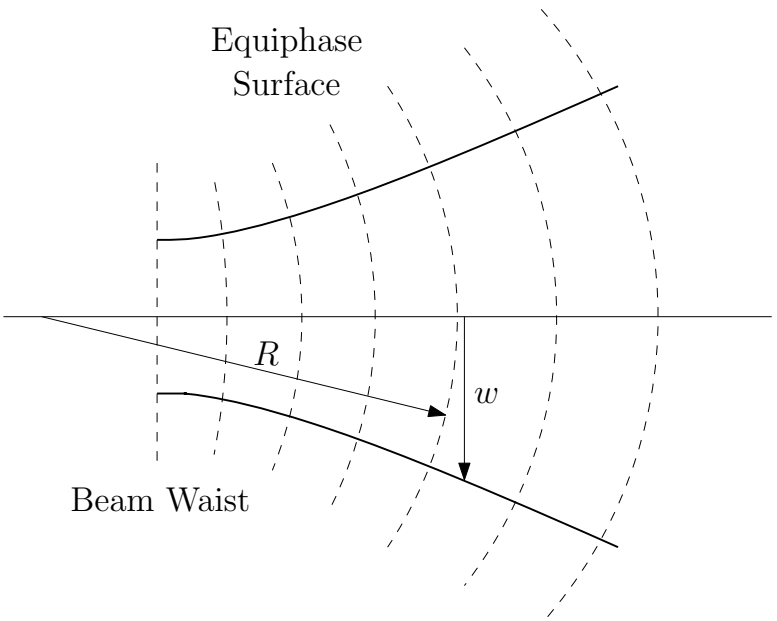

Figure 3.3: Cut though a beam with equiphase surfaces (dashed lines), beam radius w and radius of curvature R.

$$R = z + \frac{z_c^2}{z}, \tag{3.32}$$

$$w = w_0\sqrt{1 + \left(\frac{z}{z_c}\right)^2}, \tag{3.33}$$

$$\phi_0 = \operatorname{arctg}\frac{z}{z_c}. \tag{3.34}$$

In the "near field", the beam radius is almost unchanged from its value at the beam waist, meaning $w \leq \sqrt{2}w_0$. By the time we reach the confocal distance z_c, the beam waist is broadened to the value $w = \sqrt{2}w_0$, thus we can say that the confocal distance defines the distance, where there are almost no changes in the beam radius – beam can be approximated as collimated. At distances greater then z_c from the waist the beam radius increases significantly. As we reach much greater distances than z_c in the "far field" mode, the beam radius grows linearly with distance. The constant growth can be defined by angle $\theta = \operatorname{arctg}(w/z)$ and in the far field limit we obtain the asymptotic beam growth angle θ_0 expressed by

$$\theta_0 = \operatorname{arctg}\left(\frac{\lambda}{\pi w_0}\right). \tag{3.35}$$

If we use small angle approximation the divergence angle θ_0 of Gaussian beam can be rewritten to the form

$$\theta_0 \cong \frac{\lambda}{\pi w_0}. \tag{3.36}$$

For example, if we use wavelength $\lambda = 3\,\text{mm}$, which is relevant for the next chapter, and beam waist radius $w_0 = 3{,}164\,\text{mm}$ then the confocal distance $\approx 10{,}5\,\text{mm}$ and divergence angle $\theta_0 \approx 0{,}3\,\text{rad} \approx 17°$.

3.2. Gaussian Beam Transformation

Formulas expressed in previous sections allow us to calculate the electric field as a function of distance from the waist, however, if we deal with distances much greater than confocal distance z_c the growth of beam size is immense. In order to bring the radiation to the sample in greater distances we have to avoid the constant growth of Gaussian beam. This is carried out by employing lenses or mirrors which can change the radius of curvature and produce converging beam.

In following text, basic formulas for Gaussian beam imaging are developed using the fundamental Gaussian beam mode. Calculations of beam propagation through series of lenses is usually carried out using matrices.

3.2.1. Ray Matrices

The location h' and slope α' of ray at the output plane of system in paraxial approximation is defined to be linear function of the input parameters h and α of ray described by

$$\begin{aligned} h' &= A \cdot h + B \cdot \alpha, \\ \alpha' &= C \cdot h + D \cdot \alpha, \end{aligned} \tag{3.37}$$

where under the term "system" we can imagine anything from simple interface to a multielement optical system. The convention in question is shown in the figure 3.4. Previous expressions can be treated in the form of matrices as

$$\begin{pmatrix} h' \\ \alpha' \end{pmatrix} = \begin{pmatrix} A & B \\ C & D \end{pmatrix} \begin{pmatrix} h \\ \alpha \end{pmatrix} \tag{3.38}$$

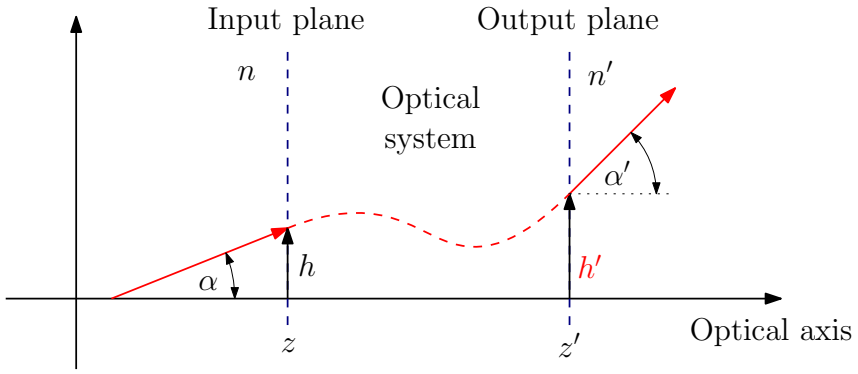

Figure 3.4: Scheme of the convention used in defined expressions.

Since the input radius od curvature is defined by $R = h/\alpha$, we can extract from previous expressions relationship analogically for output

$$R' = \frac{A \cdot R + B}{C \cdot R + D} \tag{3.39}$$

The extension of this ray transformation approach to Gaussian beams leads to the "$ABCD$" law in which four parameters characterize an element of optical system. Important note is that we use the convention where rays are incident from the left.

Basically we can get the matrix representing the effect of large multielement system by multiplying the respective individual $ABCD$ matrices.

Here we show some examples of the ray transformation matrices for

- distance d in material of index of refraction n_2 embedded in material of index n_1;

$$\begin{bmatrix} 1 & \dfrac{n_1 d}{n_2} \\ 0 & 1 \end{bmatrix} \tag{3.40}$$

- thin lens of focal length f;

$$\begin{bmatrix} 1 & 0 \\ -\dfrac{1}{f'} & 1 \end{bmatrix} \tag{3.41}$$

- thick lens with optical powers of both curved surfaces Φ_1 and Φ_2, thickness d and index of refraction described in the direction of beam propagation n_1, n_1', n_2 and n_2';

$$\begin{bmatrix} 1 - d\dfrac{\Phi_1}{n_1'} & d\dfrac{n_1}{n_1'} \\ -\dfrac{\Phi_1}{n_2'} - \dfrac{\Phi_2}{n_2'} + \dfrac{d\Phi_1\Phi_2}{n_1' n_2'} & -d\dfrac{n_1\Phi_2}{n_1' n_2'} + \dfrac{n_1}{n_2'} \end{bmatrix} \tag{3.42}$$

- pair of thin lenses f_1 and then f_2, separated by sum of their focal lengths

$$\begin{bmatrix} \frac{-f_2}{f_1} & f_1 + f_2 \\ 0 & \frac{-f_1}{f_2} \end{bmatrix}. \tag{3.43}$$

4. Development of ODMR Setup

After two chapters of necessary theoretical introduction, this chapter begins the practical part of the thesis. Here we introduce the development of new ODMR spectrometer build around *10T Oxford Instruments* cryostat (*Spectromag SM4000*). It is a modification of MCD spectrometer to which we add a new electromagnetic sample irradiation in microwave (in the following text sometimes referred also as THz) frequency range.

The advantage of this coupled system is its significantly higher sensitivity of measurement (about 8 or 9 orders) than conventional ESR spectrometers [2, 3], which is an outcome of detection of radiation in visible range of electromagnetic spectrum which is much more sensitive than in microwave region. In specific systems it is possible to even detect magnetic resonance of individual molecules [3]. Also, with the possibility of detecting signals from 10^{10} Hz to 10^{15} Hz there is an enormous gain in signal strength which makes the study of very small numbers of defects possible [6–8].

As it was stated before, ODMR is an powerful technique for investigation of various potential advanced materials that could, one day, lead to realization of spintronic devices, quantum computers or ultra high density data storage systems.

The layout of introduced ODMR setup is depicted by the figure 4.1. This solution is connected with the challenge of focusing two beams from different regions of electromagnetic spectrum – visible (VIS) and microwave (THz). This problem was partially solved by the necessary condition that the source of microwaves – Backward-Wave Oscillator (BWO) – needs to be in a "safe distance" from the stray field of the cryostat. This "safe distance" was set to be at minimum 1,1 m which corresponds to the field of 50 G $\approx$ 0,005 T).

BWO is na electron accelerator of small sizes which in general generates a continuous electromagnetic wave in frequency interval ranging from 30 GHz up to 1,1 THz. The specific BWO we are using is able to generate microwave range from 90 GHz to 160 GHz using standard feed horn antenna. Together with the use of frequency multipliers it can cover much larger span up to 480 GHz.

The BWO is placed on a separate optical table, together with focusing elements – Teflon biconvex lenses. Positions and focal length of lenses were chosen to be present exclusively on this separate optical table because of the opacity of Teflon in visible spectrum range. The exact positions and calculations of beam guiding system is in section 4.3. Three different approaches using three various programs were chosen to confirm the correct lenses dislocation. At first, *ZEMAX OpticStudio* program was used. Next approach was done by versatile computing environment *MATLAB*. Results from these two programs were confirmed by *Thomas Keating Ltd* company specializing in design and construction of quasi-optical systems.

In order to couple two different radiation types, dichroic mirror transparent for VIS and reflective for microwaves is used. A 1,1 mm thick high quality rounded glass substrate is sputter-coated with Indium Tin Oxide composition (ITO) thin film of thickness varying

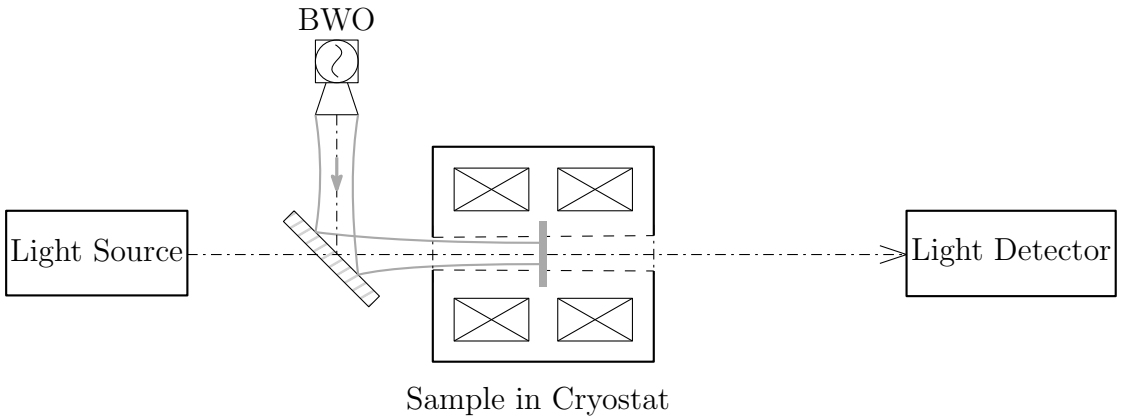

Figure 4.1: Scheme of newly developed ODMR spectrometer by implementing microwave irradiation of the sample, which is placed into standard MCD spectrometer consisting of light source, cryostat and detector positioned in one axis together with optical lenses focusing light beam onto a sample placed in cryostat and then collecting and focusing the beam again on the detector. Microwave radiation is being generated in Backward-Wave Oscillator (BWO), guided and focused by Teflon lenses placed on separate optical table and then reflected by dichroic mirror onto the sample.

from $100 - 310\,\mathrm{nm}$ dependent on the type of coating which is connected to the transmittance/reflectance of incident radiation [69]. The types and characteristics of different coatings are discussed in section 4.1.

As we have discussed in chapter 3 one of the main input parameters into quasi-optical beam guide calculation is the beam waist w_0. However, this parameter is formed by the feed horn antenna, which in our case was not the original one that should have been attached to this specific type of BWO. There was a need of calculation of the distribution of oscillating electromagnetic field generated inside of the horn antenna, which is described in section 4.2.

4.1. Dichroic Mirror VIS/THz

Here we discuss the dichroic mirrors, which are used to couple the two incident beams – microwaves and visible light. Mirrors were acquired from company *Präzisions Glas & Optik GmbH*. High quality glass substrates are coated by sputtering of ITO, which, thanks to its conductivity and transmissivity in thin layers, makes it perfect candidate for many applications. The transmissivity/reflectance characteristics in VIS/microwave regimes respectively are tuned by the thickness of ITO layer. Complete product details can be found on the website [69].

For our purposes we have chosen to order three types of coatings CEC005S, CEC010S and CEC020S. Their characteristics are shown in the table 4.1 and the transmission curves for each type of coating in VIS spectrum range are shown in figures 4.2, 4.3 and 4.4. In the figure 4.5 there are also shown reflection curves for radiation of lower frequencies region of electromagnetic spectrum. Here, different coatings are represented by various colours - CEC005S black, CEC010S red and CEC020S blue. We predict that the behaviour of reflectance will remain alike and will continue in a way, similar as before, also for larger values of wavelength λ as it was confirmed by the experimental assembly.

For the purpose of using ITO glass substrates as mirrors we have ordered them as rounded plates with diameter of 4″ in order to fit them into 4″ mirror mount – *KS4 – ⌀4″ Precision Kinematic Mirror Mount, 2 Adjusters* purchased from *Thorlabs*. This mount is optimal for easy and precise manipulation and fine adjustment of the reflection angle which is crucial for desired sample irradiation. Complete product details can be found on the website [70].

Table 4.1: Different types of ITO coated glass substrates. Thickness of ITO layer influence the transmissivity/reflectance characteristics of VIS/THz regime respectively. For transmissivity of VIS, value at 550 nm is used. For reflectance the average value from the interval of 100 to 215 nm was used.

Type	Layer thickness [nm]	VIS Transmissivity	THz Reflectance
CEC005S	310	85,03%	94,2%
CEC010S	180	82,76%	92,1%
CEC020S	100	84,23%	85,9%

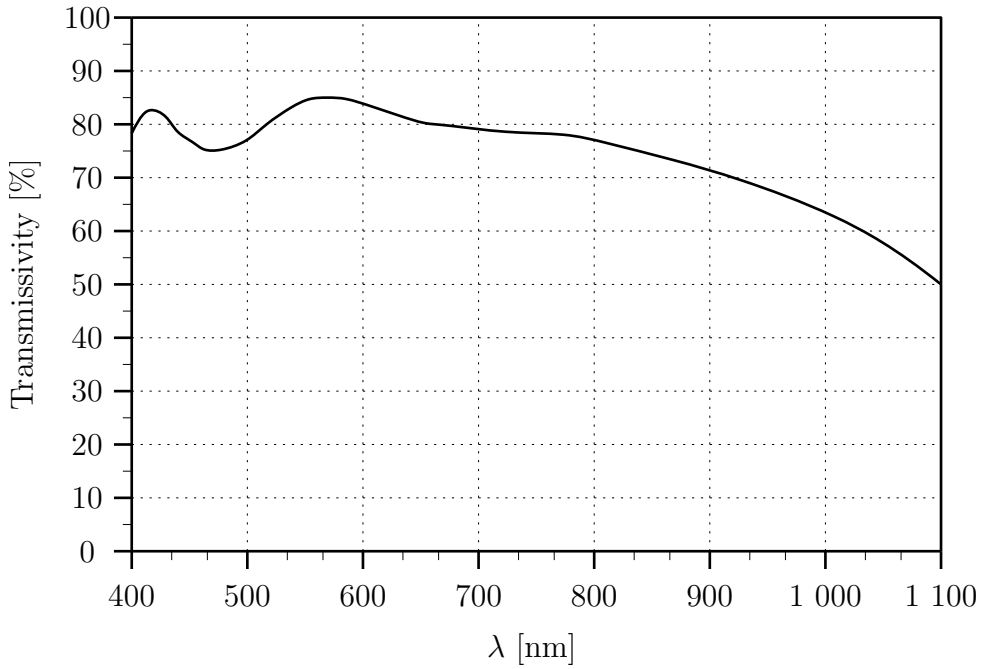

Figure 4.2: Transmission curve in the visible spectrum range of ITO coated glass substrate – type CEC005S with the film thickness of 310 nm.

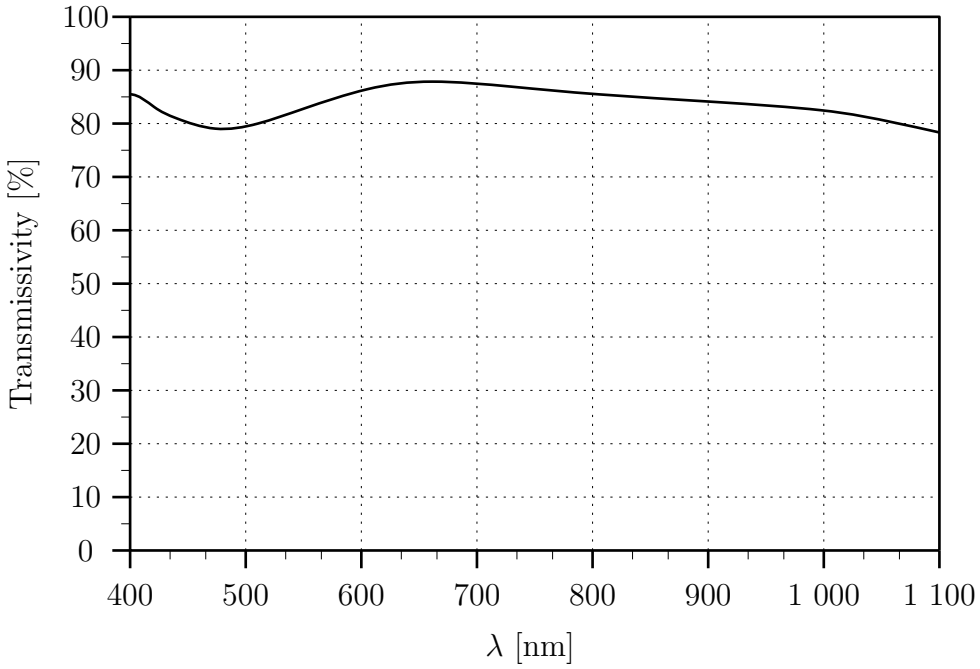

Figure 4.3: Transmission curve in the visible spectrum range of ITO coated glass substrate – type CEC010S with the film thickness of 180 nm.

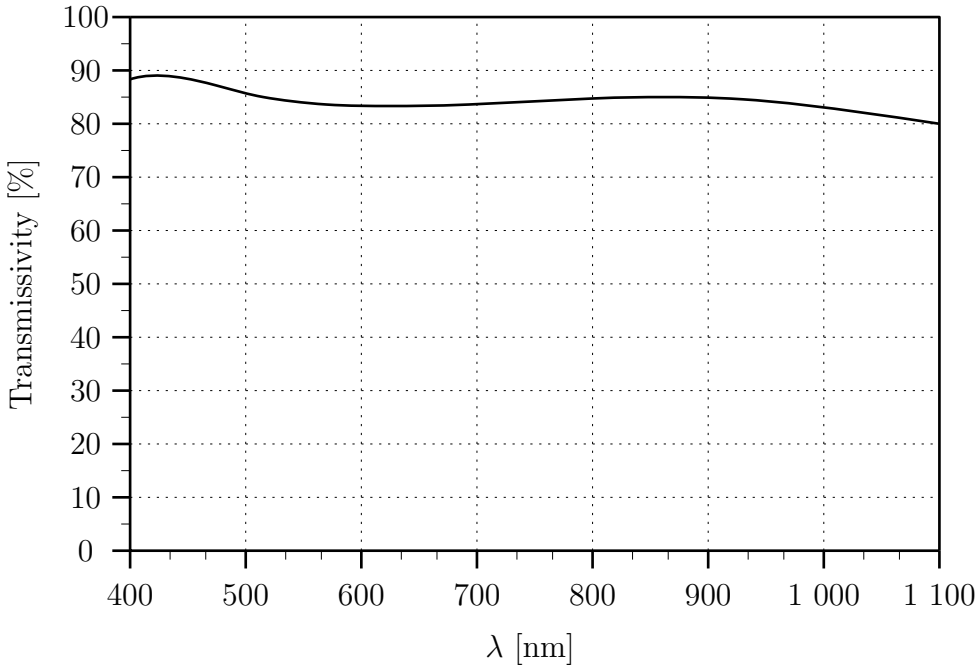

Figure 4.4: Transmission curve in the visible spectrum range of ITO coated glass substrate – type CEC020S with the film thickness of 100 nm.

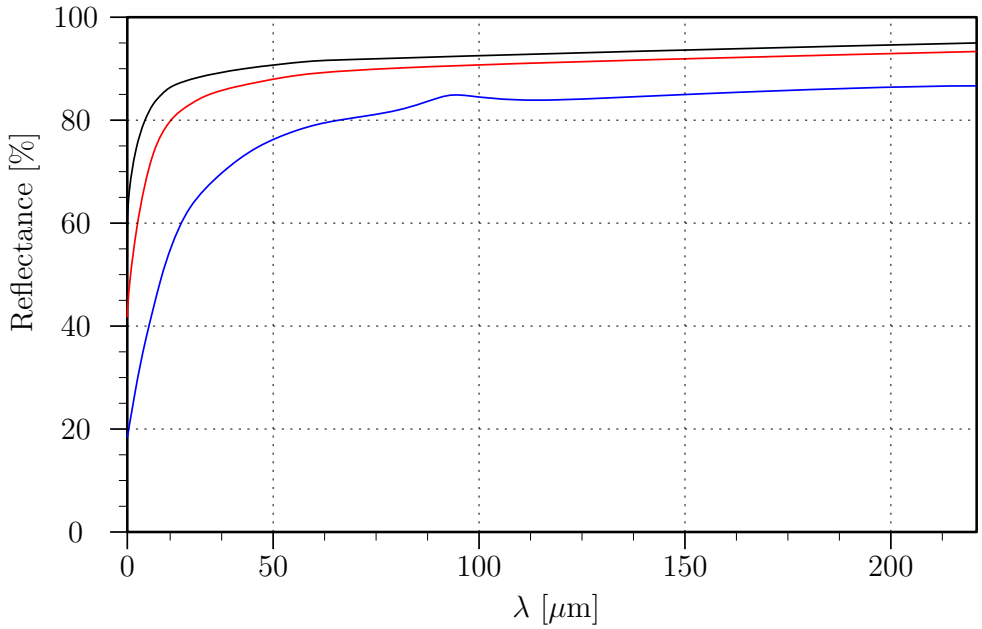

Figure 4.5: Reflection curve for all three types of ITO coated dichroic mirrors differed by colour – CEC005S black, CEC010S red and CEC020S blue.

4.2. Horn Simulation

In the chapter 3 we have defined the most important expressions for calculations of quasi-optical systems, in our case calculation of the beam guiding system. There is also stated that one of the most important input parameters is the waist of guided beam w_0. As it was mentioned before, we possess an unoriginal pyramidal rectangular horn antenna attached to the BWO, resulting in unknown waist w_0 of generated beam.

To solve this task we have used a simulation software – *CST Computer Simulation Technology Studio Suite*, which is a program generally used for computation of electromagnetic designs and its analysis. Detailed information about this program can be found on website [71].

The output waveguide of the BWO (which is input for horn antenna) is classified as WR7 according to the standard EIA dimension [72]. The sketch of simulated horn antenna is shown in the figure 4.6. There are described only inner dimensions of the horn antenna, that are crucial for the simulation process, in order to simplify the sketch. Thickness of the material is 1 mm. The input waveguide port (see the red markings) for the simulation was placed into the centre of inner port with dimensions specified by EIA WR7: $x = 0{,}8255$ mm and $y = 1{,}651$ mm.

The essential result of simulation can be seen in the figure 4.7, where the distribution of the electric field in a cut along the y axis at the output plane of horn antenna is shown. The waist of beam $w_0 = 3{,}162$ mm is given by the value $1/e$ (marked by blue horizontal line) of the on axis relative intensity (marked by red horizontal line) [68].

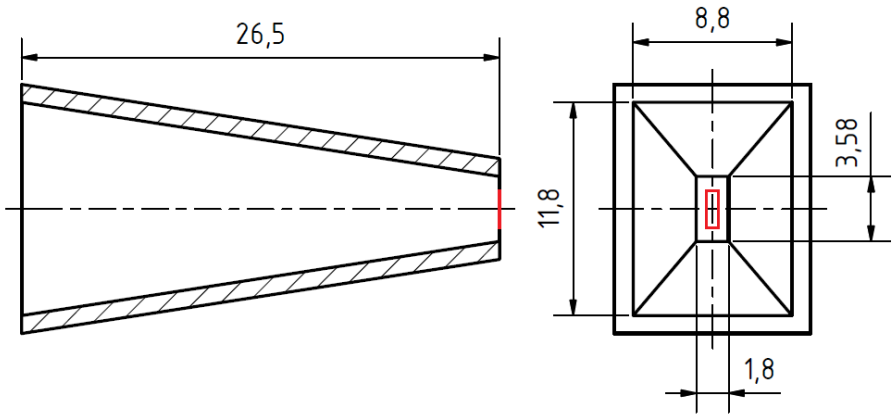

Figure 4.6: Sketch of pyramidal horn antenna simulated in *CST Studio Suite*. Only inner dimensions of the ports are shown to simplify the sketch, thickness of the edges is 1 mm. The input waveguide was placed into the inner port of horn antenna with dimension set by EIA WR7 $x = 0{,}8255$ mm and $y = 1{,}651$ mm, see the red outline.

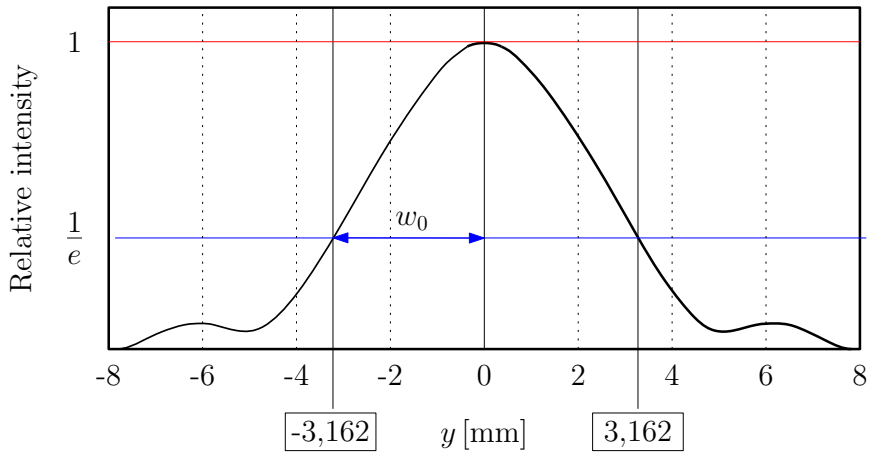

Figure 4.7: Distribution of the electric field simulated by *CST Studio Suite* viewed in cut along y axis at the output plane of horn antenna. The on axis relative intensity of field is marked by red horizontal line and the value $1/e$ of the on axis relative intensity is marked by blue horizontal line. The beam waist radius $w_0 = 3{,}162$ mm is shown by blue double sided arrow.

4.3. QO Beam Guide Optimization

This section is describing process of simulation and optimization of the beam guiding system. The initial conditions are following:

- Input waist parameter of the beam generated by BWO with pyramidal horn antenna is $w_0 = 3{,}162\,\mathrm{mm}$
- Beam will be guided by quasi-optical lenses, which will be placed exclusively on a separate "microwave" optical table
- The dichroic mirror positioned in the intersection of "microwave" and "optical" table will couple both incident beams onto the sample placed in cryostat

Quasi-optical focusing elements used in the beam guiding system are biconvex PTFE (Teflon) lenses with diameter $\varnothing = 40\,\mathrm{mm}$, focal length $f = 120\,\mathrm{mm}$ and index of refraction in frequencies of hundreds of GHz $n \approx 1{,}4$ [73].

The total path of microwave beam is influenced by two main factors: firstly it is the necessity of BWO being in the safe distance from the stray field of cryostat, which was set to be 1,1 m at minimum; secondly there cannot be any Teflon lens in the path of light meaning that microwave beam needs to be focused onto the sample in cryostat before the coupling of both (microwave and optical) beams.

For the optimization three different approaches were taken in order to verify the results. At first we have calculated positions of lenses with the optical design program *ZEMAX OpticStudio*, after that we have tried to simulate propagation of Gaussian beam with the computing environment *MATLAB*. Results from both programs were then confirmed by calculation acquired from *Thomas Keating Ltd* company specializing in quasi-optical systems design.

4.3.1. ZEMAX OpticStudio

From the name itself, it can be seen that *ZEMAX OpticStudio* is a program for optical design and analysis. Since *ZEMAX* is calculating corresponding refractive index n of optical elements using (among others) Sellmeier equation, we had to implement a new material into "glass catalogue". The Sellmeier equation is and empirical relationship between refractive index n and wavelength λ given by

$$n^2(\lambda) = A + \frac{B_1\lambda^2}{\lambda^2 - C_1} + \frac{B_2\lambda^2}{\lambda^2 - C_2}, \tag{4.1}$$

where A, $B_{1,2}$ and $C_{1,2}$ are Sellmeier coefficients associated with a given optical material. This equation is usually in different form, in which there is number 1 instead of A. The coefficient A i an approximation of the short-wavelength absorption contributions to the refractive index at longer wavelengths. Sellmeier coefficients for Teflon are shown in table 4.2 [74].

For calculations we have used wavelength $\lambda = 3\,\mathrm{mm}$. The refractive index of Teflon was set to be constant $n = 1{,}433$ and lenses were approximated as thin. Tracing, shown in the figure 4.8, was obtained for two point sources – on axis (blue trace) and 3 mm of axis (green trace) – both with 10° radiation cone angle. Beam is focused by three lenses of focal length $f = 120\,\mathrm{mm}$, then it is reflected by mirror and imagined onto the sample in cryostat with ⌀14 aperture. Exact positions and distances are shown in the scheme.

Table 4.2: Sellmeier coefficients for Teflon [74]

A	B_1	C_1	B_2	C_2
1,517	0,184	0,016	1	104,66

Although the divergence is not shown in the tracing scheme and the resulting sample irradiation is not perfect, this calculation gave us important rough results about the placement of all optical components, which we have used in next steps of beam guide optimization.

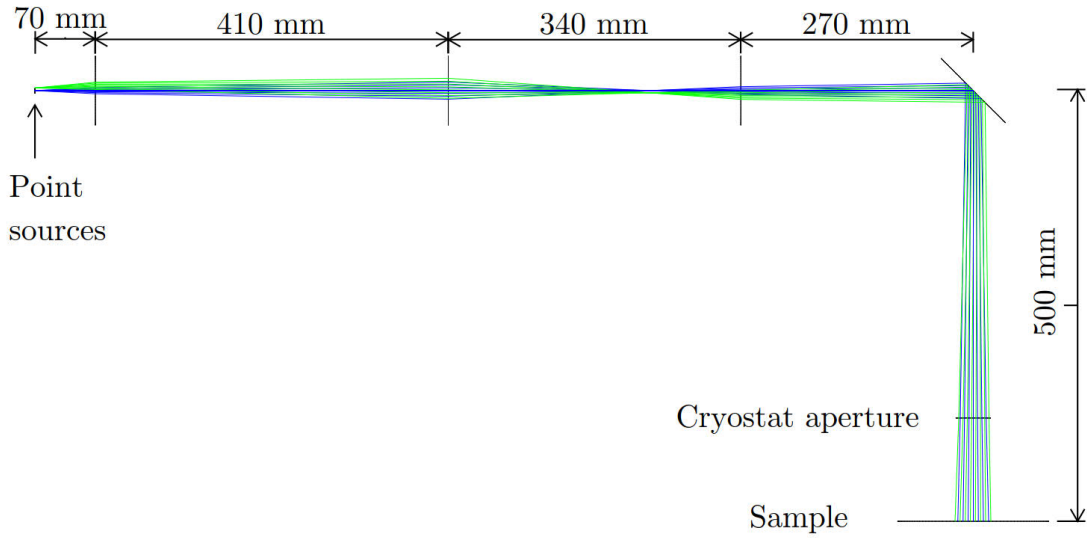

Figure 4.8: Tracing of microwave beam guiding system obtained for two point sources, on axis (blue trace) and 3 mm of axis (green trace), both with 10° radiation cone angle. Beam is focused by three lenses of focal length of $f = 120$ mm, then it is reflected by mirror and imagined onto the sample in cryostat with ⌀14 aperture.

4.3.2. MATLAB

In *MATLAB* computing environment we have used script simulating the behaviour of the radius of Gaussian beam, which means the $1/e$ value of the on axis relative intensity. Expressions for the radius w, object s and image s' waist position and confocal distance z_c, which are all shown in the figure 4.9, were gained from [68] and [75] as

$$w = w_0 \sqrt{1 + \left(\frac{\lambda z}{\pi w_0^2}\right)}, \tag{4.2}$$

$$s' = f\left[1 + \frac{\left(\frac{s}{f} - 1\right)}{\left(\frac{s}{f} - 1\right)^2 + \left(\frac{z_R}{f}\right)^2}\right], \tag{4.3}$$

$$z_c = \frac{\pi w_0^2}{\lambda}. \tag{4.4}$$

The result of *MATLAB* script calculation can be seen in the figure 4.10, where the red solid line represents the propagation of Gaussian beam radius along the axis z. Blue dotted lines are representations of lenses placements, blue solid line is then the plane of dichroic mirror, but the effect is not pictured. Black solid lining shows the aperture of cryostat. Green dotted line represents the plane where sample is placed into cryostat.

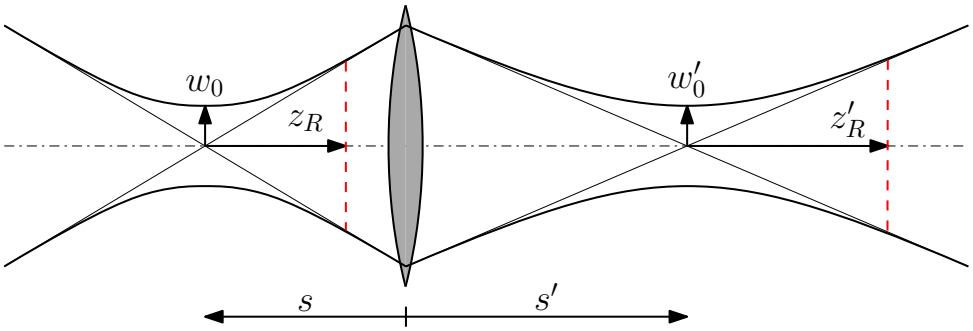

Figure 4.9: Scheme of the Gaussian beam imaging geometry by thin lens with described object/image beam waist radius w_0/w_0', beam waist position s/s' and confocal distance z_R/z_R' respectively.

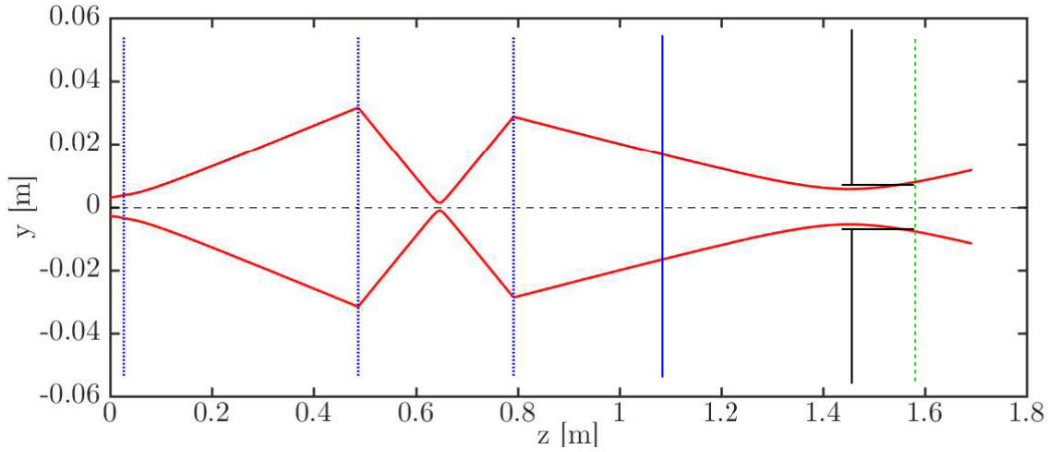

Figure 4.10: Calculation of Gaussian beam propagation in *MATLAB*. The red line represents behaviour of beam radius along the axis of propagation z. Blue dotted lines mark positions of lenses. Blue solid line shows the plane where dichroic mirror is placed but its effect is not pictured. Black solid lining represents the aperture of cryostat windows and green dotted line shows plane of sample.

4.3.3. Thomas Keating Ltd.

The outcome of previous section was then verified by Dr. Kevin Pike from *Thomas Keating Ltd* company. The acquired result is placed into Appendices section A.2 because of its form of delivery as a large scale drawing scheme. Here in the figure 4.11 can be seen only a redrawn scheme of the result. Red dotted lines show the positions of beam waists, where the first is inside the pyramidal horn antenna and the last is in the proximity of sample placed inside of cryostat. Blue dotted lines represent the placements of lenses or dichroic

mirror. Black solid lining marks the inner aperture of cryostat. Values represented by ϕ are diameters of the beam in relevant positions in mm.

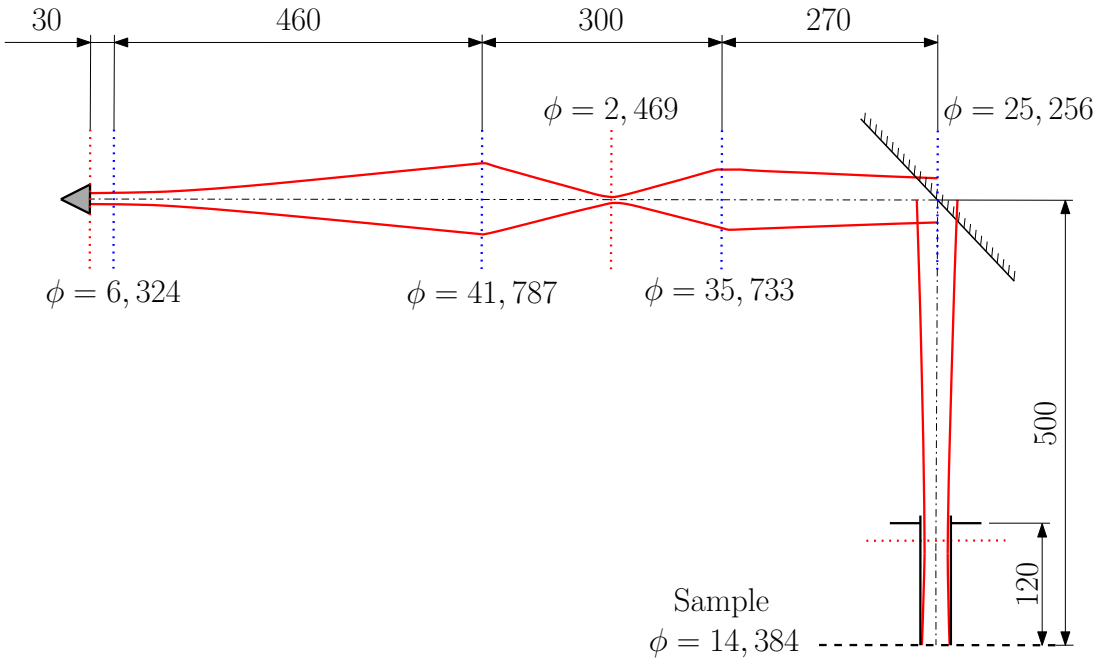

Figure 4.11: Redrawn scheme of the calculation by *Thomas Keating Ltd* company. Red dotted lines marks the positions of beam waist (first is inside the pyramidal horn antenna – source). Blue dotted lines show places of lenses or plane of dichroic mirror. The values ϕ represents the diameter of propagated beam in specified positions in mm. Black solid lining marks the aperture of cryostat window. As can be seen, this result is in a good agreement with the outcome of *MATLAB* script.

4.4. Antenna for Nitrogen-Vacancy Centres Detection

If one needs to excite paramagnetic resonance of electron with lower frequencies a different approach for bringing the microwave radiation onto the sample is needed. The divergence of electromagnetic beam with frequencies in units of GHz is immense and the form of beam guidance through the system of lenses is almost impossible. Here we introduce simulation of broadband microwave planar ring antenna for ODMR of Nitrogen-Vacancy (NV) centres in diamond. Design of the antenna was influenced by the article [76] however, a few adjustments had to be carried out.

Simulation process was done in *CST Studio* software program. The targets of antenna design are as follows:

- Antenna is placed beneath the sample.
- It generates spatially uniform magnetic field B within the largest possible area of the sample.
- The resonance frequency of generated oscillating field is around 2,87 GHz with bandwidth of hundreds of MHz.

4.4.1. First Antenna Design

One of the most important characteristic of antenna design is the reflection coefficient S_{11} where, if the conditions are fulfilled, the most of energy delivered to the antenna is being radiated. However, also the uniformity of magnetic field is crucial for obvious reasons.

The geometry of antenna can be seen in figure 4.12 viewed from the top. There is a grounding plate covering the whole opposite side of antenna. For connection of the input signal ultra small coaxial connectors were used (the area for connector soldering is placed on the left side of antenna in figure 4.12).

The characteristics of generated oscillating magnetic field can be seen in the figure 4.13: Simulated reflection coefficient S_{11} in (a) and uniformity of generated magnetic field in (b).

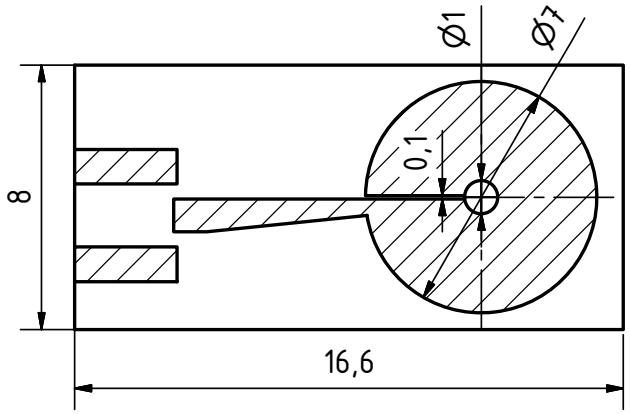

Figure 4.12: Scheme of antenna geometry. The hatched sections represent the conductive area. Sample will be placed into the centre of rounded conductive part where the antenna is radiating spatially uniform excitation field. The conductive part in the left side of the picture is for connector soldering. The opposite side of antenna (bottom) is whole covered by conducting material and acting as grounding.

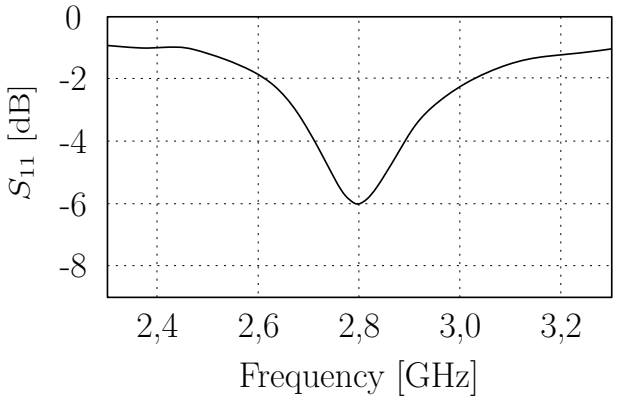

(a) Simulated reflection coefficient S_{11} of designed antenna. The dip is clearly observable near $f = 2{,}8\,\mathrm{GHz}$. The bandwidth is approximately 400 MHz (Q-factor ≈7)

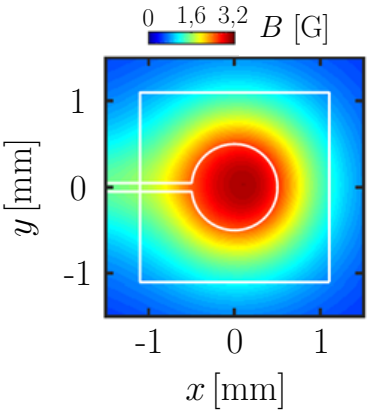

(b) Spatial uniformity of generated oscillating magnetic field B.

Figure 4.13: Reflection coefficient S_{11} in (a) and spatial uniformity of generated magnetic field B within the sample surface in (b). *Modified pictures originally from [76]*

For the fabrication of antennas positive lift-off optical lithography process was used in *CEITEC* laboratories. As a substrate 4′ Si wafers were used.

However, we have encountered problem with the soldering of connectors. These problems caused heavy damage to the antenna and its characteristics. After multiple re-soldering and temperature tests the conductive part of antennas tended to detach from the substrate surface.

In the figure 4.14 measurement of the reflection coefficient after the first soldering onto the antenna (black line) and after multiple temperature tests and re-soldering of the connector is shown. Clearly, it can be seen that the damage is immense and the antennas cannot be used in order to prevent the destruction of signal source.

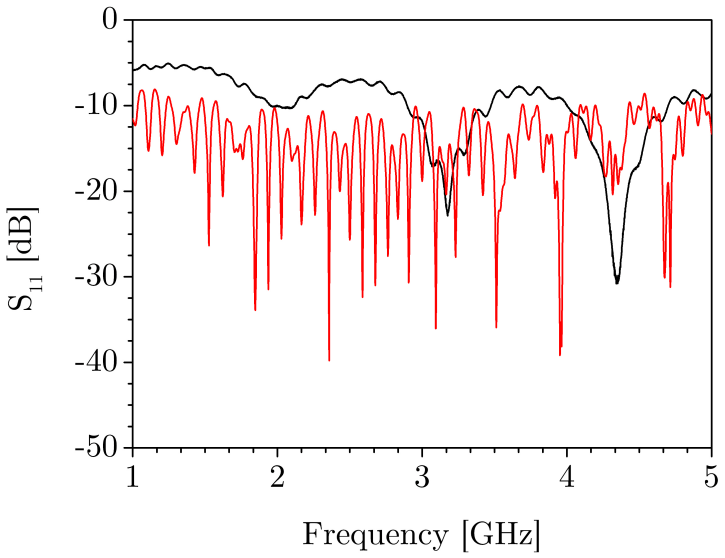

Figure 4.14: Measured data of reflection coefficient S_{11} of antenna after the first soldering of connector – black line, and after multiple temperature tests and repeated soldering – red line.

4.4.2. Second Antenna Design

The result of previous section led us to change of the fabrication process. We have decided to fabricate another type of antennas on small automated milling cutter. However, the minimal dimension which is possible for the cutter to mill is 0,2 mm. That had a strong influence on the relevant parameters of antenna resulting in following changes of its design.

The adjustments of antenna dimensions can be seen in the figure 4.15. Change in the dimension of gap of the antenna loop had a large influence on the resonant frequency. In order to set the frequency back to 2,87 GHz we needed to radically increase the diameter and shift the inner hole out from the axis of the main antenna loop. In the figure 4.16 also simulation of the reflection coefficient S_{11} can be seen. The change of relevant dimensions is shown in following table 4.3.

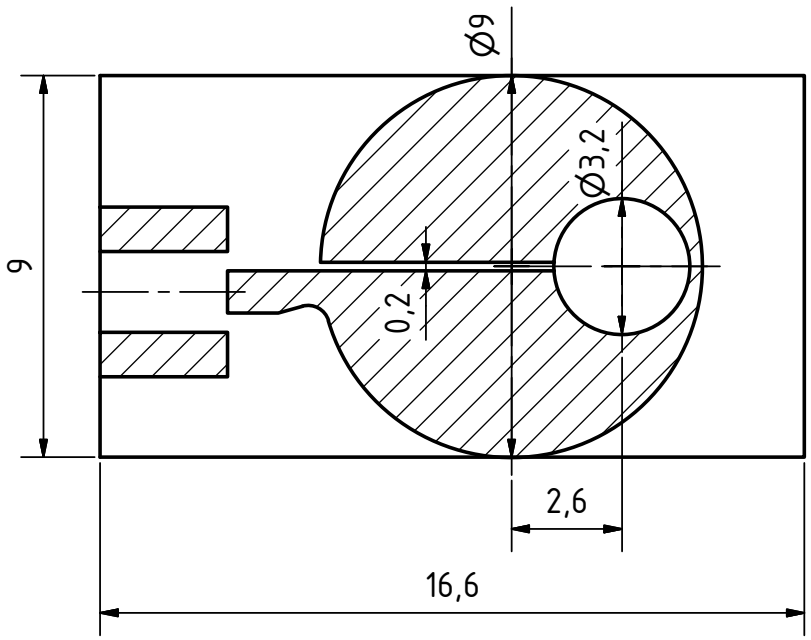

Figure 4.15: Scheme of the second generation of NV centres antenna suitable for fabrication on milling cutter. Conductive material of antenna is represented by hatched area. In order to set the resonant frequency back to 2,87 GHz we had to radically increase the diameter of inner hole and shift it from the axis of the main antenna loop by 2,6 mm.

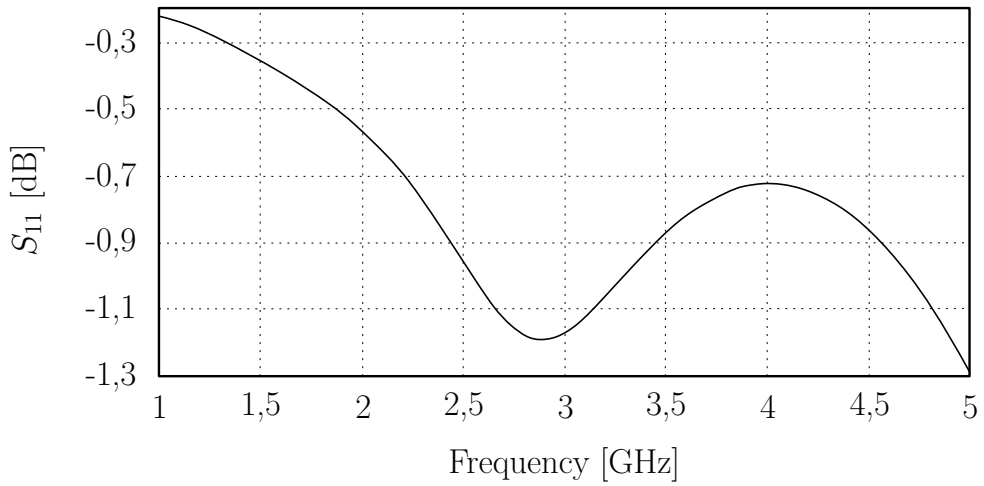

Figure 4.16: Simulation of the reflection coefficient S_{11} of the second generation of antenna. The dip of S_{11} is clearly observable near $f = 2{,}8$GHz.

Table 4.3: Comparison between the two discussed designs of NV centres antenna.

Dimensions in mm	First generation	Second generation
g	0,1	0,2
s	0,0	2,6
R	4,0	4,5
r	0,5	1,7

4.5. Sample Holder

During the development of new ODMR spectrometer, sample holder allowing an exposure to both types of electromagnetic radiation was designed and manufactured. The presented sample holder is also suitable for the study of NV centres samples.

4.5.1. NV Centres Sample Holder

Design of discussed sample holder for NV centres in diamond is shown in figures 4.17 and 4.18, where the drawing scheme of the whole assembly and rendered images from *Autodesk Inventor* software application are shown respectively.

Samples of NV centres in diamond are placed right onto the antenna (postion 2 in figure 4.17), which was described in previous sections. Antenna is fixed by the covering brass plate (positon 5) pressed by four bolts (position 6) in each of its corners to the brass base of sample holder (postion 1). To prevent conductive connection of the grounding of antenna and base, Teflon spacer (position 3) is inserted in between. The signal to the antenna is brought by ultra small *U.FL* connector (position 4) soldered directly to the antenna. Optical axis of the spectrometer is marked by dashed dotted line.

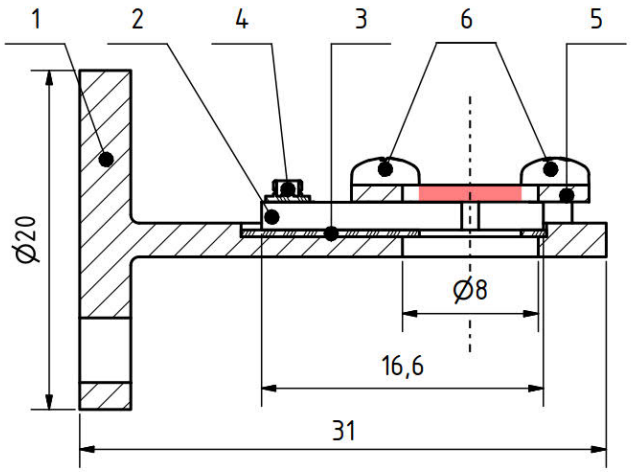

Figure 4.17: Scheme of the sample holder designed for NV centres samples viewed in cut. Area marked by red square marks the space for sample placement right above the antenna (position 2). Both sample on top of antenna is fixed be brass plate (position 5) by four bolts (position 6) in its each corner by screwing them into the base (position 1) which is then connected to the sample rod of cryostat. To prevent conductive connection between grounding of the antenna and base, Teflon spacer (postion 3) is inserted. In the scheme also the *U.FL* connector (position 4) can be seen. The dashed dotted line represent the optical axis of spectrometer.

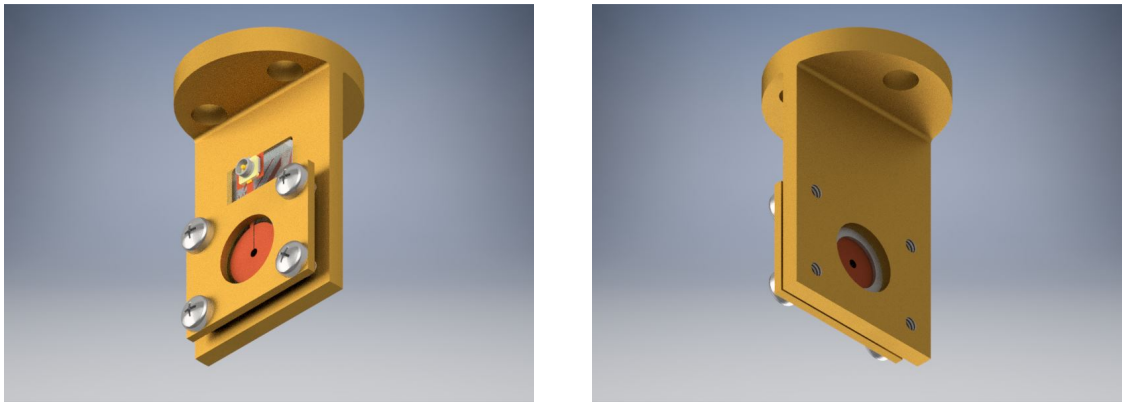

Figure 4.18: Rendered images of NV centres sample holder from top right view on the left and bottom right view on the right right.

4.6. New ODMR Spectrometer

In order to summarize the whole chapter, here we demonstrate the final arrangement of THz section of ODMR spectrometer assembly.

As the source of radiation we use BWO, with its limiting factor, that it needs to be in a "safe distance" from magnetic stray field of cryostat, which was set to be 1,1 m at minimum (which corresponds to the field of 50 G $\approx$ 0,005 T). On the other hand, it provides a continuous, voltage tunable frequencies ranging from 90 to 160q GHz. With the use of frequency multipliers, it is possible to go almost up to 500 GHz. Beam is guided through Teflon lenses of focal length $f = 120$ mm. To couple THz and VIS radiation onto the sample, dichroic mirror is used.

The results of QO beam guide system was then verified experimentally by the intensity detector - Golay cell. As the result of thin lens approximation in every process of calculations, small adjustments in position of lenses had to be done. Exact placement of all components is described in figure 4.19.

Photographies of the ODMR assembly can be seen in figures 4.20 and 4.21.

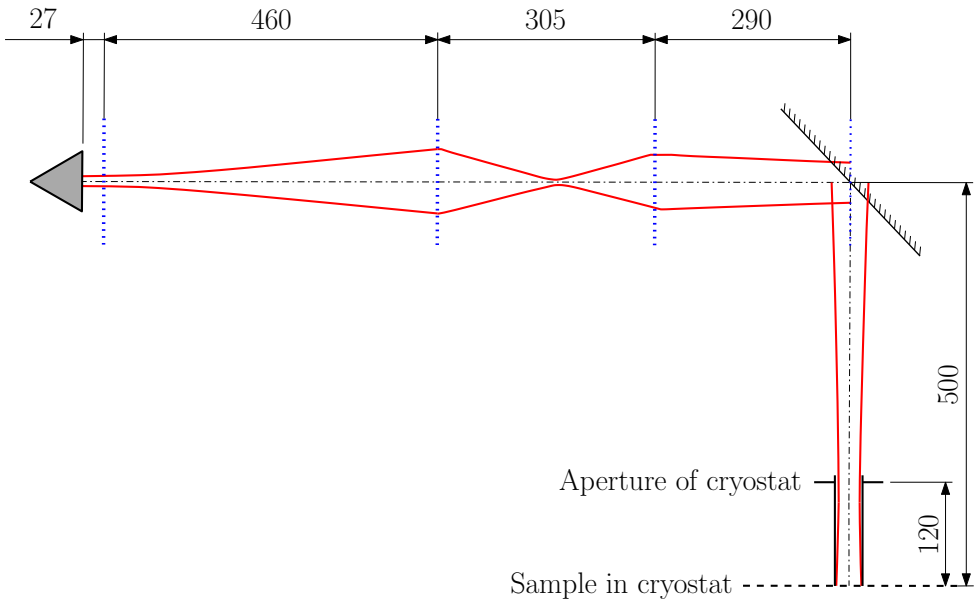

Figure 4.19: Scheme of final THz beam guide section of ODMR assembly. Blue dotted lines represent positions of lenses or plane where dichroic mirror is placed. Black solid lining marks the aperture of cryostat window.

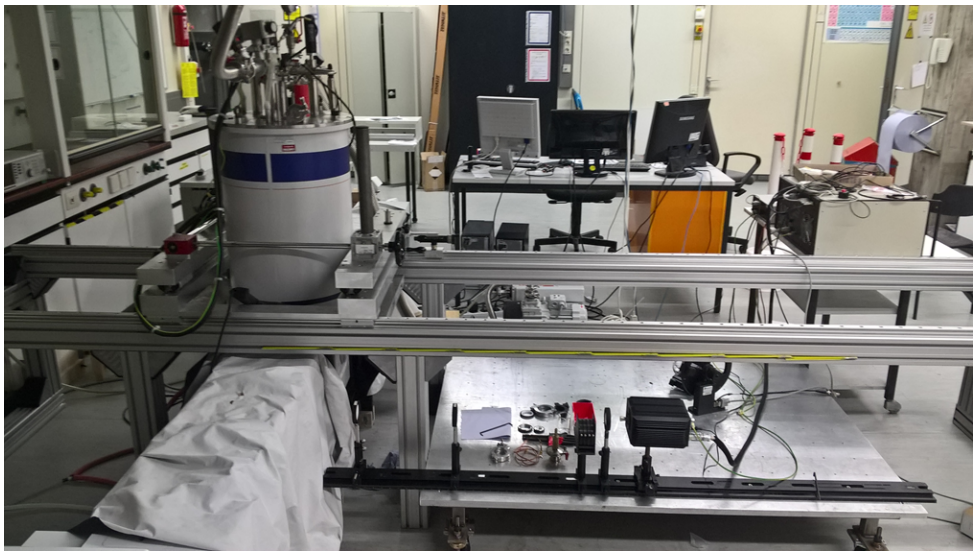

Figure 4.20: Photography of the ODMR assembly from the detector side with closed shading box around optical beam path.

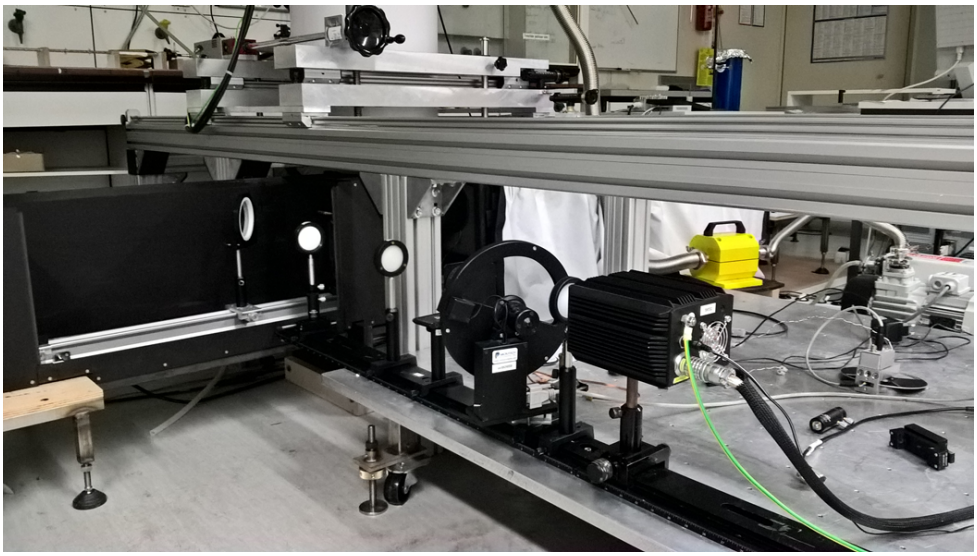

Figure 4.21: Photography of the ODMR assembly with opened shading box of optical path, where the dichroic mirror is visible together with the table for THz optics.

5. Experimental Results

"The most exciting phrase to hear in science, the one that heralds new discoveries, is not 'Eureka!' (I found it!) but 'That's funny ...'"

Isaac Asimov

The capabilities of newly developed ODMR spectrometer were then attempted to reveal on multiple samples. The process of measurements that were performed is following. At first, standard MCD spectrum was recorded at two fixed values of magnetic field while sweeping with the wavelength of incident light at low temperature. After analysing which of the MCD signals is most affected by a change of magnetic field, we set the wavelength to that relevant point and started to irradiate the sample with microwaves at fixed frequency f_R, which was set on the specific value in order to hit the paramagnetic resonance. Then we started to record intensity measurement in VIS spectrum while slowly sweeping with the magnetic field around the value $B = B_R \pm 0{,}5\,\mathrm{T}$ for which the microwave resonant frequency was set.

Since the condition for EPR to occur is given by equation 2.12, we need the specific value for Landé $g-$factor for each sample. Since we have used heavily studied molecules, the $g-$factors were obtained from relevant papers.

5.1. Chromium Complex $[Cr(ddpd)_2](BF_4)_3$

The complex $[Cr(ddpd)_2](BF_4)_3$ is highly water-soluble and very stable towards thermal and photo-induced substitution reactions and in the future, it can be used for fluorescence intensity- and lifetime-based oxygen sensing in the near-infrared (NIR) spectrum [77].

We have tested three different forms of the sample: single crystal, powder and solution. The measurement data are shown for each form together with a picture of the sample.

The single crystal sample was moulded into $\varnothing 12\,\mathrm{mm}$ circular cast of acrylic glass, as can be seen on the left side of figure 5.1. The powder sample was mixed with Fluorolube grease, which is a common technique for stabilization of powder-like samples for spectroscopy measurements. The sample in form of solution was diluted in distilled water mixed with glycerine.

For each sample, after the MCD measurement at the temperature of $1{,}5\,\mathrm{K}$, relevant MCD peaks were chosen in further experiments. Then, specific frequency of microwave irradiation f_R was chosen in order to hit the resonance and the intensity measurement was started while sweeping the magnetic field around the resonance field $B = B_R \pm 0{,}5\,\mathrm{T}$. The specific experimental set of values of ODMR measurement for each form of the Chromium compound is attached in the following table 5.1.

Since the condition for EPR is given by equation 2.12, with the value of Landé g-factor $g \approx 1{,}97$ [77] we can calculate appropriate corresponding values of magnetic field B_R, see table 5.1.

However, no unexpected but desired change (ODMR signal) in the intensity measurement was recorded.

Table 5.1: Experimental values of ODMR measurements of Chromium(III) complex $[Cr(ddpd)_2](BF_4)_3$ samples. E corresponds to the value of energy in MCD spectrum, B_R represent the value of magnetic field for which the resonance occurs for given frequency f_R of microwave irradiation.

Form of the sample:	Single crystal	Powder	Solution
E [cm^{-1}]	24 300	20 400	23 700
B_R [T]	5,1	5,4	5,8
f_R [GHz]	141	150	160

If we compare the three MCD spectra for different forms of the sample, we can see that the resemblance is not there as much as one would expect. The problem can be in the extremely low intensity of MCD peaks in case of powder and single crystal samples.

Regarding the single crystal, low illumination of the sample could be caused by some condensed impurity covering the light path, which should intersect the sample plane in the position of the crystal itself, resulting in a shadow casted over the crystal. However, since the experiment was not reproduced, we could not find a simple explanation.

With respect to the powder sample, there could possibly be the problem with the amount of powder and its proper mixture with Fluorolube grease. As can be seen in the figure 5.2 the compound is not properly covering the whole glass even though the amount of powder is approximately the same as in the other powder-like samples. Therefore the diffraction of light passing through the powder could be very high. The next common step would be the production of next sample, however, that was not possible in our case, because of two highly restricting factors: available amount of the sample in storage and time.

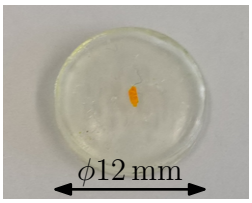

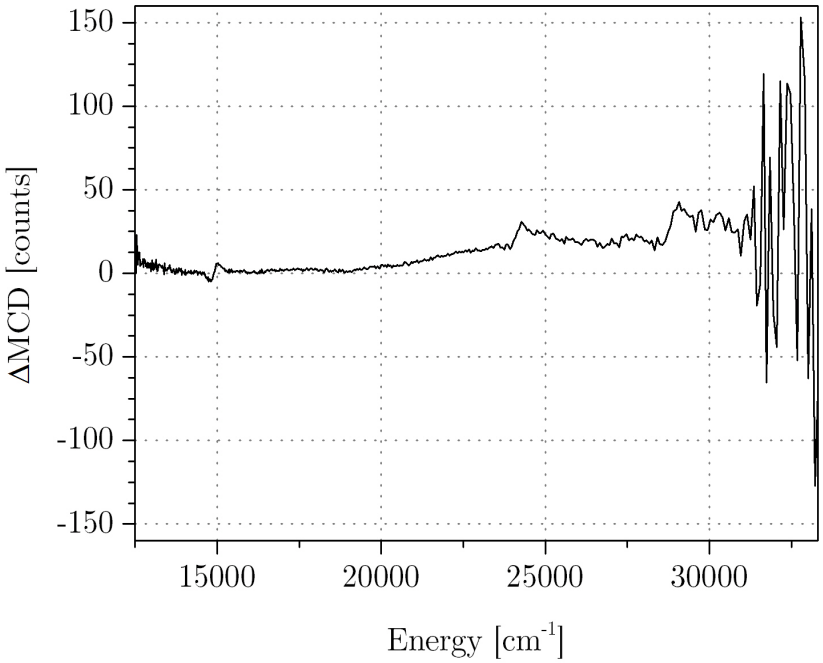

Figure 5.1: ΔMCD measurement of Chromium(III) complex [Cr(ddpd)$_2$](BF$_4$)$_3$ single crystal sample at 6 T and 1,5 K. Due to low illumination the resemblance between MCD spectra for different forms of sample is very weak.

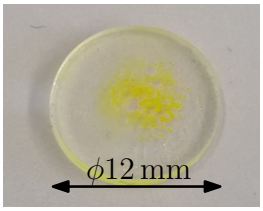

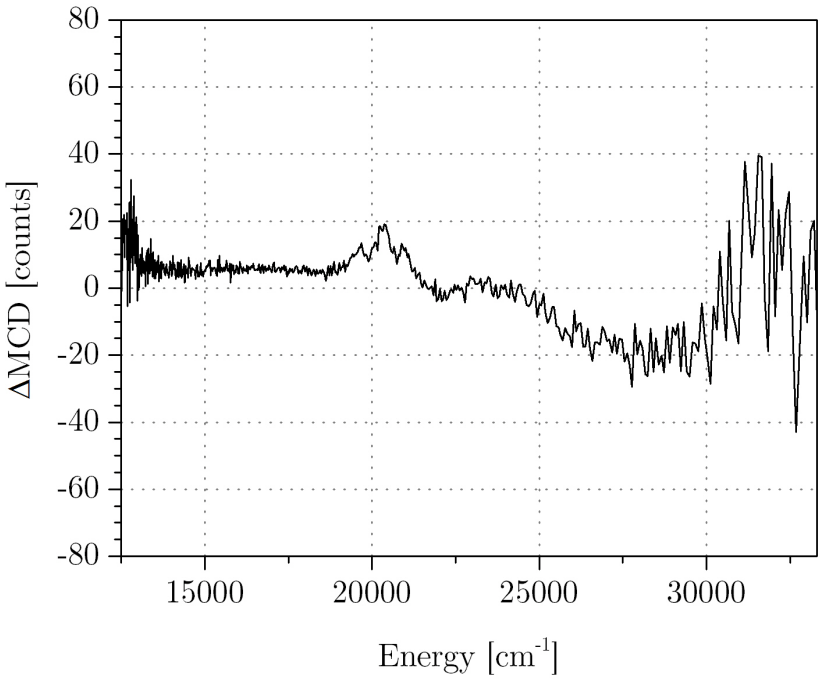

Figure 5.2: ΔMCD measurement of Chromium(III) complex [Cr(ddpd)$_2$](BF$_4$)$_3$ powder sample at 7 T and 1,5 K. Due to low illumination the resemblance between MCD spectra for different forms of sample is very weak.

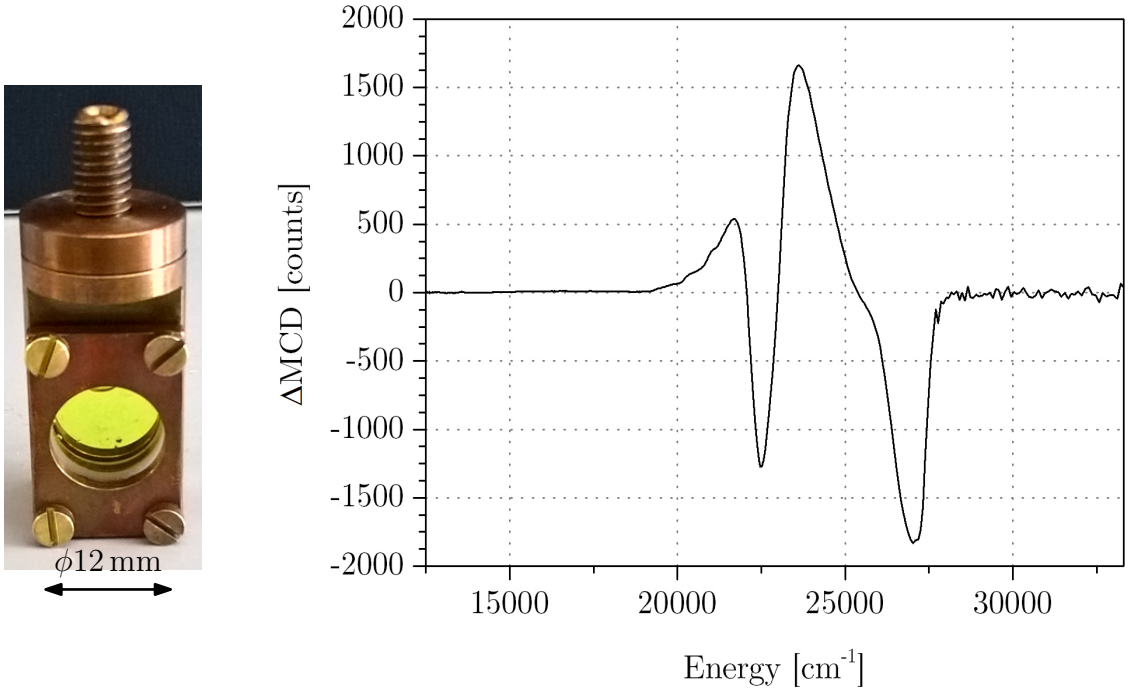

Figure 5.3: ΔMCD measurement of Chromium(III) complex $[Cr(ddpd)_2](BF_4)_3$ sample diluted in distilled water mixed with glycerine at 7 T and 1,5 K.

5.2. $ErPc_2$

The $ErPc_2$ double-decker belongs to the group of lanthanide based metal complexes with which are heavily investigated and have a promising future of many applications in new hybrid materials or as single molecule magnets. [78, 79]

Discussed $ErPc_2$ can be, for example, used as a photosensitive layer in organic field-effect transistors [80].

Studied sample of $ErPc_2$ was in a form of powder, which was mixed with Fluorolube grease. Picture of the sample can be seen on the left side of figure 5.4, where, on the right side also MCD spectrum recorded at 7 T is shown. For ODMR experiment we have chosen to try multiple MCD peaks for different microwave frequencies. All measurements were performed at temperature of 1,5 K.

The Landé $g-$factor for this compound is very high $g \approx 9{,}5$ [81] meaning that the resonant field for frequencies around 150 GHz is approximately 1,1 T. Thus, we have also tried to mount the frequency multipliers, specifically the tripler, and we irradiated the sample also with frequency $f = 370$ GHz. Specific ODMR measurement data sets are shown in table 5.2.

Sadly, remarkably same results, as in the previous section, were acquired from the ODMR measurement.

Table 5.2: Experimental values of ODMR measurements for $ErPc_2$ powder-like sample. E corresponds to the value of energy in MCD spectrum, B_R represent the value of magnetic field for which the resonance occurs for given frequency f_R of microwave irradiation.

E [cm^{-1}]	14 800	15 400	15 400	16 500	16 500	17 600	18 900
B_R [T]	1,1	1,0	2,8	1,0	1,1	1,1	2,8
f_R [GHz]	150	140	370	140	150	150	370

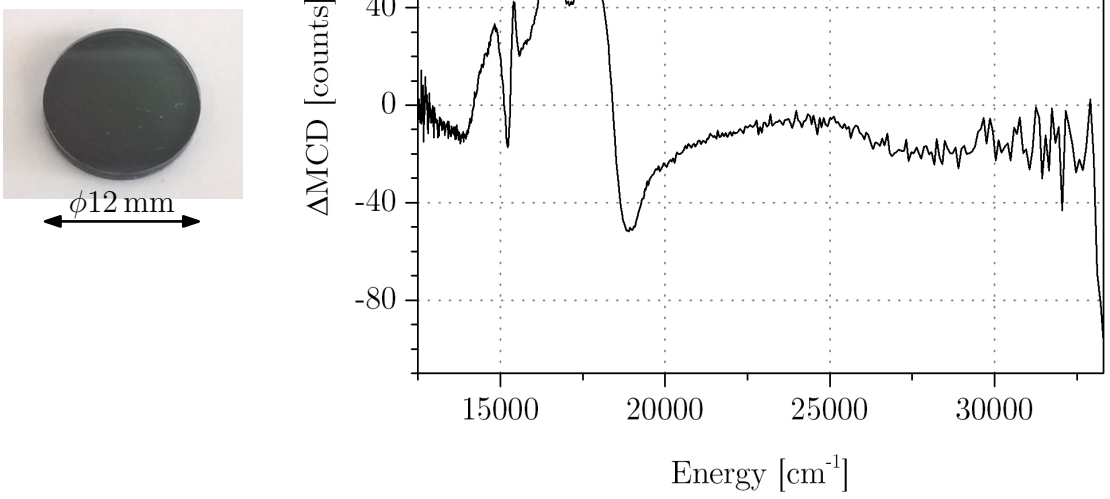

Figure 5.4: ΔMCD measurement of lanthanide based metal complex $ErPc_2$ powder-like sample recorded at 7 T and 1,5 K. The ODMR experiment was tried at almost every MCD signal ranging from 14 000 to 19 000 cm^{-1}. The MCD signal is remarkably similar, in case of the appearance, to the Q-band EPR measurement in [26], where a large broad peak is carved up with sharp, high intensity peaks. The large broad peak is most probably interband transition, whereas the sharp and steepy represent magnetic transitions.

5.3. CuPc

CuPc is another representative of organic molecules group of transition metal phthalocyanine complex. Due to a number of remarkable properties, phthalocyanines are recently very popular objects of investigation and have a promising future of many applications in organic electronics involved in thin film devices or as single molecule magnet [78, 79, 82, 83].

CuPc was one of the first molecules that were observed individually by scanning tunnelling microscopy and its subatomic scale features were partially revealed. [78] Recently CuPc was studied as a candidate for application in organic solar cells devices [83, 84].

We have studied CuPc sample in two forms: powder and thin film. The Landé $g-$factor is both for thin film and for powder approximately $g \approx 2{,}1$ [26, 84]. In the figures 5.5 and 5.6 both powder and 100 nm thin film samples are shown together with the MCD spectra at 5 T and 6 T respectively, at temperature of 1,5 K. We have investigated these two samples with frequencies about 150 GHz with fields ranging around 5 T. All used values for ODMR measurement are specified in the table 5.3.

Table 5.3: Experimental values of ODMR measurements for CuPc samples in form of powder and thin film. E corresponds to the value of energy in MCD spectrum, B_R represent the value of magnetic field for which the resonance occurs for given frequency f_R of microwave irradiation.

Form of the sample:	Powder			
E [cm^{-1}]	17 600	17 600	24 400	24 400
B_R [T]	4,8	5,1	4,8	5,1
f_R [GHz]	141	150	141	150
Form of the sample:	Thin film			
E [cm^{-1}]	17 200	17 200	20 500	20 500
B_R [T]	4,8	5,1	4,8	5,1
f_R [GHz]	141	150	141	150

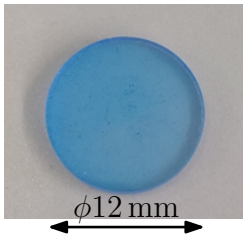

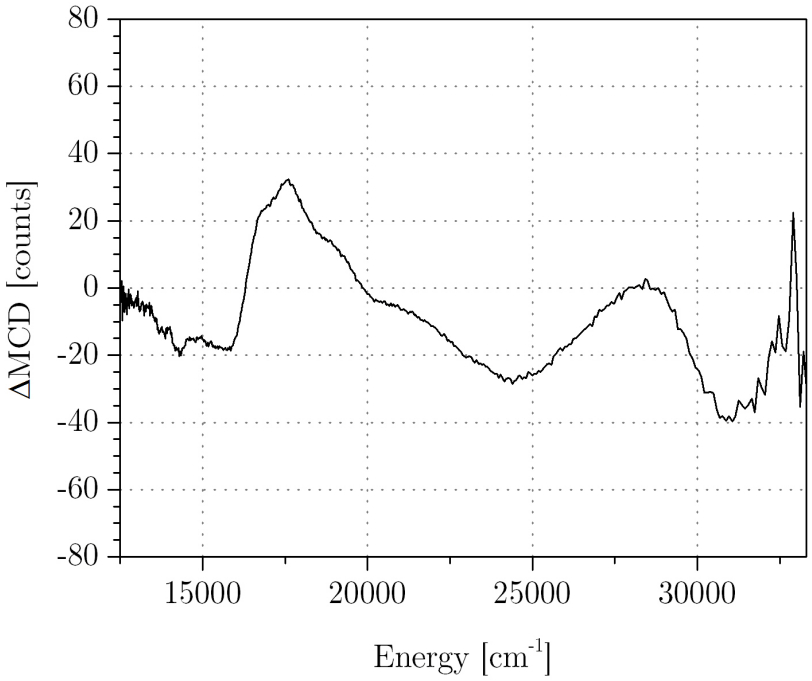

Figure 5.5: ΔMCD measurement of transition metal phthalocyanine complex CuPc powder-like sample recorded at 5 T and 1,5 K.

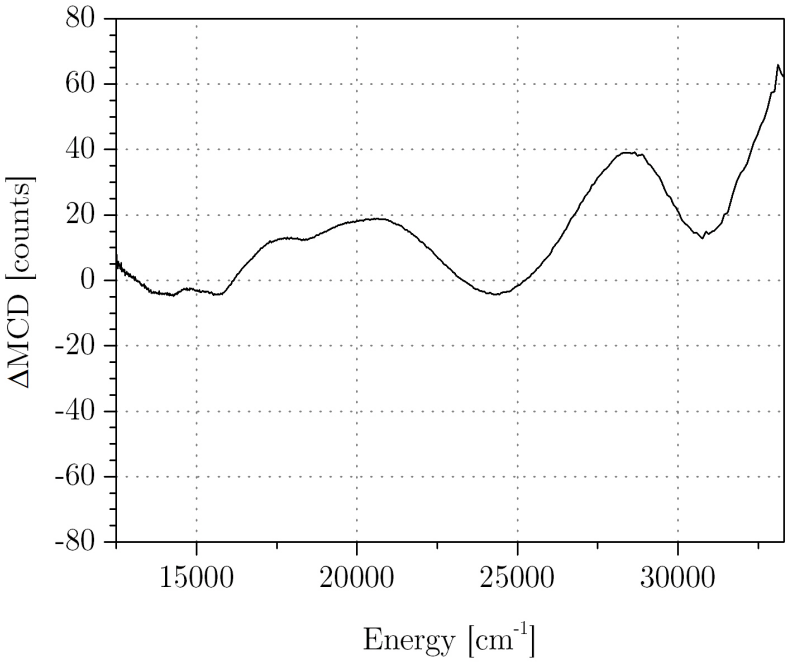

Figure 5.6: ΔMCD measurement of transition metal phthalocyanine complex CuPc 100 nm thin film sample recorded at 6 T and 1,5 K.

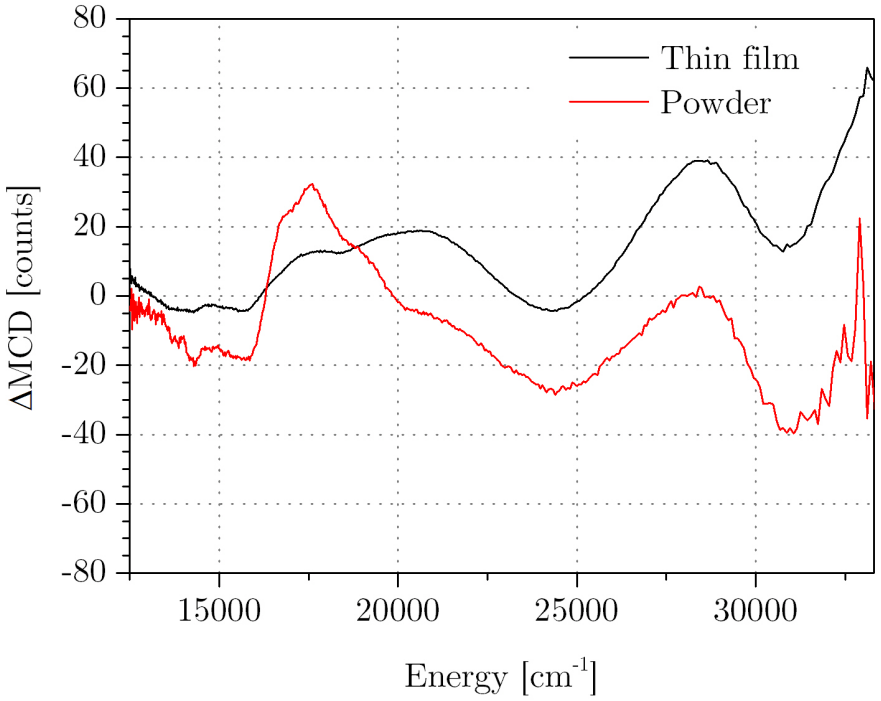

Figure 5.7: Comparison between ΔMCD measurement of transition metal phthalocyanine complex CuPc powder-like and thin film sample recorded at 5 T and 6 T respectively, both at temperature of 1,5 K. With a little bit of imaging the peaks, which are most probably interband transitions, corresponds rather nicely to each other.

5.4. MnPc

MnPc as another representative of transition metal phthalocyanine complexes, it shares the possible application as radiation and electrochemical sensors [85, 86], spin filters [87] or various components of semiconductor and displaying devices [78]. In recent years molecular and supramolecular magnetic properties of MnPc containing Li as central atoms have been reported [78].

We have studied MnPc in a form of powder. The sample can be seen in figure 5.8 together with the MCD spectrum at 7 T and temperature of 1,5 K. The Landé $g-$factor for MnPc is $g \approx 2$ [26]. The resulting ODMR measurement information can be found in table 5.4.

Table 5.4: Experimental values of ODMR measurements for MnPc powder-like sample. E corresponds to the value of energy in MCD spectrum, B_R represent the value of magnetic field for which the resonance occurs for given frequency f_R of microwave irradiation.

E [cm^{-1}]	15 200	15 200	18 700	20 500
B_R [T]	5,3	5,0	5,3	5,3
f_R [GHz]	148	140	148	148

During the second ODMR measurement of this sample ($E = 15\,200\,\mathrm{cm}^{-1}$, $B_R = = 5{,}0\,\mathrm{T}$ and $f_R = 140\,\mathrm{GHz}$) we gained a discussable result. While sweeping the field from 4,9 to 5,7 T with the sweeping rate of 0,01 T/min we recorded feasible peak in intensity measurement which corresponded to the resonant field $B_R = 5{,}0\,\mathrm{T}$. However, any attempts to reproduce this measurement were unsuccessful regardless the number of repetition and amount of concerted effort. The bandwidth and little misplacement can be due to the possible unclear frequency of microwaves generated by the BWO source. The ODMR intensity measurement of this specific "result" can be seen in the figure 5.9.

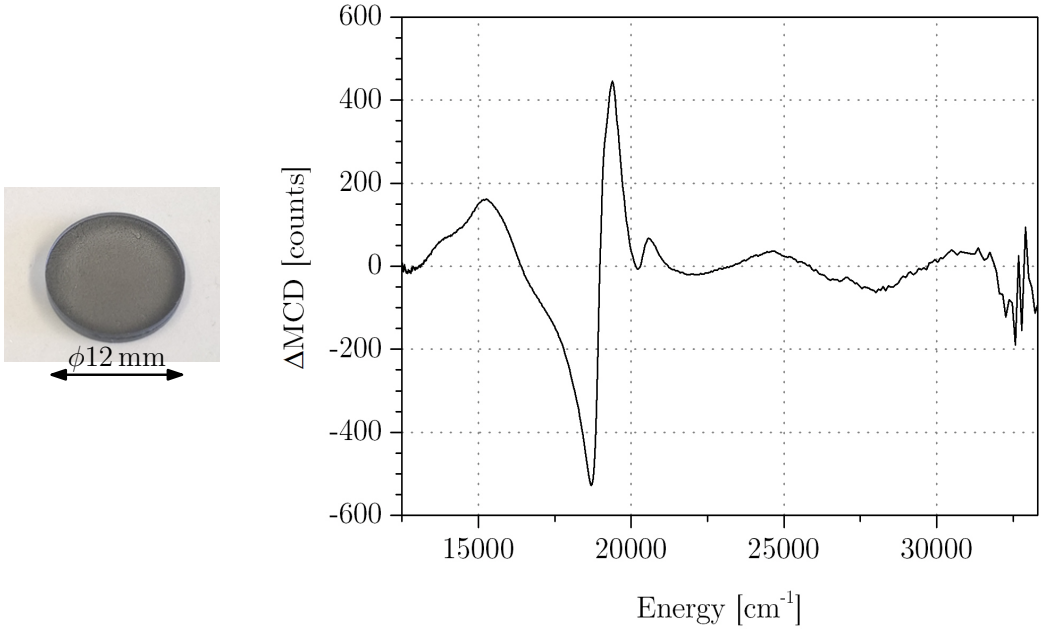

Figure 5.8: ΔMCD measurement of transition metal phthalocyanine complex MnPc thin film sample recorded at 7 T and 1,5 K. The strong MCD signal at 18 900 cm^{-1} suggests the presence of C term - ground state degeneracy and corresponds rather nicely with literature [88].

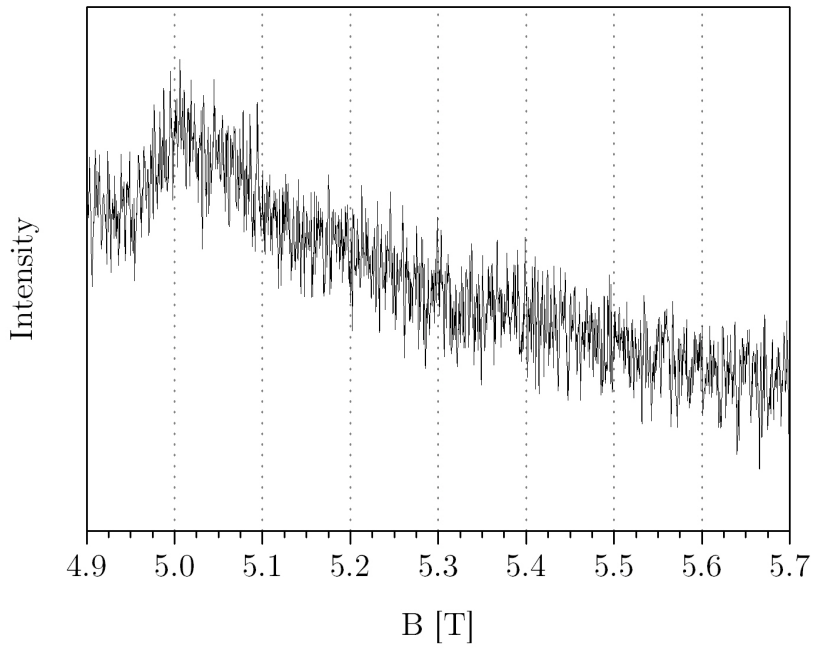

Figure 5.9: The possible result of ODMR measurement of MnPc powder-like sample. Spectrum was recorded at $E = 15\,200\,cm^{-1}$, which corresponds to wavelength of $\lambda \approx 658$ nm with microwave irradiation of frequency $f_R = 140$ GHz. The peak in intensity agrees with the predicted resonant field at $B_R \approx 5{,}0$ T. The bandwidth and small misplacement can be due to the inaccurate frequency of microwaves.

Conclusion

The presented master's thesis deals with the development of new experimental ODMR setup as a result of modification of standard VIS/UV MCD spectrometer built around 10T Oxford Instruments cryostat (*Spectromag*), into which a microwave irradiation of a sample is added.

Within the three chapters in the first half of the thesis, necessary theoretical introduction into the basics of resonance spectroscopy methods is demonstrated.

The second part, divided into two chapters, is dedicated to the practical solution of difficulties which have arisen during the construction of the new setup.

Firstly, before the construction itself, several designs and calculations were made. In order to couple two different types of radiation, we have used VIS/microwave (THz) dichroic ITO coated mirror. We have simulated the behaviour of microwave irradiation based on the free space approximation of Gaussian beam propagation. Microwave generator has to be placed in a safe distance from the stray field of magnet, where the sample is inserted, therefore, there was a need of a quasi-optical beam guiding system. We have chosen to guide microwave beam through series of quasi-optical lenses and to determine their positions, three different approaches were taken using three various programs: firstly *ZEMAX OpticStudio*; secondly computing environment *MATLAB* and thirdly a specific program from *Thomas Keating Ltd* company. The rough results were gained from the firstly stated program. The second one improved previous calculations which were then verified by simulations obtained from the mentioned company.

In order to irradiate the sample also with lower microwave frequencies, the design of antenna determined for the placement beneath the sample is offered. However, functionality of the first generation of antennas, manufactured by the process of optical lift-off lithography, was not as good as we expected. After multiple temperature cycle tests, the characteristics were heavily altered. Therefore, we have decided to change the process of manufacture resulting in the second generation of antenna design.

The last part of the thesis is dedicated to examination of the new ODMR spectrometer capabilities. Multiple measurements of various transition and lanthanide based metal complexes were performed. First of all, the Chromium(III) complex in three different forms – single crystal, powder and solution – was measured. That was followed by investigation of lanthanide based metal complex $ErPc_2$ double-decker and phthalocyanine complex CuPc, which was in two forms, powder and thin film as well. The last presented sample is another representative of phthalocyanine complexes MnPc. During the ODMR measurement of this sample we have recorded conceivable intensity peak which corresponds rather nicely to the expected resonant field. Regardless the amount of concerted effort, any attempts to reproduce this signal were unsuccessful. Therefore, the newly developed setup of ODMR spectrometer is subjected to further testing and improvements.

References

[1] NĚMEC, Petr. Cesta ke spinovemu tranzistoru. *Sdělovací technika* [online]. 2012, pp. 5–7. Available from: `http://physics.mff.cuni.cz/kchfo/ooe/soubory/110/sdelovaci-technika-6-5-8-2012.pdf`.

[2] LEE, Sang-Yun, Seoyoung PAIK, Dane R. MCCAMEY and Christoph BOEHME. Modulation frequency dependence of continuous-wave optically/electrically detected magnetic resonance. *Physical Review B*. 2012, vol. 86, no. 11, pp. 115204. ISSN 1098-0121. Available from: doi:10.1103/PhysRevB.86.115204.

[3] BINGHAM, Stephen J., Dieter SUTER, Arthur SCHWEIGER and Andrew J. THOMSON. Optical detection of transition metal ion electron paramagnetic resonance by coherent Raman spectroscopy. *Chemical Physics Letters*. 1997, vol. 266, no. 5, pp. 543–547. ISSN 00092614. Available from: doi:10.1016/S0009-2614(97)00031-6.

[4] KÖHLER, J., J. A. J. M. DISSELHORST, M. C. J. M. DONCKERS, E. J. J. GROENEN, J. SCHMIDT and W. E. MOERNER. Magnetic resonance of a single molecular spin. *Nature*. 1993, vol. 363, no. 6426, pp. 242–244. ISSN 0028-0836. Available from: doi:10.1038/363242a0.

[5] WRACHTRUP, J., C. von BORCZYSKOWSKI, J. BERNARD, M. ORRITT and R. BROWN. Optical detection of magnetic resonance in a single molecule. *Nature*. 1993, vol. 363, no. 6426, pp. 244–245. ISSN 0028-0836. Available from: doi:10.1038/363244a0.

[6] REYHER, H-J, B FAUST, B SUGG, R RUPP and L ACKERMANN. Optically detected magnetic resonance via the magnetic circular dichroism of absorption of cerium impurities in bulk paramagnetic terbium gallium garnet. *Journal of Physics: Condensed Matter*. 1999, vol. 9, no. 42, pp. 9065–9082. ISSN 0953-8984. Available from: doi:10.1088/0953-8984/9/42/020.

[7] BRIAT, B, M T BOROWIEC, H Bou RJEILY, F RAMAZ, A HAMRI and H SZYMCZAK. Combined Optical/MCD/ODMR investigations of photochromism in doubly-doped Bi 12 GeO 20. *Radiation Effects and Defects in Solids* [online]. 2002, vol. 157, no. 6-12, pp. 989–993. ISSN 1042-0150. Available from: doi:10.1080/10420150215806. Available from: `http://dx.doi.org/10.1080/10420150215806`.

[8] JEON, Duk Y, H P GISLASON and George D WATKINS. Optical detection of magnetic resonance of the zinc vacancy in ZnSe via magnetic circular dichroism. *Phys. Rev. B*. 1993, vol. 48, no. 11, pp. 7872–7883. Available from: doi:10.1103/PhysRevB.48.7872.

[9] GESCHWIND, Stanley. *Electron paramagnetic resonance.* New York: Plenum Press, 1972. ISBN 0306305801.

[10] ROMANOV, N.G., D.O. TOLMACHEV, A.S. GURIN, Y.A. USPENSKAYA, E.V. EDINACH, H.R. ASATRYAN, A.G. BADALYAN, P.G. BARANOV, A.G. PETROSYAN, H. WIECZOREK and C. RONDA. The Gd–Ce Cross-Relaxation Effects in ODMR via Ce^{3+} Emission in Garnet Crystals. *Applied Magnetic Resonance*. 2016, vol. 47, no. 7, pp. 737–744. ISSN 09379347. Available from: doi:10.1007/s00723-016-0795-3.

[11] BLOEMBERGEN, N., S. SHAPIRO, P. S. PERSHAN and J. O. ARTMAN. Cross-relaxation in spin systems. *Physical Review*. 1959, vol. 114, no. 2, pp. 445–459. ISSN 0031899X. Available from: doi:10.1103/PhysRev.114.445.

[12] GATTESCHI, Dante, Roberta SESSOLI and Jacques VILLAIN. *Molecular Nanomagnets* [online]. Oxford Scholarship, 2007. ISBN 9780191718298. Available from: doi:10.1093/acprof:oso/9780198567530.001.0001.

[13] DU TRÉMOLET DE LACHEISSERIE, Etienne, Damien GUGNOUX and Michel SCHLENKER. *Magnetism: Fundamentals*. 1st ed. Springer US, 2005. ISBN ISBN 0-387-22967-1.

[14] WERNSDORFER, Wolfgang. A long-lasting phase. *Nature nanotechnology*. 2007, vol. 6, no. March, pp. 174–176. ISSN 1476-1122. Available from: doi:10.1038/nmat1852.

[15] *Jens Kortus: Molecular Magnetism*. [online]. [Visited on 2017-5-24]. Available from: `http://www.physik.tu-freiberg.de/~kortus/kortus-research.html`.

[16] COEY, JMD. *Magnetism and magnetic materials*. Cambridge University Press, 2010. ISBN 0521846149.

[17] REED, M. D., L. DICARLO, S. E. NIGG, L. SUN, L. FRUNZIO, S. M. GIRVIN and R. J. SCHOELKOPF. Realization of Three-Qubit Quantum Error Correction with Superconducting Circuits. *Nature* [online]. 2011, vol. 482, no. 7385, pp. 382–385. ISSN 0028-0836. Available from: doi:10.1038/nature10786.

[18] WERNSDORFER, Wolfgang. Molecular magnets: chemistry brings qubits together. *Nature nanotechnology*. 2009, vol. 4, no. 3, pp. 145–6. ISSN 1748-3395. Available from: doi:10.1038/nnano.2009.21.

[19] DIVINCENZO, David P. and IBM. The Physical Implementation of Quantum Computation. [online]. 2000. ISSN 00158208. Available from: doi:10.1002/1521-3978(200009)48:9/11<771::AID-PROP771>3.0.CO;2-E.

[20] LEUENBERGER, Michael N Loss Daniel. Quantum computing in molecular magnets. *Nature*. 2001, vol. 410, no. 6830, pp. 789. ISSN 00280836.

[21] LLOYD, Seth. Quantum search without entanglement. *Physical Review A* [online]. 1999, vol. 61, no. 1, pp. 10301. ISSN 1050-2947. Available from: doi:10.1103/PhysRevA.61.010301.

[22] EKERT, Artur and Richard JOZSA. Quantum computation and Shor's factoring algorithm. *Reviews of Modern Physics*. 1996, vol. 68, no. 3, pp. 733–753. ISSN 00346861. Available from: doi:10.1103/RevModPhys.68.733.

[23] SORNETTE, D. and M. J. WERNER. Statistical Physics Approaches to Seismicity. *ArXiv* [online]. 2008, pp. 71. ISSN 9780387758886. Available from: doi:10.1007/978-0-387-30440-3.

[24] CLARK, R. G., R. BRENNER, T. M. BUEHLER, V. CHAN, N. J. CURSON, A. S. DZURAK, E. GAUJA, H. S. GOAN, A. D. GREENTREE, T. HALLAM, A. R. HAMILTON, L. C. L. HOLLENBERG, D. N. JAMIESON, J. C. MCCALLUM, G. J. MILBURN, J. L. O'BRIEN, L. OBERBECK, C. I. PAKES, S. D. PRAWER, D. J. REILLY, F. J. RUESS, S. R. SCHOFIELD, M. Y. SIMMONS, F. E. STANLEY, R. P. STARRETT, C. WELLARD and C. YANG. Progress in silicon-based quantum computing. *Philosophical Transactions of the Royal Society A: Mathematical, Physical and Engineering Sciences*. 2003, vol. 361, no. 1808, pp. 1451–1471. ISSN 1364-503X. Available from: doi:10.1098/rsta.2003.1221.

[25] KANE, B. E. A silicon-based nuclear spin quantum computer. *Nature*. 1998, vol. 393, no. 6681, pp. 133–137. ISSN 00280836. Available from: doi:10.1038/30156.

[26] BADER, K., M. WINKLER and J. van SLAGEREN. Tuning of molecular qubits: very long coherence and spin–lattice relaxation times. *Chem. Commun.* 2016, vol. 52, no. 18, pp. 3623–3626. ISSN 1359-7345. Available from: doi:10.1039/C6CC00300A.

[27] *CuPc | Copper(II) phthalocyanine triple-sublimed grade*. [online]. [Visited on 2017-5-24]. Available from: `http://www.sigmaaldrich.com/catalog/product/aldrich/702854?lang=de%7B%5C&%7Dregion=DE`.

[28] DREISER, J. Molecular lanthanide single-ion magnets: from bulk to submonolayers. *Journal of Physics: Condensed Matter*. 2015, vol. 27, no. 18, pp. 183203. ISSN 0953-8984. Available from: doi:10.1088/0953-8984/27/18/183203.

[29] PIRAMANAYAGAM, S.N. and T.C. CHONG. Development in Data Storage. 2012, pp. 331.

[30] *Flash Memory Areal Densities Exceed Those of Hard Drives*. [online]. [Visited on 2017-5-24]. Available from: `https://www.forbes.com/sites/tomcoughlin/2016/02/03/flash-memory-areal-densities-exceed-those-of-hard-drives/%7B%5C#%7D2be6638e7c72`.

[31] RECHKEMMER, Yvonne, Frauke D. BREITGOFF, Margarethe van der MEER, Mihail ATANASOV, Michael HAKL, Milan ORLITA, Petr NEUGEBAUER, Frank NEESE, Biprajit SARKAR and Joris van SLAGEREN. A four-coordinate cobalt(II) single-ion magnet with coercivity and a very high energy barrier. *Nature Communications*. 2016, vol. 7, pp. 10467. ISSN 2041-1723. Available from: doi:10.1038/ncomms10467.

[32] WEIL, John A. and James R. BOLTON. *Electron Paramagnetic Resonance* [online]. 2nd Editio. 2006. ISBN 978-0-471-75496-1.

[33] HALLIDAY, David, Robert RESNICK and Jearl WALKER. *Fundamentals of Physics, 9th Edition*. 9th editio. Wiley, 2010. ISBN 978-0-470-55653-5.

[34] PETR NEUGEBAUER. *Development of a Heterodyne High Field / High Frequency Electron Paramagnetic Resonance Spectrometer at 285 GHz*. 2010. PhD thesis. Université Joseph-Fourier - Grenoble.

[35] DELFS, C. D., D. GATTESCHI and L. PARDI. *High Nuclearity Spin Clusters: A New Dimension in Magnetism?* 1993. Available from: doi:10.1080/02603599308035834.

[36] SESSOLI, R., D. GATTESCHI, A. CANESCHI and M. A. NOVAK. Magnetic bistability in a metal-ion cluster. *Nature*. 1993, vol. 365, no. 6442, pp. 141–143. ISSN 0028-0836. Available from: doi:10.1038/365141a0.

[37] SLAGEREN, Joris Van. *Introduction to Molecular Magnetism* [online]. 2005. Available from: `http://obelix.physik.uni-bielefeld.de/%7B~%7Dschnack/molmag/material/123.pdf`.

[38] FRIEDMAN, Jonathan R. and Myriam P. SARACHIK. Single-Molecule Nanomagnets. *Annual Review of Condensed Matter Physics* [online]. 2010, vol. 1, no. 1, pp. 109–128. ISSN 1947-5454. Available from: doi:10.1146/annurev-conmatphys-070909-104053.

[39] DOHERTY, Marcus W., Neil B. MANSON, Paul DELANEY, Fedor JELEZKO, Jörg WRACHTRUP and Lloyd C L HOLLENBERG. The nitrogen-vacancy colour centre in diamond. *Physics Reports* [online]. 2013, vol. 528, no. 1, pp. 1–45. ISSN 03701573. Available from: doi:10.1016/j.physrep.2013.02.001.

[40] RONDIN, L, J P TETIENNE, T HINGANT, J F ROCH, P MALETINSKY and V JACQUES. Magnetometry with nitrogen-vacancy defects in diamond. *Rep Prog Phys* [online]. 2014, vol. 77, no. 5, pp. 56503. ISSN 0034-4885. Available from: doi:10.1088/0034-4885/77/5/056503.

[41] BALASUBRAMANIAN, Gopalakrishnan, Philipp NEUMANN, Daniel TWITCHEN, Matthew MARKHAM, Roman KOLESOV, Norikazu MIZUOCHI, Junichi ISOYA, Jocelyn ACHARD, Johannes BECK, Julia TISSLER, Vincent JACQUES, Philip R. HEMMER, Fedor JELEZKO and Jörg WRACHTRUP. Ultralong spin coherence time in isotopically engineered diamond. *Nature Materials*. 2009, vol. 8, no. 5, pp. 383–387. ISSN 1476-1122. Available from: doi:10.1038/nmat2420.

[42] DEGEN, C. L. Scanning magnetic field microscope with a diamond single-spin sensor. *Applied Physics Letters* [online]. 2008, vol. 92, no. 24, pp. 243111. ISSN 00036951. Available from: doi:10.1063/1.2943282.

[43] SHERSHULIN, V A, S R SAMOYLENKO, O S KUDRYAVTSEV, A P BOLSHAKOV, E E ASHKINAZI, V Yu YUROV, V G RALCHENKO, V I KONOV and I I VLASOV. Confocal luminescence study of nitrogen-vacancy distribution within nitrogen-rich single crystal CVD diamond. *Laser Physics*. 2016, vol. 26, no. 1, pp. 015202. ISSN 1054-660X. Available from: doi:10.1088/1054-660X/26/1/015202.

[44] HALL, L. T., C. D. HILL, J. H. COLE and L. C. L. HOLLENBERG. Ultrasensitive diamond magnetometry using optimal dynamic decoupling. *Physical Review B - Condensed Matter and Materials Physics* [online]. 2010, vol. 82, no. 4, pp. 045208. ISSN 10980121. Available from: doi:10.1103/PhysRevB.82.045208.

[45] MERILES, Carlos A., Liang JIANG, Garry GOLDSTEIN, Jonathan S. HODGES, Jeronimo MAZE, Mikhail D. LUKIN and Paola CAPPELLARO. Imaging mesoscopic nuclear spin noise with a diamond magnetometer. *Journal of Chemical Physics* [online]. 2010, vol. 133, no. 12, pp. 124105. ISSN 00219606. Available from: doi:10.1063/1.3483676.

[46] MCGUINNESS, L. P., Y. YAN, A. STACEY, D. A. SIMPSON, L. T. HALL, D. MACLAURIN, S. PRAWER, P. MULVANEY, J. WRACHTRUP, F. CARUSO, R. E. SCHOLTEN and L. C. L. HOLLENBERG. Quantum measurement and orientation tracking of fluorescent nanodiamonds inside living cells. *Nature Nanotechnology*. 2011, vol. 6, no. 6, pp. 358–363. ISSN 1748-3387. Available from: doi:10.1038/nnano.2011.64.

[47] DOHERTY, Marcus W, Viktor V STRUZHKIN, David A SIMPSON, Liam P. MCGUINNESS, Yufei MENG, Alastair STACEY, Timothy J KARLE, Russell J HEMLEY, Neil B MANSON, Lloyd C. L. HOLLENBERG and Steven PRAWER. Electronic Properties and Metrology Applications of the Diamond NV− Center under Pressure. *Physical Review Letters* [online]. 2014, vol. 112, no. 4, pp. 047601. ISSN 0031-9007. Available from: doi:10.1103/PhysRevLett.112.047601.

[48] TOYLI, D. M., D. J. CHRISTLE, A. ALKAUSKAS, B. B. BUCKLEY, C. G. VAN DE WALLE and D. D. AWSCHALOM. Measurement and control of single nitrogen-vacancy center spins above 600 K. *Physical Review X* [online]. 2012, vol. 2, no. 3, pp. 031001. ISSN 21603308. Available from: doi:10.1103/PhysRevX.2.031001. Available from: `https://link.aps.org/doi/10.1103/PhysRevX.2.031001`.

[49] CHIPAUX, Mayeul, Alexandre TALLAIRE, Jocelyn ACHARD, Sebastien PEZZAGNA, Jan MEIJER, Vincent JACQUES, Jean Francois ROCH and Thierry DEBUISSCHERT. Magnetic imaging with an ensemble of nitrogen vacancy-centers in diamond. *European Physical Journal D* [online]. 2015, vol. 69, no. 7, pp. 1–11. ISSN 14346079. Available from: doi:10.1140/epjd/e2015-60080-1.

[50] JELEZKO, F. and J. WRACHTRUP. *Single defect centres in diamond: A review*. 2006. ISBN 1862-6300. Available from: doi:10.1002/pssa.200671403.

[51] BUCKINGHAM, A. D. and P. J. STEPHENS. Magnetic Optical Activity. *Annual Review of Physical Chemistry*. 1966, vol. 17, no. 1, pp. 399–432. ISSN 0066-426X. Available from: doi:10.1146/annurev.pc.17.100166.002151.

[52] STEPHENS, P.J. Magnetic Circular Dichroism. *Annu. Rev. Phys. Chem.* 1974, vol. 25, no. 1, pp. 201–232. ISSN 0066-426X. Available from: doi:10.1146/annurev.pc.22.100171.001355.

[53] MASON, W. Roy. *A Practical Guide to Magnetic Circular Dichroism Spectroscopy*. Hoboken, NJ, USA: John Wiley & Sons, Inc., 2007. ISBN 9780470139233. Available from: doi:10.1002/9780470139233.

[54] FASMAN, Gerald D. *Circular Dichroism and the Conformational Analysis of Biomolecules* [online]. 1st ed. Boston, MA: Springer US, 1996. ISBN 978-1-4419-3249-5. Available from: doi:10.1007/978-1-4757-2508-7.

[55] RECHKEMMER, Yvonne. *Spectroscopic Investigations of the Magnetic Anisotropy of Lanthanide- and Cobalt-Based Molecular Nanomagnets*. 2016. PhD thesis. Universität Stuttgart.

[56] NEESE, Frank and Edward I SOLOMON. MCD C-Term signs, saturation behavior, and determination of band polarizations in randomly oriented systems with spin S â‰¥ 1/2. Applications to S = 1/2 and S = 5/2. *Inorg. Chem.* 1999, vol. 38, no. 8, pp. 1847–1865. ISSN 0020-1669. Available from: doi:10.1021/ic981264d.

[57] SPAETH, Johann-Martin, Jürgen R. NIKLAS and Ralph H BARTRAM. *Structural Analysis of Point Defects in Solids: An Introduction to Multiple Magnetic Resonance Spectroscopy*. 1992. ISBN 978-3-642-84407-2,978-3-642-84405-8.

[58] BINGHAM, Stephen J, Jörg GUTSCHANK, Birgit BÖRGER, Dieter SUTER and Andrew J THOMSON. Magnetic circular dichroism anisotropy from coherent Raman detected electron paramagnetic resonance spectroscopy: Application to spin-1/2 transition metal ion centers in proteins. *The Journal of Chemical Physics*. 2000, vol. 113, no. 10, pp. 4331. ISSN 00219606. Available from: doi:10.1063/1.1288142.

[59] BÖRGER, Birgit, Stephen J. BINGHAM, Jörg GUTSCHANK, Marc Oliver SCHWEIKA, Dieter SUTER and Andrew J. THOMSON. Optically detected electron paramagnetic resonance by microwave modulated magnetic circular dichroism. *The Journal of Chemical Physics*. 1999, vol. 111, no. 18, pp. 8565. ISSN 00219606. Available from: doi:10.1063/1.480197.

[60] ROGULIS, Uldis. Optical detection of paramagnetic centres: From crystals to glass-ceramics. *Low Temperature Physics*. 2016, vol. 42, no. 7, pp. 539–542. ISSN 1063-777X. Available from: doi:10.1063/1.4959009.

[61] SEARCH, Home, Collections JOURNALS, About CONTACT, My IOPSCIENCE, Solid State PHYS and I P ADDRESS. Zero-field optically detected magnetic resonance (ZF- ODMR) in semiconductors. *J. Phys.* 1984, vol. 251, pp. 1–6.

[62] BARANOV, P. G. and N. G. ROMANOV. Magnetic resonance in micro- and nanostructures. *Applied Magnetic Resonance*. 2001, vol. 21, no. 2, pp. 165–193. ISSN 0937-9347. Available from: doi:10.1007/BF03162450.

[63] CHILDRESS, L., M. V. GURUDEV DUTT, J. M. TAYLOR, A. S. ZIBROV, F. JELEZKO, J. WRACHTRUP, P. R. HEMMER and M. D. LUKIN. Coherent Dynamics of Coupled Electron and Nuclear Spin Qubits in Diamond. *Science* [online]. 2006, vol. 314, no. 5797, pp. 281–285. ISSN 0036-8075. Available from: doi:10.1126/science.1131871.

[64] BARANOV, P.G., V.V. DYAKONOV, N.G. ROMANOV and V.A. VETROV. Optical Detection of Magnetic Resonance without Microwaves VIA MCD of F-Centers in Doped Alkali Halides. *Radiation Effects and Defects in Solids*. 1991, vol. 119-121, no. 1, pp. 165–170. ISSN 10294953 10420150. Available from: doi:10.1080/10420159108224872.

[65] Van OORT, E. and M. GLASBEEK. Optically detected adiabatic fast passage and cross-relaxation of the N-V center in diamond. *Applied Magnetic Resonance*. 1991, vol. 2, no. 2, pp. 291–300. ISSN 09379347. Available from: doi:10.1007/BF03166042.

[66] WANG, Hai-Jing, Chang S. SHIN, Scott J. SELTZER, Claudia E. AVALOS, Alexander PINES and Vikram S. BAJAJ. Optically detected cross-relaxation spectroscopy of electron spins in diamond. *Nature Communications* [online]. 2014, vol. 5. ISSN 2041-1723. Available from: doi:10.1038/ncomms5135.

[67] LEE, K. M. and G. D. WATKINS. Optical detection of cross relaxation in SiC. *Physical Review B*. 1982, vol. 26, no. 1, pp. 26–34. ISSN 01631829. Available from: doi:10.1103/PhysRevB.26.26.

[68] GOLDSMITH, Paul F. *Quasioptical Systems*. IEEE, 1998. ISBN 9780470546291. Available from: doi:10.1109/9780470546291.

[69] *Startseite / Präzisions Glas & Optik GmbH / Home page*. [online]. [Visited on 2017-5-24]. Available from: `https://www.pgo-online.com/`.

[70] *Thorlabs - KS4 Ø4"; Precision Kinematic Mirror Mount, 2 Adjusters*. [online]. [Visited on 2017-5-24]. Available from: `https://www.thorlabs.com/thorproduct.cfm?partnumber=KS4%7B%5C#%7Dad-image-0`.

[71] *Home*. [online]. [Visited on 2017-5-24]. Available from: `https://www.cst.com/`.

[72] *Waveguide Sizes - Dimensions & Cutoff Frequency*. [online]. [Visited on 2017-5-24]. Available from: `https://www.everythingrf.com/tech-resources/waveguides-sizes`.

[73] LAMB, James W. Miscellaneous data on materials for millimetre and submillimetre optics. *International Journal of Infrared and Millimeter Waves*. 1996, vol. 17, no. 12, pp. 1997–2034. ISSN 0195-9271. Available from: doi:10.1007/BF02069487.

[74] YANG, Min K., Roger H. FRENCH and Edward W. TOKARSKY. Optical properties of Teflon® AF amorphous fluoropolymers. *Journal of Micro/Nanolithography, MEMS and MOEMS*. 2008, vol. 7, no. 3, pp. 033010. ISSN 15371646. Available from: doi:10.1117/1.2965541.

[75] SELF, S a. Focusing of spherical Gaussian beams. *Applied optics*. 1983, vol. 22, no. 5, pp. 658–61. ISSN 0003-6935. Available from: doi:10.1364/AO.22.000658.

[76] SASAKI, Kento, Yasuaki MONNAI, Soya SAIJO, Ryushiro FUJITA, Hideyuki WATANABE, Junko ISHI-HAYASE, Kohei M ITOH and Eisuke ABE. Broadband, large-area microwave antenna for optically detected magnetic resonance of nitrogen-vacancy centers in diamond. *Review of Scientific Instruments* [online]. 2016, vol. 87, no. 5, pp. 053904. ISSN 10897623. Available from: doi:10.1063/1.4952418.

[77] OTTO, Sven, Markus GRABOLLE, Christoph FÖRSTER, Christoph KREITNER, Ute RESCH-GENGER and Katja HEINZE. [Cr(ddpd)2]3+: A Molecular, Water-Soluble, Highly NIR-Emissive Ruby Analogue. *Angewandte Chemie - International Edition*. 2015, vol. 54, no. 39, pp. 11572–11576. ISSN 15213773. Available from: doi:10.1002/anie.201504894.

[78] De la TORRE, Gema, Christian G. CLAESSENS and Tomás TORRES. Phthalocyanines: old dyes, new materials. Putting color in nanotechnology. *Chem. Commun.* 2007, vol. 109, no. 20, pp. 2000–2015. ISSN 1359-7345. Available from: doi:10.1039/B614234F.

[79] WOODRUFF, Daniel N., Richard E. P. WINPENNY and Richard A. LAYFIELD. *Lanthanide single-molecule magnets*. 2013. ISBN 0009-2665. Available from: doi:10.1021/cr400018q.

[80] ZHANG, Jianping, Yao LI, Yu TANG, Xiao LUO, Lei SUN, Feiyu ZHAO, Junkang ZHONG and Yingquan PENG. Airstable near-infrared sensitive organic field-effect transistors utilizing erbium phthalocyanine as photosensitive layer. *Synthetic Metals*. 2016, vol. 218, pp. 27–33. ISSN 03796779. Available from: doi:10.1016/j.synthmet.2016.04.022.

[81] DÖRFEL, M. *Single Crystal Studies of the Magnetic Anisotropy of Molecular Nanomagnets*. Stuttgart: University of Stuttgart, 2015. 197 pp.

[82] ROGERS, J A, Z BAO, K BALDWIN, A DODABALAPUR, B CRONE, V R RAJU, V KUCK, H KATZ, K AMUNDSON, J EWING and P DRZAIC. Paper-like electronic displays: Large-area rubber-stamped plastic sheets of electronics and microencapsulated electrophoretic inks. *Proceedings of the National Academy of Sciences*. 2001, vol. 98, no. 9, pp. 4835–4840. ISSN 0027-8424. Available from: doi:10.1073/pnas.091588098.

[83] WARNER, Marc, Soumaya MAUTHOOR, Solveig FELTON, Wei WU, Jules A. GARDENER, Salahud DIN, Daniel KLOSE, Gavin W. MORLEY, A. Marshall STONEHAM, Andrew J. FISHER, Gabriel AEPPLI, Christopher W. M. KAY and Sandrine HEUTZ. Spin-based diagnostic of nanostructure in copper phthalocyanine-C 60 solar cell blends. *ACS Nano*. 2012, vol. 6, no. 12, pp. 10808–10815. ISSN 19360851. Available from: doi:10.1021/nn304156e.

[84] BOGUSLAVSKII, E. G., S. A. PROKHOROVA and V. A. NADOLINNYI. Evolution of ordered films of copper phthalocyanine according to EPR data. *Journal of Structural Chemistry*. 2005, vol. 46, no. 6, pp. 1014–1022. ISSN 00224766. Available from: doi:10.1007/s10947-006-0236-5.

[85] ARSHAK, A, S. ZLEETNI and K. ARSHAK. -radiation Sensor Using Optical and Electrical Properties of Manganese Phthalocyanine (MnPc) Thick Film. *Sensors* [online]. 2002, vol. 2, no. 5, pp. 174–184. ISSN 1424-8220. Available from: doi:10.3390/s20500174. Available from: `http://www.mdpi.com/1424-8220/2/5/174/`.

[86] ÇEKEN, Berna, Mehmet KANDAZ and Atif KOCA. Electrochemical metal-ion sensors based on a novel manganese phthalocyanine complex. *Synthetic Metals*. 2012, vol. 162, no. 17-18, pp. 1524–1530. ISSN 03796779. Available from: doi:10.1016/j.synthmet.2012.07.019.

[87] SHEN, Xin, Lili SUN, Enrico BENASSI, Ziyong SHEN, Xingyu ZHAO, Stefano SANVITO and Shimin HOU. Spin filter effect of manganese phthalocyanine contacted with single-walled carbon nanotube electrodes. *Journal of Chemical Physics*. 2010, vol. 132, no. 5, pp. 054703. ISSN 00219606. Available from: doi:10.1063/1.3302258.

[88] WILLIAMSON, Bryce E., Thomas C. VANCOTT, Michael E. BOYLE, G. Christian MISENER, Martin J. STILLMAN and Paul N. SCHATZ. Determination of the ground state of manganese phthalocyanine in an argon matrix using magnetic circular dichroism and absorption spectroscopy. *Journal of the American Chemical Society*. 1992, vol. 114, no. 7, pp. 2412–2419. ISSN 0002-7863. Available from: doi:10.1021/ja00033a016.

[89] *Gaussian beam propagation through a series of thin lenses - File Exchange - MATLAB Central*. [online]. [Visited on 2017-5-24]. Available from: `https://www.mathworks.com/matlabcentral/fileexchange/37436-gaussian-beam-propagation-through-a-series-of-thin-lenses`.

A. Appendices

A.1. MATLAB script

Here the *MATLAB* script used for the calculation of Gaussian beam propagation through series of thin lenses is attached. The modified code is originally from [89].

```
function Gaussian_Propagation(lambda,beam_waist,wp,fpos,f,show_flag)
% propagates a Gaussian beam through a series of lenses.
% Input:
%   lambda          beam's wavelength
%   beam_waist      waist of the beam at the waist positions (wp)
%   wp              waist position
%   fpos            lenses positions vector [pos1, pos2, pos3 ...]
%   f               lenses focal-lengths vector [f1, f2, f3 ...]
%   show_flag       prints text on figure with waist positions and sizes
%
%   All units are metric.

if (nargin < 6); show_flag=0; end
if (nargin < 5); f=[0.120 0.120 0.120]; end
if (nargin < 4); fpos=[0.027 0.487 0.792]; end
if (nargin < 3);  wp=[0]; end
if (nargin < 2); beam_waist=3e-3; end
if (nargin < 1); lambda=750e-6; end

%% calculate the waist_pos(i) and w(i) between all of the lenses
w(1)=beam_waist;                % initial beam waist
waist_pos(1)=wp;                % initial beam waist position

for i=1:length(f)       % loop over all of the lenses vector
% calculate the new waist position relative to current lens position
waist_distance_from_next_lens=fpos(i)-waist_pos(i);
[new_w, new_rel_d] = ...
    Gaussian_focusing(lambda,w(i),waist_distance_from_next_lens,f(i));
w(i+1)=new_w;
% calculate the absolute position of the new waist
waist_pos(i+1)=fpos(i)+new_rel_d;
end

fpos=[waist_pos(1) fpos];
%generate propagation axis z, w(z) vector and plot it:
z(1)=waist_pos(1);
Wz(1)=w(1);
for i=1:length(fpos)-1      % cycle through all lenses
```

```
ztemp=linspace(fpos(i),fpos(i+1));       % just a 100 points propagation ...
    ztemp vector, can be modified to ...
    ztemp=linspace(fpos(i),fpos(i+1),num_of_points_desired);
Wz=[Wz w(i)*sqrt(1+((ztemp-waist_pos(i))/(pi*w(i)^2/lambda)).^2)];    % ...
    gaussian beam propagation
z=[z ztemp];
end

if fpos(end)+2*abs(f(end))>waist_pos(end)
ztemp=linspace(fpos(end),fpos(end)+2*abs(f(end)));   % propagate 2*f of ...
    the last lens - Change if needed to see larger propagation distances
else
ztemp=linspace(fpos(end),waist_pos(end)+2*abs(f(end)));   % propagate 2*f ...
    of the last beam waist - Change if needed to see larger propagation ...
    distances
end

Wz=[Wz w(end)*sqrt(1+((ztemp-waist_pos(end))/(pi*w(end)^2/lambda)).^2)];
z=[z ztemp];

%% beam plots:
figure(4)
plot(z,Wz,'r',z,-Wz,'r');          % plot the gaussian beam
hold on;
xlabel('z(m)'); ylabel('y(m)');

% lenses plot:
xline=kron(fpos(2:end),[1 1]');
yline=2*kron(max(abs(Wz))*ones(length(fpos)-1,1)',[0.85 -0.85]');
plot(xline,yline,'b:')
% legend('beam waist (+)','beam waist (-)','thin lens');
ZL=waist_pos(end);

% text anotations:
% text(fpos(2:end),1.05*yline(1,:),strcat('f= ',num2str(f')));     % ...
    prints the focal length of each lens
% text(fpos(2:end),-1.05*yline(1,:),strcat('Z_f= ...
    ',num2str(fpos(2:end)')));     % prints the focal length of each lens

if show_flag
% plots the waist location and size at different heights
ymax=max(yline(:));
text(waist_pos,w-0.05*ymax,strcat('W_{',num2str((1:length(waist_pos) ...
    )'),'}=',num2str(w','%0.3d')),'FontSize',8);
text(waist_pos,w+0.05*ymax,strcat('Z=',num2str(waist_pos','%0.4g')), ...
    'FontSize',8);
end

hold off
%waist_pos
%w
fprintf(1,strcat('waist position from last lens: ...
    ',num2str(waist_pos(end)-fpos(end)),'\n'))
fprintf(1,strcat('waist size: ',num2str(w(end)),'\n'))

function [w_new,s_new]=Gaussian_focusing(lambda,w_old,s_old,f)
% Gaussian beam focusing by a thin lens (Based on Self's paper, see [1])
% Inputs: lambda=wavelength;
```

```
85 %          w_old = waist before the lens;
86 %          s_old = distance of waist before lens (s>0 before lens)
87 %          f = focal length of lens (f>0 for converging lens)
88 % Output: w_new = new waist;
89 %          s_new = position of waist from lens
90 zR=pi*w_old^2/lambda;     % original rayleigh range
91 s_new = f.*(1+(s_old./f-1)./((s_old./f-1).^2+(zR./f).^2));  % new waist ...
       location (Eq. (9b))
92 w_new = w_old./sqrt((1-s_old./f).^2+(zR./f).^2);
```

A.2. Thomas Keating Ltd calculation

The large scale drawing of the calculation by Dr Kevin Pike from *Thomas Keating Ltd* is shown for the frequency of $f = 150\,\mathrm{GHz}$, which was used at most in the performed measurements. The figure is placed on separate page.

Calculation by *Thomas Keating Ltd* corresponds rather nicely to the result from *MATLAB* script in section 4.3.2 in matter of the beam waist positions. Values of the beam diameters need to be considered as half of the calculated numbers because of the small mistake in the input parameter, which was taken as radius instead of diameter (the input beam waist radius is $w_0 = 3{,}162\,\mathrm{mm}$, not $6{,}324\,\mathrm{mm}$, which corresponds to the value of beam diameter $12{,}648\,\mathrm{mm}$ set in the drawing). And since the beam radius dependence is given by equation 3.25, we can take the half of every value.

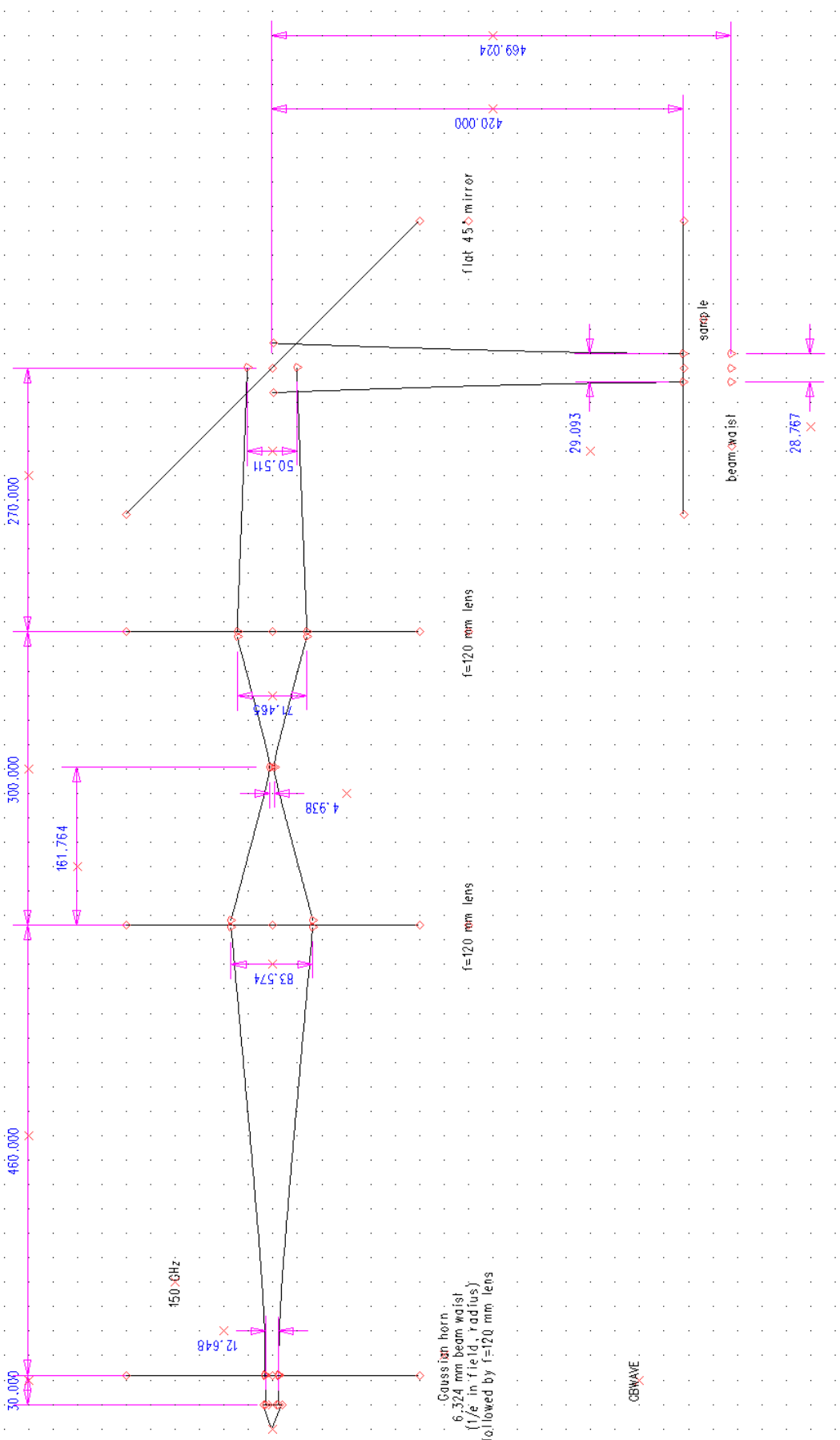
469.024
420.000
flat 45° mirror
sample
29.093
beam waist
28.767
50.511
270.000
f=120 mm lens
71.465
300.000
4.938
161.764
f=120 mm lens
83.574
460.000
150 GHz
12.648
30.000
Gaussian horn
6.324 mm beam waist
(1/e^2 field radius)
followed by f=120 mm lens
OSWAVE

A.3. Technical drawings - NV Centres Sample Holder

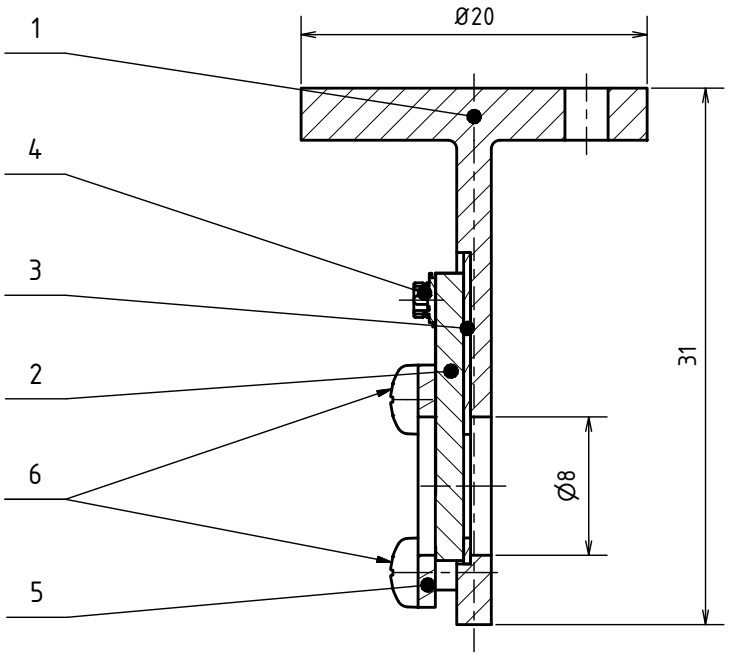

PARTS LIST				
ITEM	NAME	MATERIAL	SHEET NUMB	QUANTITY
1	HOLDER	Messing	2	1
2	SAMPLE	Glass		1
3	PTFE ISOLATOR	Teflon	4	1
4	SMD CONNECTOR			1
5	SAMPLE MOUNTING	Messing	3	1
6	ISO 7045 H - M2x4			4

Material:		Scale: 3 : 1	Name: NV'S SAMPLE HOLDER ASSEMBLY	Quantity: 1
Weight: 0.018 kg				
Institut für Physikalische Chemie Universität Stuttgart	Designed by: Martin Schneider		Accuracy: ISO 2758 mH	Sheet: 1
	Supervised by: Petr Neugebauer		Toleration: ISO 8015	
	Date: 10/01/2017		Projection: ISO E	

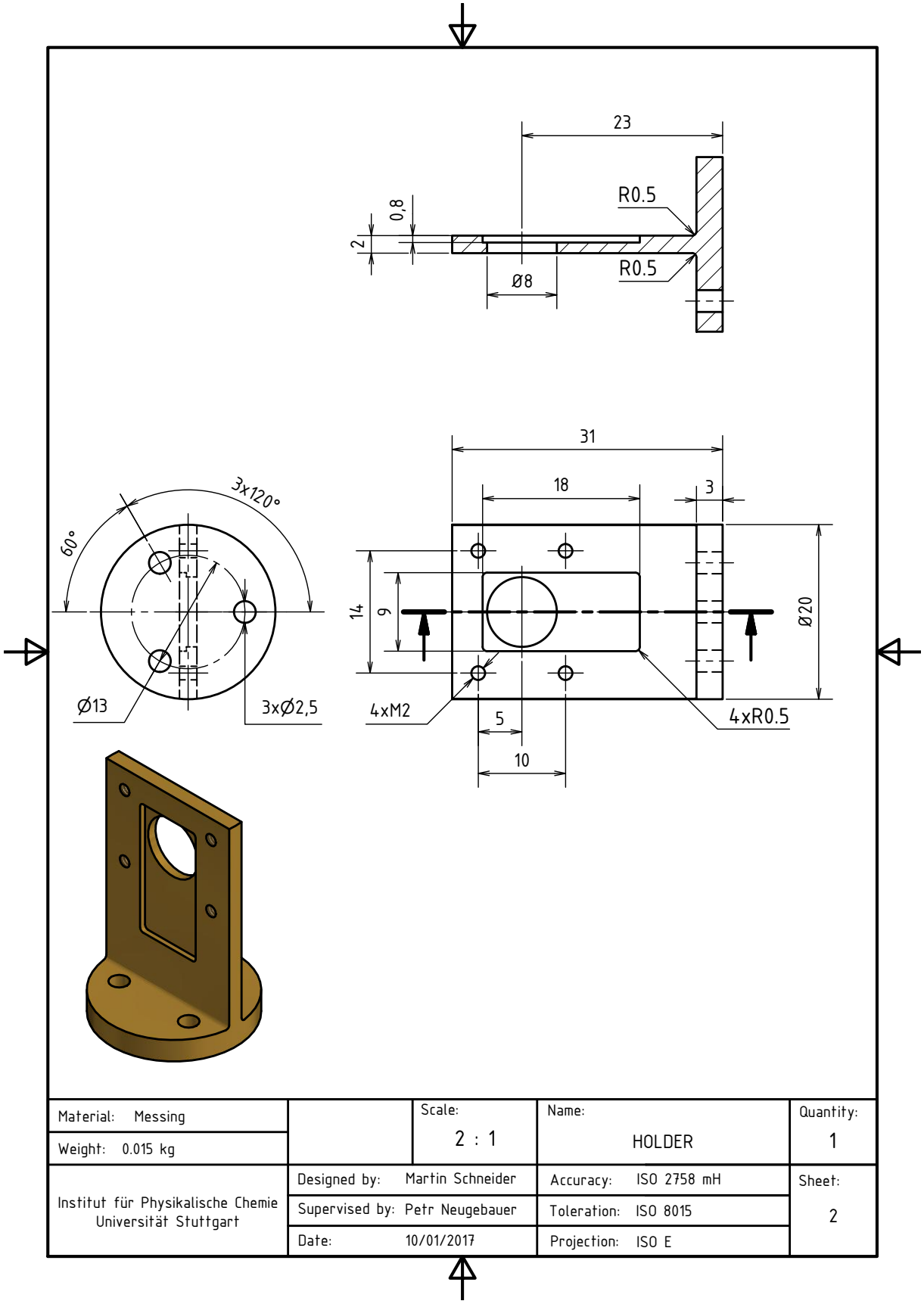

Material: Messing		Scale: 2 : 1	Name: HOLDER	Quantity: 1
Weight: 0.015 kg				
Institut für Physikalische Chemie Universität Stuttgart	Designed by: Martin Schneider		Accuracy: ISO 2758 mH	Sheet: 2
	Supervised by: Petr Neugebauer		Toleration: ISO 8015	
	Date: 10/01/2017		Projection: ISO E	

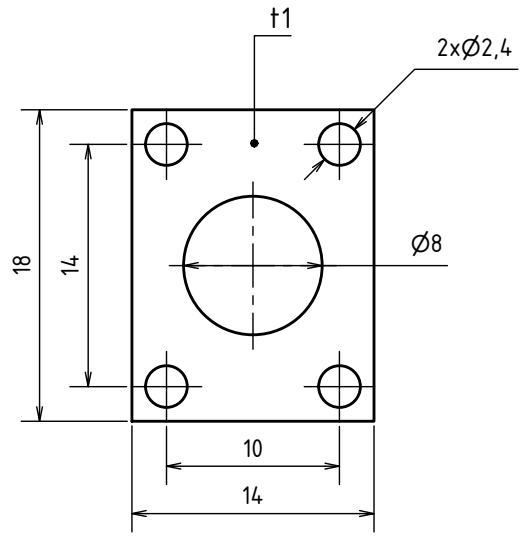

Material: Messing		Scale: 3 : 1	Name: SAMPLE MOUNTING	Quantity: 1
Weight: 0.002 kg				
Institut für Physikalische Chemie Universität Stuttgart	Designed by: Martin Schneider		Accuracy: ISO 2758 mH	Sheet: 3
	Supervised by: Petr Neugebauer		Toleration: ISO 8015	
	Date: 10/01/2017		Projection: ISO E	

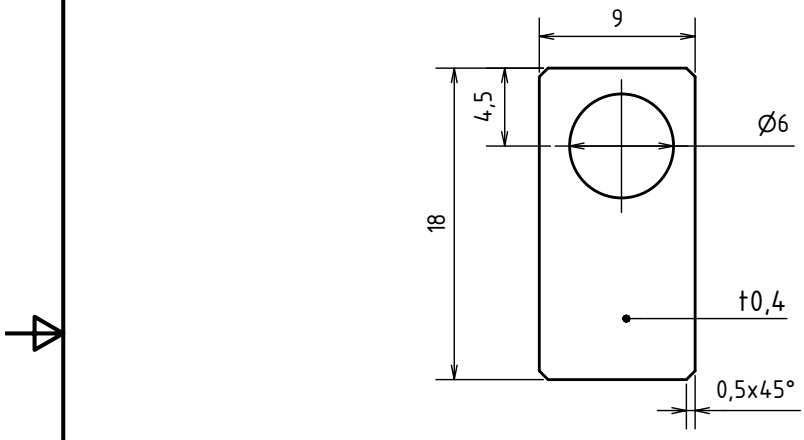

Material: Teflon		Scale: 3 : 1	Name: PTFE ISOLATOR	Quantity: 1
Weight: 0.000 kg				
Institut für Physikalische Chemie Universität Stuttgart	Designed by: Martin Schneider		Accuracy: ISO 2758 mH	Sheet: 4
	Supervised by: Petr Neugebauer		Toleration: ISO 8015	
	Date: 10/01/2017		Projection: ISO E	